SAND2017-10551R

Thermal-Hydraulic Results for the Boiling Water Reactor Dry Cask Simulator

Spent Fuel and Waste Disposition

Prepared for
US Department of Energy
Spent Fuel and Waste Science and Technology

S.G. Durbin and E.R. Lindgren
Sandia National Laboratories

September 29, 2017
SFWD-SFWST-2017-000033
SAND2017-####

Prepared by
Sandia National Laboratories
Albuquerque, New Mexico 87185 and Livermore, California 94550

Sandia National Laboratories is a multimission laboratory managed and operated by National Technology and Engineering Solutions of Sandia, LLC, a wholly owned subsidiary of Honeywell International, Inc., for the U.S. Department of Energy's National Nuclear Security Administration under contract DE-NA0003525.

EXECUTIVE SUMMARY

The thermal performance of commercial nuclear spent fuel dry storage casks is evaluated through detailed numerical analysis. These modeling efforts are completed by the vendor to demonstrate performance and regulatory compliance. The calculations are then independently verified by the Nuclear Regulatory Commission (NRC). Carefully measured data sets generated from testing of full sized casks or smaller cask analogs are widely recognized as vital for validating these models. Recent advances in dry storage cask designs have significantly increased the maximum thermal load allowed in a cask in part by increasing the efficiency of internal conduction pathways and by increasing the internal convection through greater canister helium pressure. These same canistered cask systems rely on ventilation between the canister and the overpack to convect heat away from the canister to the environment for both aboveground and belowground configurations. While several testing programs have been previously conducted, these earlier validation attempts did not capture the effects of elevated helium pressures or accurately portray the external convection of aboveground and belowground canistered dry cask systems.

The purpose of this investigation was to produce validation-quality data that can be used to test the validity of the modeling presently used to determine cladding temperatures in modern vertical dry casks. These cladding temperatures are critical to evaluate cladding integrity throughout the storage cycle. To produce these data sets under well-controlled boundary conditions, the dry cask simulator (DCS) was built to study the thermal-hydraulic response of fuel under a variety of heat loads, internal vessel pressures, and external configurations.

An existing electrically heated but otherwise prototypic BWR Incoloy-clad test assembly was deployed inside of a representative storage basket and cylindrical pressure vessel that represents a vertical canister system. The symmetric single assembly geometry with well-controlled boundary conditions simplified interpretation of results. Two different arrangements of ducting were used to mimic conditions for aboveground and belowground storage configurations for vertical, dry cask systems with canisters. Transverse and axial temperature profiles were measured throughout the test assembly. The induced air mass flow rate was measured for both the aboveground and belowground configurations. In addition, the impact of cross-wind conditions on the belowground configuration was quantified.

Over 40 unique data sets were collected and analyzed for these efforts. Fourteen data sets for the aboveground configuration were recorded for powers and internal pressures ranging from 0.5 to 5.0 kW and 0.3 to 800 kPa absolute, respectively. Similarly, fourteen data sets were logged for the belowground configuration starting at ambient conditions and concluding with thermal-hydraulic steady state. Over thirteen tests were conducted using a custom-built wind machine. The results documented in this report highlight a small, but representative, subset of the available data from this test series. This addition to the dry cask experimental database signifies a substantial addition of first-of-a-kind, high-fidelity transient and steady-state thermal-hydraulic data sets suitable for CFD model validation.

This page is intentionally left blank.

ACKNOWLEDGEMENTS

To identify all the individuals who participated in the success of this program would be impossible. The authors would like to acknowledge their hard work and commitment to excellence, albeit anonymously.

This work was conducted jointly between the Department of Energy Spent Fuel and Waste Science and Technology campaign and the Nuclear Regulatory Commission under contract NRC-HQ-60-15-T-0004. The authors gratefully acknowledge the technical guidance and support of Abdelghani Zigh and Jorge Solis at the NRC. This experimental effort benefitted immensely from pre-test computational fluid dynamics simulations to inform and guide the design of experiment.

The authors would also like to thank Greg Koenig and William Chavez of 8843 for their tireless efforts and dedication to service, which made the success of this project possible. Ken Sorenson, manager of 8843, is also to be commended for exceptional project leadership.

This page is intentionally left blank.

CONTENTS

Executive Summary iii

Acknowledgements v

Acronyms / Abbreviations xiii

1 Introduction 1
- 1.1 Objective 2
- 1.2 Previous Studies 2
  - 1.2.1 Small Scale, Single Assembly 2
  - 1.2.2 Full Scale, Multi Assembly 2
  - 1.2.3 Uniqueness of Dry Cask Simulator 4

2 Apparatus and Procedures 5
- 2.1 General Construction 5
- 2.2 Design of the Heated Fuel Bundle 7
- 2.3 Instrumentation 9
  - 2.3.1 Thermocouples (TCs) 9
  - 2.3.2 Pressure Vessel 18
  - 2.3.3 Power Control 19
  - 2.3.4 Hot Wire Anemometers 21
- 2.4 Air Mass Flow Rate 21
  - 2.4.1 Flow Straightening 22
  - 2.4.2 Aboveground Air Flow Measurement 22
  - 2.4.3 Belowground Air Flow Measurement 25
- 2.5 Cross-Wind Testing 27

3 Aboveground Results 31
- 3.1 Steady State Analyses 31
  - 3.1.1 Peak Cladding Temperature and Air Mass Flow Rate 31
  - 3.1.2 Two-Dimensional Temperature Contours 33
  - 3.1.3 Transverse Temperature Profiles including the TC Lance 35
  - 3.1.4 Summary Data Tables 36
- 3.2 Transient Analyses 38
  - 3.2.1 Transient Response of TC Lance and Corresponding Cladding 40

4 Belowground Results 43
- 4.1 Steady State Analyses 43
  - 4.1.1 Peak Cladding Temperature and Air Mass Flow Rate 43
  - 4.1.2 Two-Dimensional Velocity Contours 45
  - 4.1.3 Transverse Temperature Profiles Including the TC Lance 46
  - 4.1.4 Summary Data Tables 47
- 4.2 Transient Analyses 49
  - 4.2.1 Transient Response of TC Lance and Corresponding Cladding 51
- 4.3 Cross-Wind Analyses 52

5 Summary 57

6 References 59

Appendix A Error Propagation Analysis A-1
A.1 Temperature Measurements A-1
A.1.1 Uncertainty in Clad Temperature Measurement A-1
A.1.2 Uncertainty in Ambient Air Temperature A-2
A.2 Pressure Measurements A-2
A.2.1 Uncertainty in Ambient Air Pressure A-2
A.2.2 Uncertainty in Helium Vessel Pressure A-2
A.2.3 Uncertainty in Air Vessel Pressure A-2
A.3 Uncertainty in Electrical Measurements A-2
A.4 Flow Measurements A-2
A.4.1 Aboveground Configuration A-3
A.4.2 Belowground Configuration (Annular Gap) A-4
A.4.3 Cross-Wind Configuration A-6

Appendix B Thermocouple Lance Anomaly B-1
B.1 Background B-1
B.2 Anomalous Transient Behavior B-2
B.3 Responsible Phenomena Identification and Mitigation Plan B-15
B.4 Mitigation Results B-16

Appendix C Channel List from Aboveground Testing C-1

LIST OF FIGURES

Figure 1.1 Typical vertical aboveground storage cask system. 1
Figure 1.2 Typical vertical belowground storage cask system. 1
Figure 2.1 General design showing the plan view (upper left), the internal helium flow (lower left), and the external air flow for the aboveground (middle) and belowground configurations (right). 5
Figure 2.2 Carbon steel pressure vessel. 6
Figure 2.3 CYBL facility housing the aboveground version of the BWR cask simulator. 7
Figure 2.4 Typical 9×9 BWR components used to construct the test assembly including top tie plate (upper left), bottom tie plate (bottom left) and channel box and spacers assembled onto the water rods (right). 8
Figure 2.5 Typical TC attachment to heater rod. 9
Figure 2.6 Experimental BWR assembly showing as-built a) axial and b) lateral thermocouple locations. 10
Figure 2.7 Definition of coordinate references in test apparatus. 11
Figure 2.8 BWR channel box showing thermocouple locations. 12
Figure 2.9 Storage basket showing thermocouple locations. 13
Figure 2.10 Pressure vessel showing thermocouple locations. 14
Figure 2.11 Ducting for aboveground configuration showing thermocouple locations. 15
Figure 2.12 Ducting for belowground configuration showing thermocouple locations. 16
Figure 2.13 Location of thermocouples for gas temperature measurements at elevations of 1.219, 2.438, 3.658 m (48, 96, and 144 in.). 17
Figure 2.14 TC elevations for the TC lance. 18
Figure 2.15 Power control system and test circuits. 20
Figure 2.16 Schematic of the instrumentation panel for voltage, current and power measurements. 20
Figure 2.17 Photographs of the two types of hot wire anemometer tips. 21
Figure 2.18 Photograph of the honeycomb element used for flow straightening. 22
Figure 2.19 Aboveground configuration showing the location of the hot wire anemometer. 22
Figure 2.20 Mass flow rate as a function of hot wire output for forced flow. 23
Figure 2.21 Schematic showing the location of the inlet duct profiles for aboveground testing. 23
Figure 2.22 Diagram showing the integration scheme for the calculation of air mass flow rate for the aboveground configuration. 24
Figure 2.23 Natural-to-forced flow correlation. 25
Figure 2.24 Location of air flow measurement instrumentation for the belowground configuration. 25
Figure 2.25 Radial positioning of the hot wire anemometers for belowground testing. 26
Figure 2.26 Diagram showing the integration scheme for the calculation of air mass flow rate for the belowground configuration. 27

Figure 2.27 Layout of the cask simulator and wind machine for cross-wind testing. 27
Figure 2.28 Schematic showing the local coordinates of the wind machine. 28
Figure 2.29 Velocity contours of the wind machine for maximum cross-wind..... 28
Figure 2.30 Correlation of the two-dimensional, integrated average velocity ($W_{2D, avg}$) to the average of the three fixed hot wire anemometers ($W_{3\text{-}Pt, avg}$). 29
Figure 3.1 Steady state peak cladding temperature as a function of power. 31
Figure 3.2 Steady state air flow rate as a function of power. 32
Figure 3.3 Steady state peak cladding temperature as a function of absolute internal vessel pressure. 32
Figure 3.4 Steady state air mass flow rate as a function of absolute internal vessel pressure. 33
Figure 3.5 Steady state temperature contours for 5.0 kW at different internal helium pressures. 34
Figure 3.6 Steady state temperature contours for 0.5 kW at different internal vessel pressures. 34
Figure 3.7 Steady state transverse temperature profile at z = 3.023 m (119 in.) for the test conducted at 5.0 kW and 800 kPa helium. 35
Figure 3.8 Steady state transverse temperature profile at z = 3.023 m (119 in.) for the test conducted at 0.5 kW and 0.3 kPa air. 36
Figure 3.9 Peak cladding temperature as a function of time for tests conducted at 800 kPa helium.... 39
Figure 3.10 Total air mass flow rate as a function of time for tests conducted at 800 kPa helium. 39
Figure 3.11 Time to reach steady state as a function of power for the various vessel pressures tested.. 40
Figure 3.12 Comparison of TC lance and cladding temperatures at z = 3.023 m (119 in.) as a function of time for the test conducted at 5.0 kW and 800 kPa helium. 41
Figure 3.13 Comparison of TC lance and cladding temperatures at z = 3.023 m (119 in.) as a function of time for the test conducted at 0.5 kW and 0.3 kPa air. 41
Figure 4.1 Steady state peak cladding temperature as a function of power. 43
Figure 4.2 Steady state air mass flow rate in the inlet annulus as a function of power. 44
Figure 4.3 Steady state peak cladding temperature as a function of absolute internal vessel pressure. 44
Figure 4.4 Steady state air mass flow rate in the inlet annulus as a function of absolute internal vessel pressure. 45
Figure 4.5 Steady state velocity contours for 5.0 kW at different internal helium pressures. 45
Figure 4.6 Steady state velocity contours for 0.5 kW at different internal vessel pressures. 45
Figure 4.7 Steady state transverse temperature profile at z = 3.023 m (119 in.) for the test conducted at 5.0 kW and 800 kPa helium. 46
Figure 4.8 Steady state transverse temperature profile at z = 3.023 m (119 in.) for the test conducted at 0.5 kW and 0.3 kPa air. 47
Figure 4.9 Peak cladding temperature as a function of time for tests conducted at 800 kPa helium.... 50
Figure 4.10 Total air mass flow rate as a function of time for tests conducted at 800 kPa helium. 50
Figure 4.11 Time to reach steady state as a function of power for the various vessel pressures tested.. 51

Figure 4.12 Comparison of TC lance and cladding temperatures at z = 3.023 m (119 in.) as a function of time for the test conducted at 5.0 kW and 800 kPa helium. 52

Figure 4.13 Comparison of TC lance and cladding temperatures at z = 3.023 m (119 in.) as a function of time for the test conducted at 0.5 kW and 0.3 kPa air. 52

Figure 4.14 Normalized air mass flow rates as a function of cross-wind speed for 1.0 kW tests. 53

Figure 4.15 Normalized air mass flow rates as a function of cross-wind speed for 2.5 kW tests. 54

Figure 4.16 Normalized air mass flow rates as a function of cross-wind speed for 5.0 kW tests. 54

Figure 4.17 Normalized air mass flow rates as a function of cross-wind speed for 100 kPa tests. 55

Figure 4.18 Normalized air mass flow rates as a function of cross-wind speed for 800 kPa tests. 55

Figure 4.19 Orientation of the wind machine and test assembly. 56

Figure 4.20 Velocity contours for 5.0 kW and 100 kPa at different cross-wind speeds. 56

LIST OF TABLES

Table 2.1 Dimensions of assembly components in the 9×9 BWR. 8
Table 2.2 List of proposed equipment for power control. 21
Table 3.1 Steady state results for the primary assembly measurements at 0.3 kPa air. 36
Table 3.2 Steady state results for the primary assembly measurements at 100 kPa helium. 37
Table 3.3 Steady state results for the primary assembly measurements at 450 kPa helium. 37
Table 3.4 Steady state results for the primary assembly measurements at 800 kPa helium. 38
Table 4.1 Steady state results for the primary assembly measurements at 0.3 kPa air. 47
Table 4.2 Steady state results for the primary assembly measurements at 100 kPa helium. 48
Table 4.3 Steady state results for the primary assembly measurements at 450 kPa helium. 48
Table 4.4 Steady state results for the primary assembly measurements at 800 kPa helium. 49
Table 4.5 Rise in peak cladding temperature attributed to cross-wind conditions. 53

ACRONYMS / ABBREVIATIONS

ANSI	American National Standards Institute
BWR	boiling water reactor
DAQ	data acquisition
DCS	Dry Cask Simulator
DOE	Department of Energy
EPRI	Electric Power Research Institute
FCRD	Fuel Cycle Research and Development
MSB	multi-assembly sealed basket
NRC	Nuclear Regulatory Commission
PCT	peak cladding temperature
PID	proportional-integral-differential controller
PWR	pressurized water reactor
SCR	silicon controlled rectifier
SNF	spent nuclear fuel
SNL	Sandia National Laboratories
TC	thermocouple
VCC	ventilated concrete cask

This page is intentionally left blank.

1 INTRODUCTION

The performance of commercial nuclear spent fuel dry storage casks is evaluated through detailed analytical modeling of the system's thermal performance. These modeling efforts are performed by the vendor to demonstrate the performance and regulatory compliance and are independently verified by the Nuclear Regulatory Commission (NRC). Most commercial dry casks in use today store the fuel in an aboveground configuration, although belowground storage has grown in recent years. Both horizontally and vertically oriented aboveground dry cask systems are currently in use. Figure 1.1 shows a diagram for a typical vertical aboveground system. Cooling of the assemblies located inside the sealed canister is enhanced by the induced flow of air drawn in the bottom of the cask and exiting out the top of the cask.

Source: www.nrc.gov/reading-rm/doc-collections/fact-sheets/storage-spent-fuel-fs.html

Figure 1.1 Typical vertical aboveground storage cask system.

Figure 1.2 shows a diagram for a typical, vertical belowground system. For belowground configurations air is drawn in from the top periphery and channeled to the bottom where it then flows upward along the wall of the canister and exits out the top center of the cask.

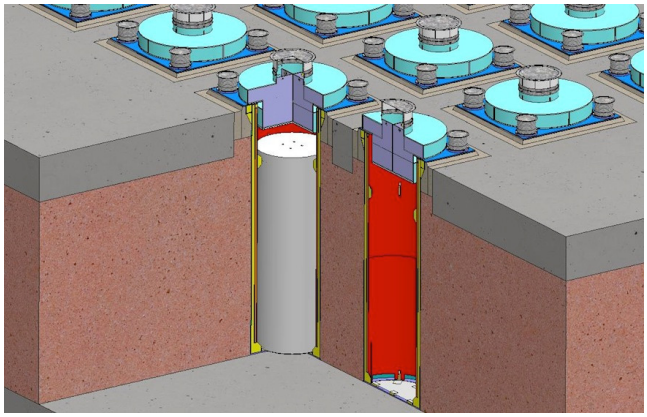

Source: www.holtecinternational.com/productsandservices/wasteandfuelmanagement/hi-storm/

Figure 1.2 Typical vertical belowground storage cask system.

Carefully measured data sets generated from testing of full sized casks or smaller cask analogs are widely recognized as vital for validating design and performance models. Numerous studies have been previously conducted [Bates, 1986; Dziadosz and Moore, 1986; Irino *et al.*, 1987; McKinnon *et al.*,1986]. Recent advances in dry storage cask designs have significantly increased the maximum thermal load allowed in a cask in part by increasing the efficiency of internal conduction pathways and by increasing the internal convection through greater canister helium pressure. These vertical, canistered cask systems

rely on ventilation between the canister and the overpack to convect heat away from the canister to the environment for both above and belowground configurations. While several testing programs have been previously conducted, these earlier validation attempts did not capture the effects of elevated helium pressures or accurately portray the external convection of aboveground and belowground canistered dry cask systems. Previous cask performance validation testing did not capture these parameters. Thus, the enhanced performance of modern dry storage casks cannot be fully validated using previous studies.

1.1 Objective

The purpose of this investigation was to produce a data set that can be used to test the validity of the modeling presently used to determine cladding temperatures in modern vertical dry casks, which are used to evaluate cladding integrity throughout the storage cycle. To produce these data sets under well-controlled boundary conditions, the dry cask simulator (DCS) was built to study the thermal-hydraulic response of fuel under a variety of heat loads, internal vessel pressures, and external configurations. The results documented in this report highlight a small, but representative, subset of the available data from this test series. To illustrate the breadth of the data sets collected for each test, an example channel list for the data acquisition system (DAQ) can be found in Appendix C.

In addition, the results generated in this test series supplement thermal data collected as part of the High Burnup Dry Storage Cask Project [EPRI, 2014]. A shortened version of the thermal lance design deployed in the Cask Project was installed in the DCS. The installation of this lance in the DCS assembly allowed the measurement of temperatures inside of a "guide tube" structure and direct comparisons with fuel cladding.

1.2 Previous Studies

1.2.1 Small Scale, Single Assembly

Two single assembly investigations were documented in the mid-1980s [Bates, 1986; Irino *et al.*, 1987]. Both included electrically heated 15×15 pressurized water reactor (PWR) assemblies with thermocouples installed to directly measure the surface temperature of the cladding. In Bates (1986) the electrically heated assembly was instrumented with 57 TCs distributed over 7 axial levels. In Irino *et al.* (1987) the electrically heated assembly was instrumented with 92 TCs distributed over 4 axial levels. In Bates (1986) a single irradiated 15×15 PWR assembly was also studied using 105 thermocouples distributed equally into each of the fifteen guide tubes at seven axial levels. All were limited to one atmosphere helium or air, and all imposed a constant temperature boundary condition on the outer cask wall in an attempt to achieve prototypic storage temperatures in the fuel assembly bundle.

1.2.2 Full Scale, Multi Assembly

A number of full scale multi-assembly cask studies were also documented in the mid-1980s to early 1990s, one for a BWR cask with unconsolidated fuel assemblies [McKinnon *et al*., 1986] and the others for PWR casks with both consolidated and unconsolidated fuel [Dziadosz *et al*., 1986; McKinnon *et al*., 1987; Creer *et al*., 1987; McKinnon *et al*.,1989; McKinnon *et al*., 1992]. Only in the most recent study was a ventilated cask design tested. In all studies the cask were studied with internal atmospheres ranging from vacuum up to 150 kPa (21.8 psia) using air, nitrogen, or helium.

In the first study [McKinnon *et al*., 1986], 28 or 52 BWR assemblies with a total heat load of 9 or 15 kW respectively were contained in REA 2023 prototype steel-lead-steel cask with a water-glycol neutron shield. Thirty-eight TCs were installed on the cask interior. Twenty-four of those were installed in direct contact with the center rod in 7 assemblies at up to 7 different elevations. Twelve were installed on the basket at 3 different elevations. Two TCs were installed in direct contact with a fuel rod located on the center outer face of an assembly. The cask was tested in a vertical and horizontal orientation with atmospheres of vacuum or nitrogen at 145 kPa (21 psia) average or helium at 152 kPa (22 psia) average.

In the earliest full scale PWR cask study [Dziadosz *et al*., 1986], twenty-one PWR assemblies with a total heat load of 28 kW were contained in a Castor-V/21 cast iron/graphite cask with polyethylene rod neutron shielding. The interior of the cask was instrumented with sixty thermocouples deployed on ten lances located in eight guide tubes and two basket void spaces. Two of the assembly lances were installed into the center assembly. Note with the use of TC lances inside of the assembly guide tubes no direct fuel cladding temperatures were measured. The cask was tested in a vertical and horizontal orientation with atmospheres of vacuum or nitrogen at 57 kPa (8.3 psia) or helium at 52 kPa (7.5 psia).

A relatively low total heat load of 12.6 kW was tested in a Westinghouse MC-10 cask with 24 PWR assemblies [McKinnon *et al*., 1987]. The MC-10 has a forged steel body and distinctive vertical carbon steel heat transfer fins around the outer circumference. The outer surface of the cask was instrumented with 34 thermocouples. The interior of the cask was instrumented with 54 thermocouples deployed on 9 TC lances in 7 fuel assembly guide tubes and 2 basket void spaces. The cask was tested in a vertical and horizontal orientation and interior atmosphere was either a vacuum or 150 kPa (21.8 psia) helium or air.

A pair of studies using the same TN-24 cask was tested with 24 PWR assemblies with 20.5 kW total output [Creer *et al*., 1987] or 24 consolidated fuel canisters with 23 kW total output [McKinnon *et al*.,1989]. The TN-24P has a forged steel body surrounded by a resin layer for neutron shielding. The resin layer is covered by a smooth steel outer shell. The TN-24P is a prototype version of the standard TN-24 cask with differences in the cask body thickness, basket material and neutron shield structure. The TN-24P also incorporates 14 thermocouples into the basket structure. In both studies the fuel was instrumented with 9 TC lances with 6 TCs per lance, 7 in fuel guide tubes and 2 in simulated guide tubes in basket void spaces. The outside surface was instrumented with 35 TCs in the unconsolidated fuel study [Creer *et al*., 1987] and 27 TCs in the consolidated fuel study [McKinnon *et al*.,1989]. In both studies the cask was tested in a vertical and horizontal orientation with the interior atmosphere as either a vacuum or 150 kPa (21.8 psia) helium or air. A seventh test was conducted in the consolidated fuel study [McKinnon *et al*.,1989] for a horizontal orientation under vacuum with insulated ends to simulate impact limiters.

None of the previous studies discussed so far included or accounted for internal ventilation of the cask. Both of the single assembly investigations imposed constant temperature boundary conditions [Bates, 1986; Irino *et al.*, 1987] and 4 full scale cask studies discussed so far [Dziadosz *et al*., 1986; McKinnon *et al*., 1987; Creer *et al*., 1987; McKinnon *et al*.,1989] considered externally cooled cask designs.

In only one previous study was a ventilated cask design considered, and this cask was the VSC-17 [McKinnon *et al*., 1992]. The VSC-17 cask system consists of a ventilated concrete cask (VCC) and a removable multi-assembly sealed basket (MSB). The VCC is steel lined and incorporates four inlet vents to the outside neat the bottom and four outlet vents near the top. When the MSB is placed inside the VCC an annular gap is formed and the vents allow air to be drawn in from the bottom through the annular gap and out the top vents. The lid on the MSB is a specially designed bolted closure that seals the basket interior and closes off the top of the cask above the top vents. The VSC-17 is a specially designed test version (holding 17 PWR assemblies) of the commercial VSC-24 cask (holding 24 PWR assemblies). The VSC-17 is smaller and lighter and incorporates the bolted lid to facilitate testing. The VSC-24 is larger and utilizes a welded lid canister for containing the spent fuel assemblies.

In the investigation of the VSC-17 cask, 17 consolidated PWR fuel canisters with a total heat load of 14.9 kW were utilized. The cask system was instrumented with 98 thermocouples. Forty-two of these were deployed on 7 TC lances with 6 TCs each. Six lances were installed in the fuel canisters and one was installed in a basket void space. Nine TCs were located on the outer MSB wall and 9 TCs were located on the inner VCC liner. Ten TCs were embedded in the VCC concrete wall. One TC was located at each vent inlet and outlet. Thirteen TCs were located on the outer cask surface and weather cover. Testing consisted of six runs all in a vertical orientation. In 4 tests the MSB was filled with helium at an average pressure of 95 kPa (13.8 psia). The vents were either all unblocked, or the inlets were half blocked, or the

inlets were fully blocked or both the inlets and outlets were fully blocked. The other two runs were with unblocked vents and 84 kPa (12.2 psia) nitrogen or vacuum.

1.2.3 Uniqueness of Dry Cask Simulator

This investigation differed from previous studies in several significant ways. Principle among these was that the canister pressure vessel was tested with helium pressures up to 800 kPa and assembly powers up to 5.0 kW until a steady state temperature profile was established. During the apparatus heating, the helium pressure was controlled to be constant to within ±0.3 kPa (0.044 psi). Additionally, ventilated design boundary conditions for aboveground and belowground configurations were explicitly simulated. The experimental approach of the present study is different than the previous studies. Rather than striving to achieve prototypic peak clad temperatures by artificially imposing a temperature boundary condition on the canister wall, this study represented the physics of near-prototypic boundary conditions.

2 APPARATUS AND PROCEDURES

This chapter describes the various subsystems, construction, and methods used for this testing. The test apparatus design was guided by an attempt to match critical dimensionless groups with prototypic systems as reasonably as possible; namely Reynolds, Rayleigh, and Nusselt numbers. The dimensional analyses revealed that a scaling distortion in simulated assembly power would be necessary to more closely match the thermal-hydraulic response of a full sized spent fuel storage cask. This need for additional decay heat is reasonable given the higher external surface-area-to-volume ratio of a single assembly arrangement as in the DCS compared to a modern canister with up to 89 assemblies, but a more rigorous treatment was recorded and is available for further details [Durbin, *et al.*, 2016].

Each phase of experimental apparatus design and implementation was also guided by extensive, meticulous computational fluid dynamics (CFD) modeling that is not explicitly detailed in this report. A brief description and example of modeling results may be found in Zigh, *et al.*, 2017. As an example, these models provided information on the flow profile development and thermal gradients that were critical to the optimization of flow straightening and hot wire anemometer placements.

2.1 General Construction

The general design details are shown in Figure 2.1. An existing electrically heated but otherwise prototypic BWR Incoloy-clad test assembly was deployed inside of a representative storage basket and cylindrical pressure vessel that represents the canister. The symmetric single assembly geometry with well-controlled boundary conditions simplified interpretation of results. Various configurations of outer concentric ducting were used to mimic conditions for aboveground and belowground storage configurations of vertical, dry cask systems with canisters. Radial and axial temperature profiles were measured for a wide range of decay power and canister pressures. Of particular interest was the evaluation of the effect of increased helium pressure on heat load for both the aboveground and belowground configurations. The effect of wind speed was also measured for the belowground configuration. External, air mass flow rates were calculated from measurements of the induced air velocities in the external ducting.

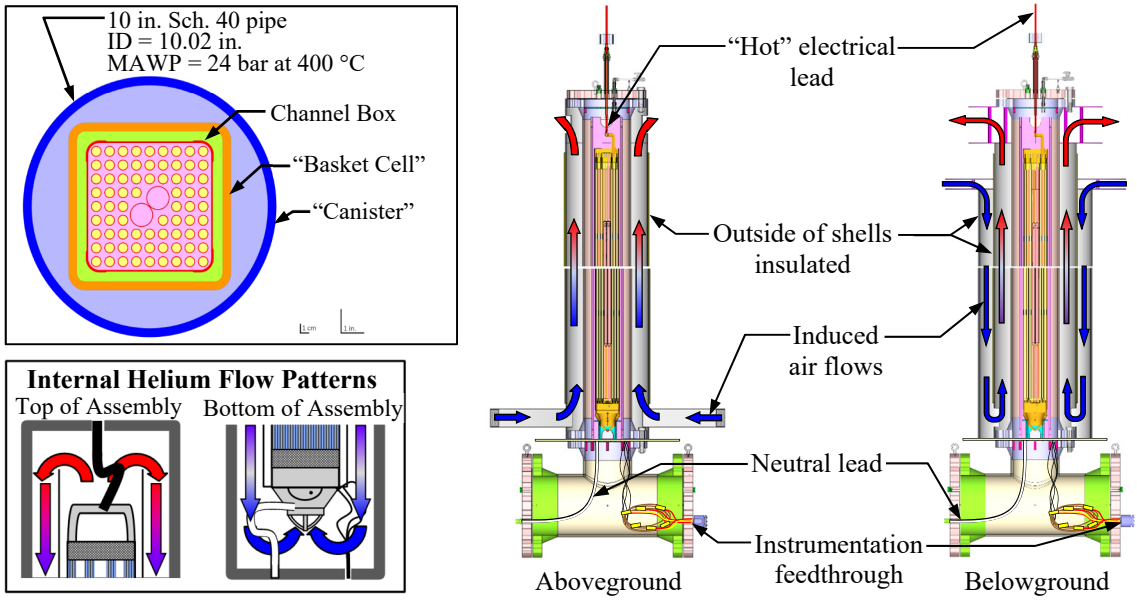

Figure 2.1 General design showing the plan view (upper left), the internal helium flow (lower left), and the external air flow for the aboveground (middle) and belowground configurations (right).

Figure 2.2 shows the major carbon steel components used to fabricate the pressure vessel. The 4.572 m (180 in.) long vertical test section was made from 0.254 m (10 in.) Schedule 40 pipe welded to Class 300 flanges. The 0.356 × 0.254 m (14 × 10 in.) Schedule 40 reducing tee was needed to facilitate the routing of over 150 thermocouples (TCs) through the pressure vessel. Blind flanges with threaded access ports for TC and power lead pass-throughs were bolted to the top of the vertical test stand section and the sides of the reducing tee. The maximum allowable working pressure was 2,400 kPa at 400 °C. Bar stock tabs were welded inside the 0.254 m (10 in.) flange on the tee to support the test assembly and on the top of the test section to allow an insulated top boundary condition.

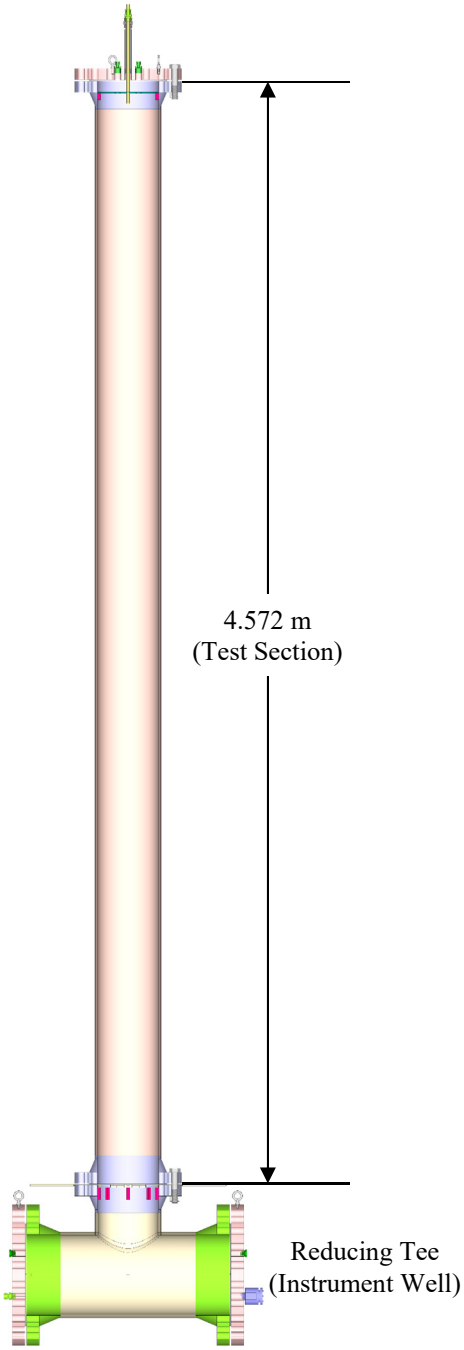

Figure 2.2 Carbon steel pressure vessel.

The test configurations were assembled and operated inside of the Cylindrical Boiling (CYBL) test facility, which is the same facility used for earlier fuel assembly studies [Lindgren and Durbin, 2007]. CYBL is a large stainless steel containment vessel repurposed from earlier flooded containment/core retention studies sponsored by DOE. Since then CYBL has served as an excellent general-use engineered barrier for the isolation of high-energy tests. The outer vessel is 5.1 m in diameter and 8.4 m tall (16.7 ft. in diameter and 27.6 feet tall) and constructed with 9.5 mm (0.375 in.) thick stainless steel walls. Figure 2.3 shows a scaled diagram of CYBL facility with the aboveground version of the test BCS inside.

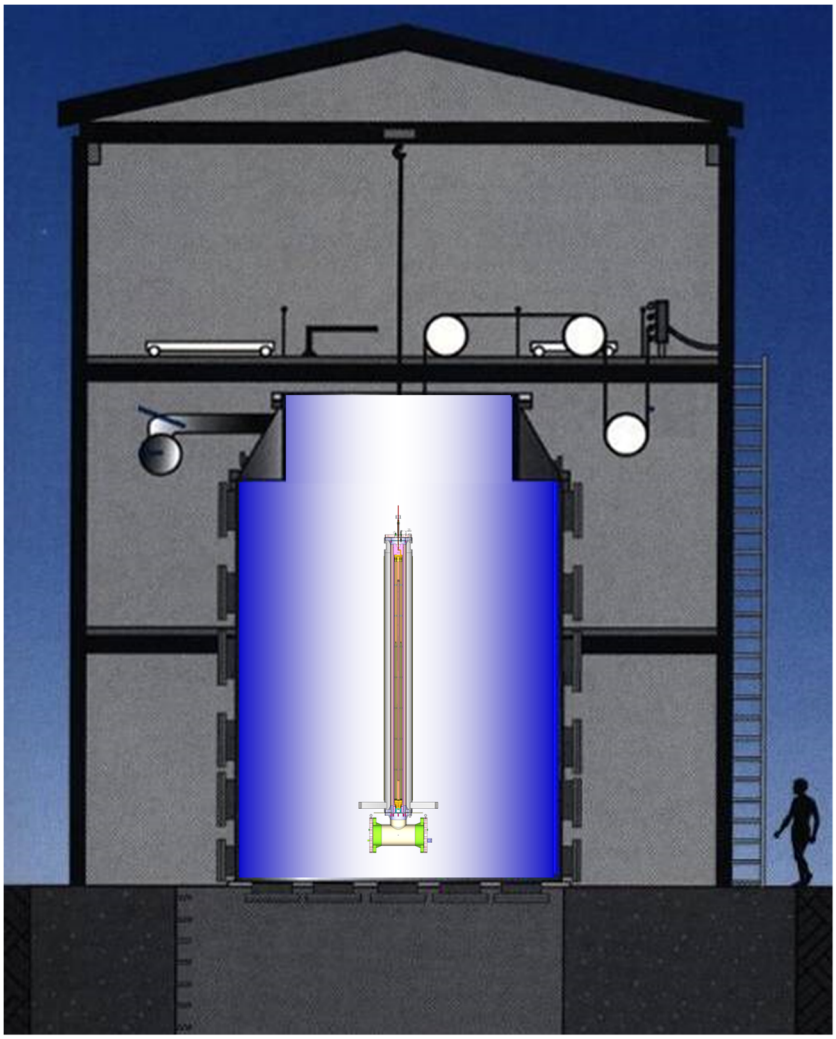

Figure 2.3 CYBL facility housing the aboveground version of the BWR cask simulator.

2.2 Design of the Heated Fuel Bundle

The highly prototypic fuel assembly was modeled after a 9×9 BWR. Commercial components were purchased to create the assembly including the top and bottom tie plates, spacers, water rods, channel box, and all related assembly hardware (see Figure 2.4). Incoloy heater rods were substituted for the fuel rod pins for heated testing. Due to fabrication constraints the diameter of the Incoloy heaters was slightly smaller than prototypic pins, 10.9 mm versus 11.2 mm. The slightly simplified Incoloy mock fuel pins were fabricated based on drawings and physical examples from the nuclear component supplier. The dimensions of the assembly components are listed below in Table 2.1.

Table 2.1 Dimensions of assembly components in the 9×9 BWR.

Description	Lower (Full) Section	Upper (Partial) Section
Number of pins	74	66
Pin diameter (mm)	10.9	10.9
Pin pitch (mm)	14.4	14.4
Pin separation (mm)	3.48	3.48
Water rod OD (main section) (mm)	24.9	24.9
Water rod ID (mm)	23.4	23.4
Nominal channel box ID (mm)	134	134
Nominal channel box OD (mm)	139	139

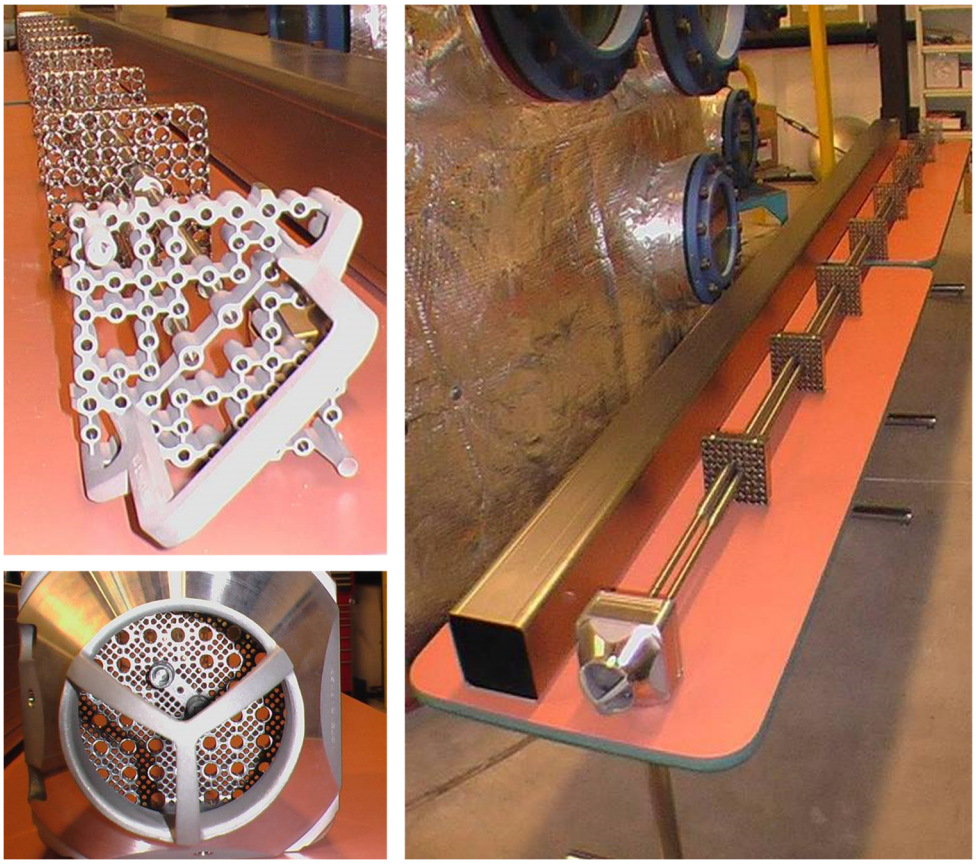

Figure 2.4 Typical 9×9 BWR components used to construct the test assembly including top tie plate (upper left), bottom tie plate (bottom left) and channel box and spacers assembled onto the water rods (right).

The thermocouples used are ungrounded junction Type K with an Incoloy sheath diameter of 0.762 mm (0.030 in.) held in intimate contact with the cladding by a thin Nichrome shim. This shim is spot welded to the cladding as shown in Figure 2.5. The TC attachment method allows the direct measurement of the cladding temperature.

Figure 2.5 Typical TC attachment to heater rod.

2.3 Instrumentation

The test apparatus was instrumented with thermocouples (TCs) for temperature measurements, pressure transducers to monitor the internal vessel pressure, and hot wire anemometers for flow velocity measurement in the exterior ducting. Volumetric flow controllers were used to calibrate the hot wire probes. Voltage, amperage, and electrical power transducers were used for monitoring the electrical energy input to the test assembly.

Ninety-seven thermocouples were previously installed on the BWR test assembly. Details of the BWR test assembly and TC locations are described elsewhere [Lindgren and Durbin, 2007]. Additional thermocouples were installed on the other major components of the test apparatus such as the channel box, storage basket, canister wall, and exterior air ducting. TC placement on these components is designed to correspond with the existing TC placement in the BWR assembly.

Hot wire anemometers were chosen to measure the inlet flow rate because this type of instrument is sensitive and robust while introducing almost no unrecoverable flow losses. Due to the nature of the hot wire measurements, best results are achieved when the probe is placed in an isothermal, unheated gas flow.

2.3.1 Thermocouples (TCs)

2.3.1.1 BWR Assembly TC locations

The existing electrically heated prototypic BWR Incoloy-clad test assembly was previously instrumented with thermocouples in a layout shown in Figure 2.6. The assembly TCs are arranged in axial and radial arrays. The axial cross-section is depicted in Figure 2.6a and radial cross-sections are shown in Figure 2.6b. The axial array A1 has TCs nominally spaced every 0.152 m (6 in.) starting from the top of the bottom tie plate (z_o = 0 reference plane). Axial array A2 has TCs nominally spaced every 0.305 m (12 in.) and the radial arrays are nominally spaced every 0.610 m (24 in.). The spacings are referred to as nominal due to a deviation at the 3.023 m (119 in.) elevation because of interference by a spacer. Note that the TCs in the axial array intersect with the radial arrays.

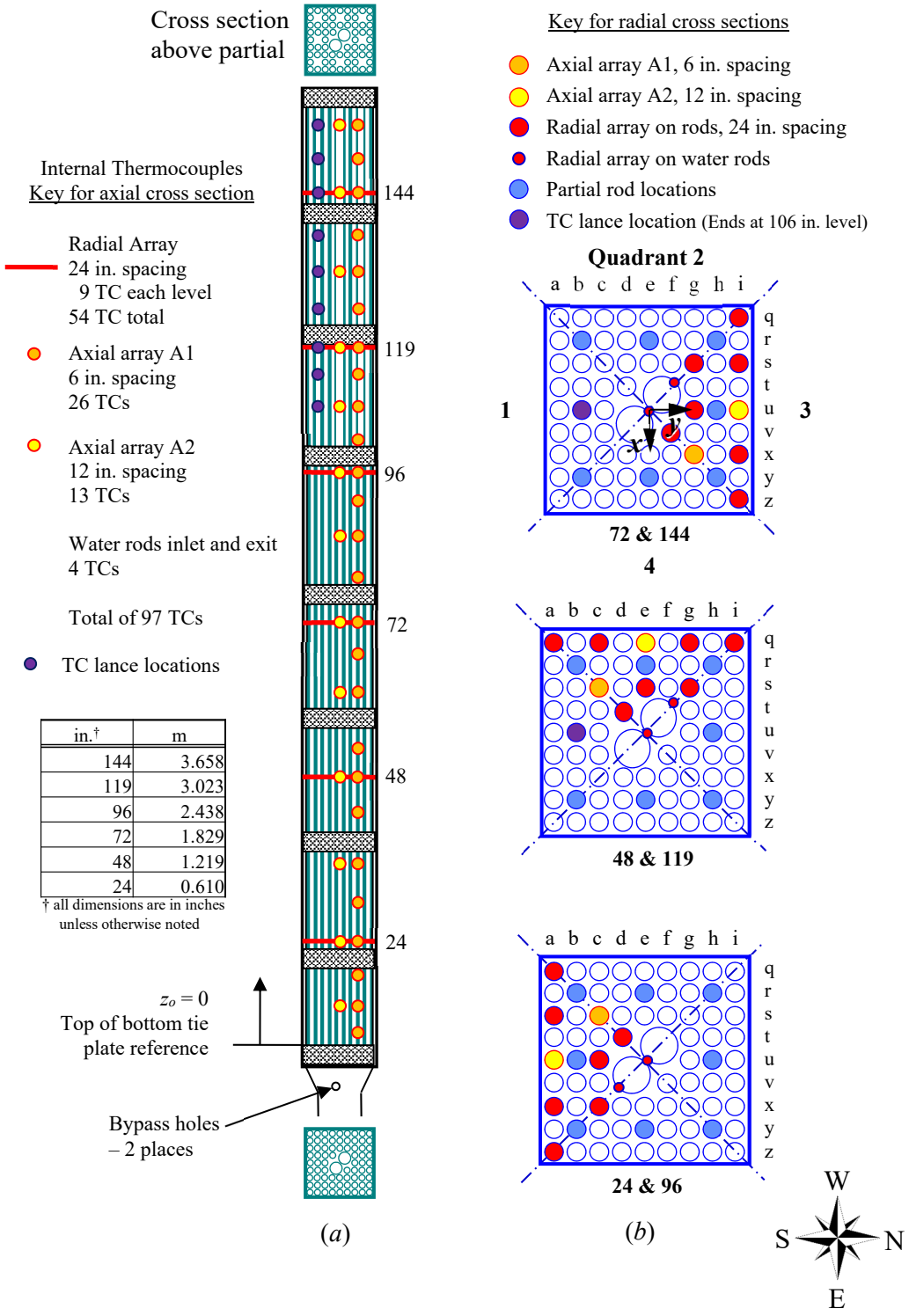

Figure 2.6 Experimental BWR assembly showing as-built *a*) axial and *b*) lateral thermocouple locations.

Based on the need to optimally balance the TC routing through the assembly the axial and radial array TCs were distributed among three separate quadrants relying on the assumption of axial symmetry.

Also shown in Figure 2.6 is the location of the TC lance (for more details see Section 2.3.1.8). The quadrant for the lance deployment was chosen to minimize the possibility of damaging any of the previously installed TCs. The TC spacing on the lance matched the elevation of the TCs in the upper portion of the A1 and A2 axial arrays and the radial array at 3.023 m (119 in.) and 3.658 m (144 in.) elevations.

Figure 2.7 shows the definition of the reference coordinate system. The reference origin is defined as being in the center of the top of the bottom tie plate. The *x*-axis is positive in the direction of Quadrant 4 and negative in the direction of Quadrant 2. The *y*-axis is positive in the direction of Quadrant 3 and negative in the direction of Quadrant 1.

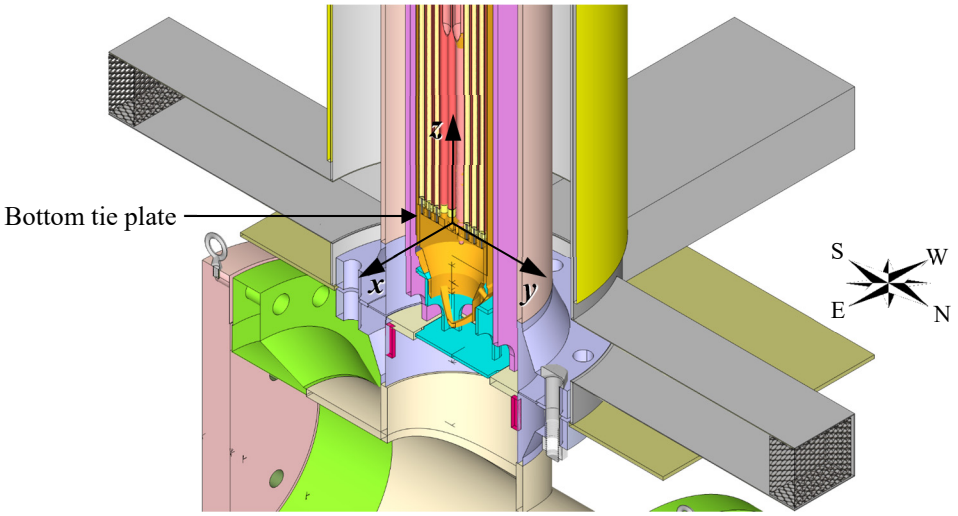

Figure 2.7 Definition of coordinate references in test apparatus.

2.3.1.2 BWR Channel Box TC Locations

The BWR channel box was instrumented with 25 TCs as depicted in Figure 2.8. Twenty-one of the TCs were on the channel faces, three were on the corners and one was on the pedestal. The TCs on the faces of the channel box were nominally located at |x|, |y| = 0.069, 0 m (2.704, 0 in.) or |x|, |y| = 0, 0.069 m (0, 2.704 in.) depending on the quadrant in which they were placed. TCs on the corners were located at |x|, |y| = 0.065, 0.065 m (2.564, 2.564 in.). The reference plane, z_o, was measured from the top of the bottom tie plate, the same as the BWR assembly. Multiple TCs on different faces at a given elevation were available to check the axial symmetry assumption at 0.610 m (24 in.) intervals starting at the z = 0.610 m (24 in.) elevation.

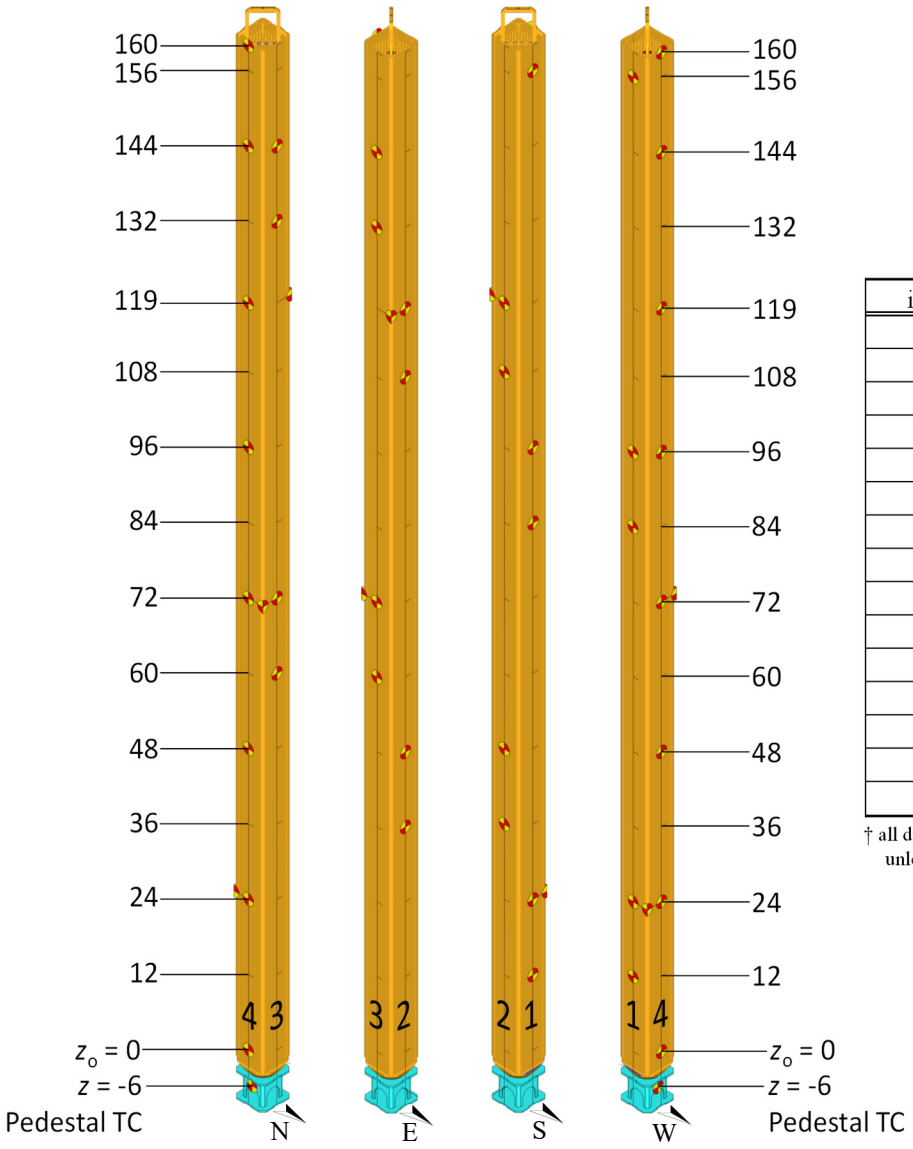

in.†	m
160	4.064
156	3.962
144	3.658
132	3.353
119	3.023
108	2.743
96	2.438
84	2.134
72	1.829
60	1.524
48	1.219
36	0.914
24	0.610
12	0.305
-6	-0.152

† all dimensions are in inches unless otherwise noted

Figure 2.8 BWR channel box showing thermocouple locations.

2.3.1.3 Storage Basket TC Locations

The storage basket was instrumented with 26 TCs as depicted in Figure 2.9. Twenty-two of the TCs were on the basket faces at the same positions as on the channel box, four were on the corners (the corner TC at the 4.191 m (165 in.) level did not correspond to a channel box TC) and one was on the basket face at the elevation of the pedestal. TCs located on the basket faces were located at |x|, |y| = 0, 0.089 m (0, 3.5 in.) and |x|, |y| = 0.089, 0 m (3.5, 0 in.). TCs on the corners were located at |x|, |y| = 0.083, 0.083 m (3.281, 3.281 in.). The reference plane, z_o, was measured from the top of the bottom tie plate.

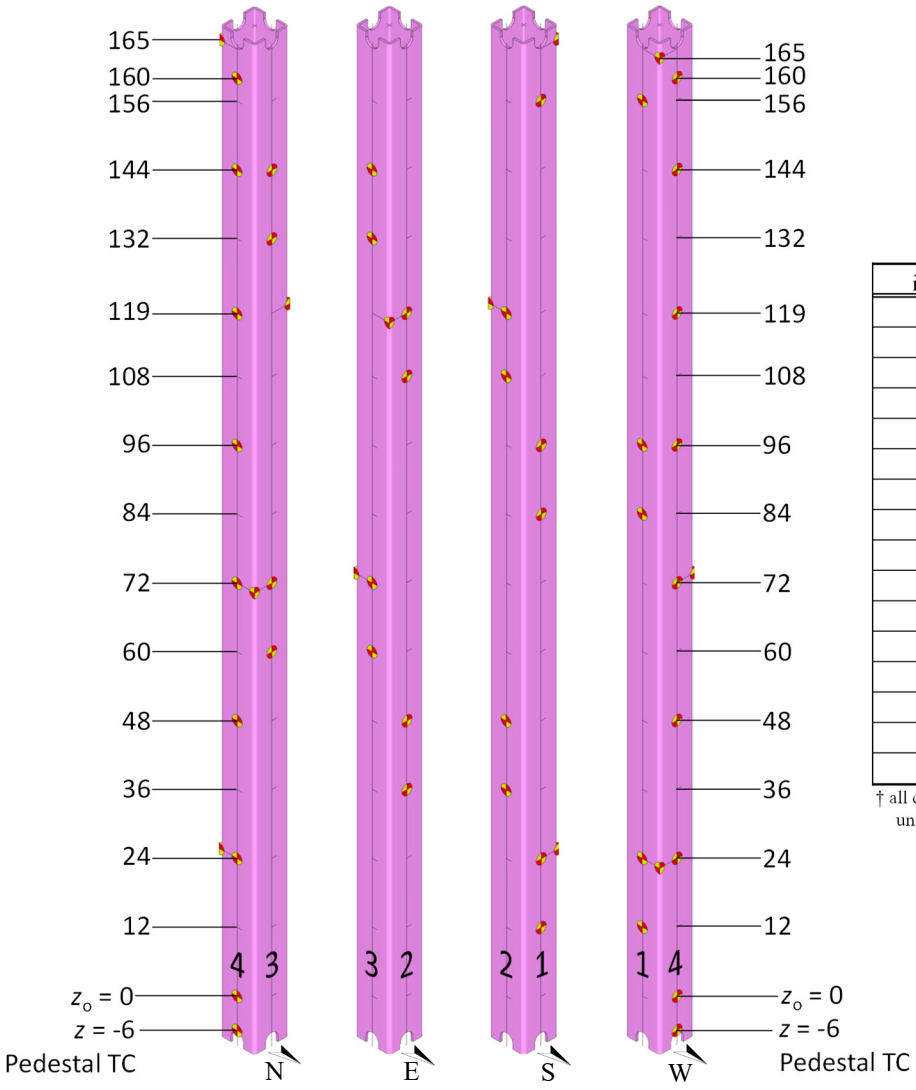

in.†	m
165	4.191
160	4.064
156	3.962
144	3.658
132	3.353
119	3.023
108	2.743
96	2.438
84	2.134
72	1.829
60	1.524
48	1.219
36	0.914
24	0.610
12	0.305
-6	-0.152

† all dimensions are in inches unless otherwise noted

Figure 2.9 Storage basket showing thermocouple locations.

2.3.1.4 Pressure Vessel TC Locations

The pressure vessel was instrumented with 27 TCs as depicted in Figure 2.10. Twenty-four of the TCs were aligned with the TCs on the storage basket faces and three were aligned with the TCs on the storage basket corners. TCs aligned with the storage basket faces were located at |x|, |y| = 0, 0.137 m (0, 5.375 in.) and |x|, |y| = 0.137, 0 m (5.375, 0 in.). TCs aligned with the storage basket corners were located at |x|, |y| = 0.097, 0.097 m (3.801, 3.801 in.). The reference plane, z_o, was measured from the top of the bottom tie plate.

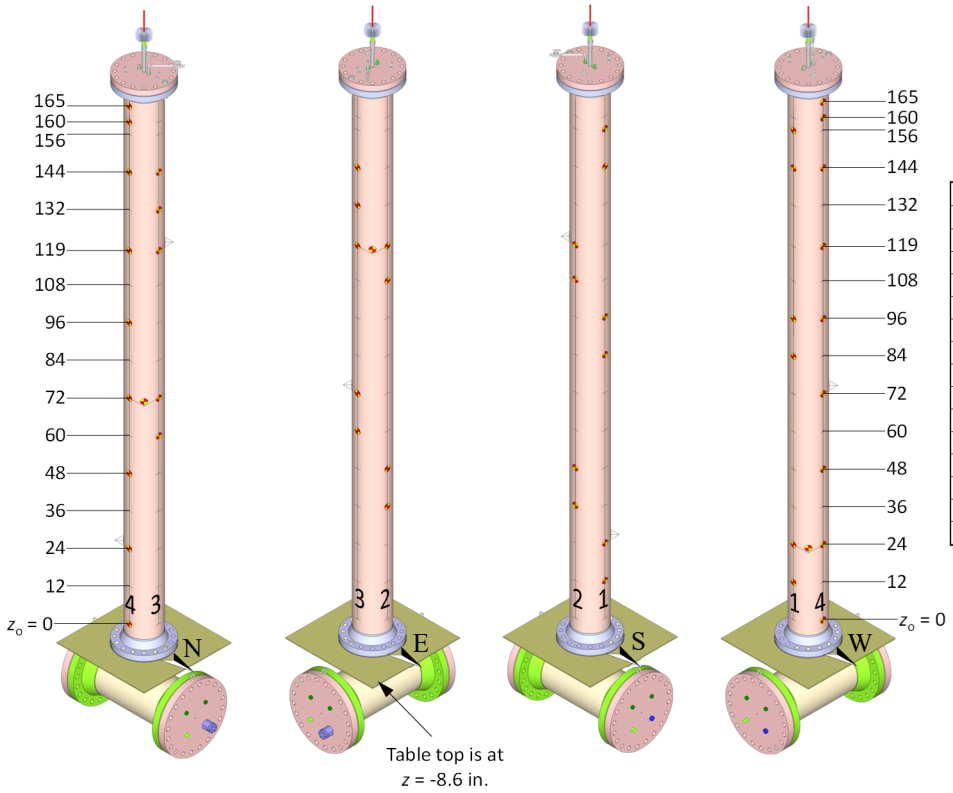

in.†	m
165	4.191
160	4.064
156	3.962
144	3.658
132	3.353
119	3.023
108	2.743
96	2.438
84	2.134
72	1.829
60	1.524
48	1.219
36	0.914
24	0.610
12	0.305

† all dimensions are in inches unless otherwise noted

Figure 2.10 Pressure vessel showing thermocouple locations.

2.3.1.5 Aboveground Configuration Ducting TC Locations

The concentric air flow duct for the aboveground configuration was instrumented with 27 thermocouples depicted in Figure 2.11. Twenty-four of the TCs were aligned with the TCs on the channel box and storage basket faces; three were aligned with the corners. The face aligned TCs were located at |x|, |y| = 0, 0.233 m (0, 9.164 in.) and |x|, |y| = 0.233, 0 m (9.164, 0 in.). The corner aligned TCs were located at |x|, |y| = 0.165, 0.165 m (6.480, 6.480 in.). The reference plane, z_o, was measured from the top of the bottom tie plate.

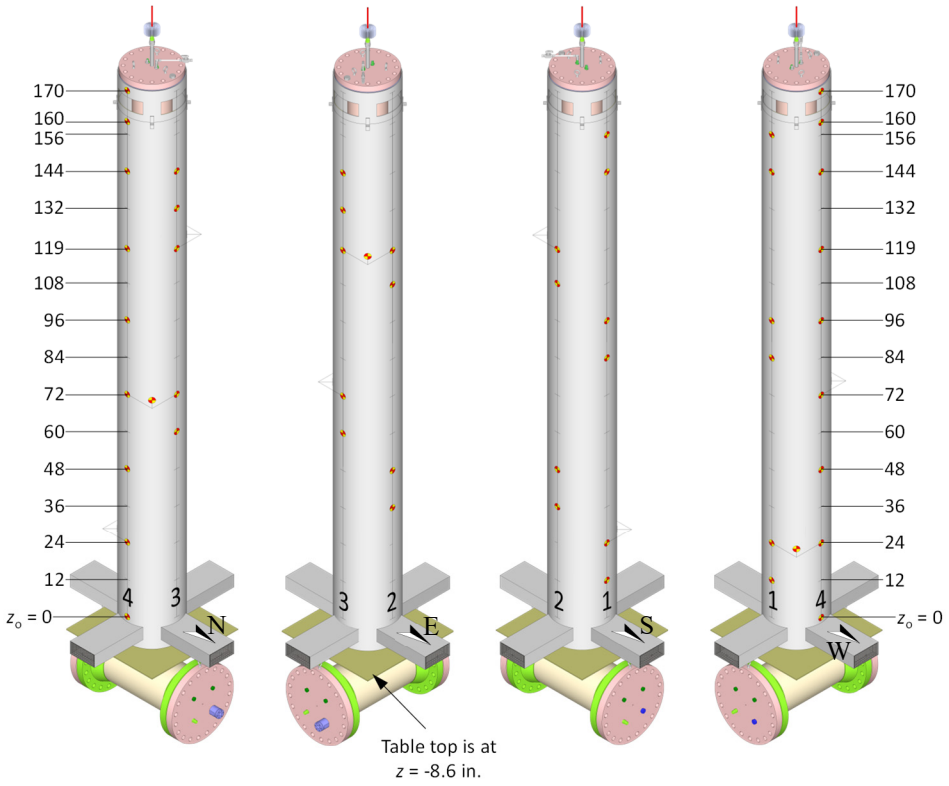

in †	m
170	4.318
165	4.191
160	4.064
156	3.962
144	3.658
132	3.353
119	3.023
108	2.743
96	2.438
84	2.134
72	1.829
60	1.524
48	1.219
36	0.914
24	0.610
12	0.305

† all dimensions are in inches unless otherwise noted

Figure 2.11 Ducting for aboveground configuration showing thermocouple locations.

2.3.1.6 Belowground Configuration Ducting TC Locations

The concentric air flow duct for the belowground configuration was instrumented with 24 thermocouples depicted in Figure 2.12. Twenty-one of the TCs were aligned with the TCs on the channel box and storage basket faces; three were aligned with the corners. The face aligned TCs were nominally located at |x|, |y| = 0, 0.316 m (0, 12.427 in.) and |x|, |y| = 0.316, 0 m (12.427, 0 in.). The corner aligned TCs were nominally located at |x|, |y| = 0.223, 0.223 m (8.787, 8.787 in.). The reference plane, z_o, was measured from the top of the bottom tie plate.

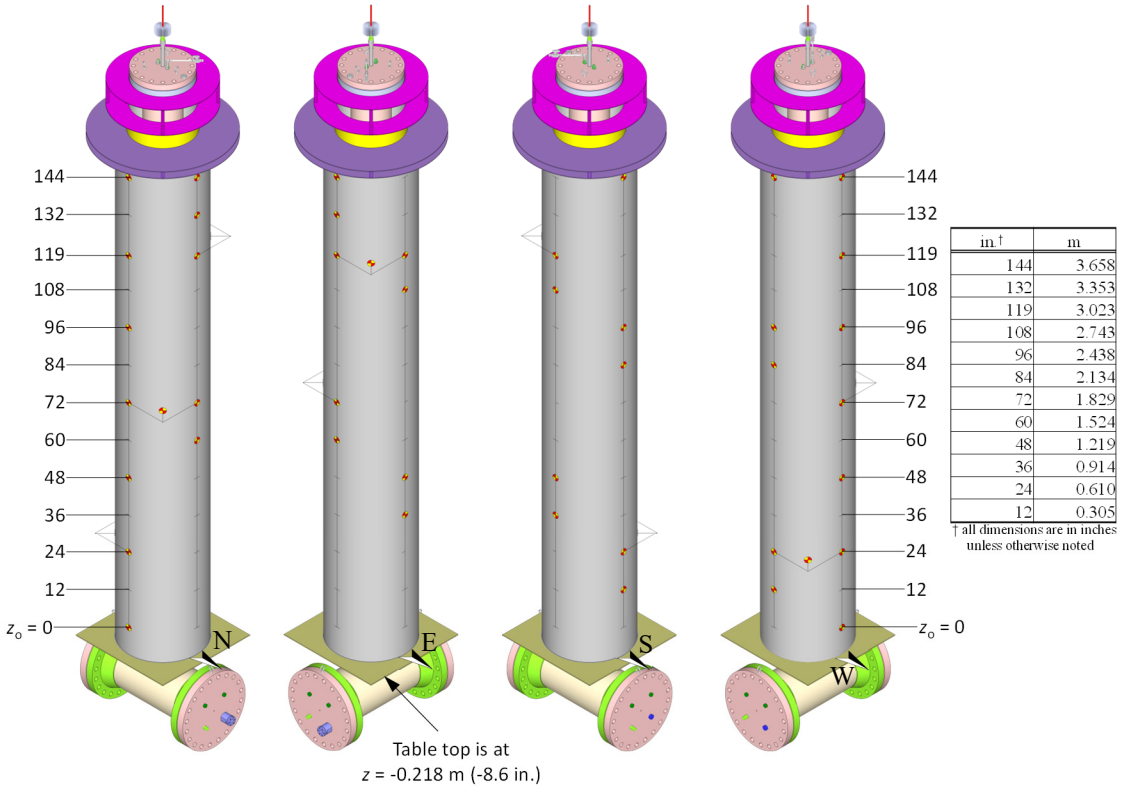

in †	m
144	3.658
132	3.353
119	3.023
108	2.743
96	2.438
84	2.134
72	1.829
60	1.524
48	1.219
36	0.914
24	0.610
12	0.305

† all dimensions are in inches unless otherwise noted

Figure 2.12 Ducting for belowground configuration showing thermocouple locations.

2.3.1.7 Gas Temperature TC Locations

Up to 37 TCs were used to measure the temperature of the gas flowing in the various regions of the test apparatus at three different elevations as depicted in Figure 2.13. For the aboveground configuration testing, the outer most gas TCs were installed but the outer shell (shell 2) was not in place. The center region shown in red denotes helium flowing upward while it was heated inside the assembly and storage basket. Moving outward, the region shown in orange depicts helium flowing downward as it cooled along the inner pressure vessel wall. A total of 17 TCs were used for gas temperature measurements inside the pressure vessel. More TCs were used at the upper two elevations where higher temperature and temperature gradients were measured.

Moving further outward the region shown in green is air moving upward as it heated along the outer pressure vessel wall. The outer most region, shown in blue, is cool air flowing downward in the belowground configuration. For the aboveground configuration, the outer blue region was open to ambient. The narrow yellow region on the outside of each of the concentric air ducts represents a 6 mm (0.25 in.) thick layer of high temperature insulation.

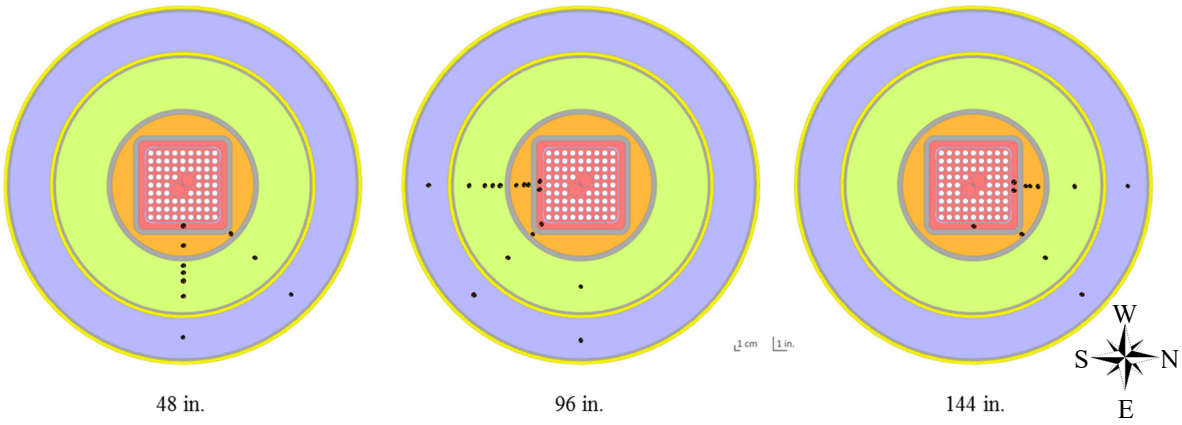

Figure 2.13 Location of thermocouples for gas temperature measurements at elevations of 1.219, 2.438, 3.658 m (48, 96, and 144 in.).

2.3.1.8 Thermocouple Lance

A custom TC lance was deployed in the upper portion of the test assembly above a partial length rod as illustrated previously in Figure 2.6. Design details of the lance are shown in Figure 2.14. The design provided for a pressure boundary along the outer surface of the lance with a pressure seal at a penetration in the top flange using standard tube fittings. The lance was made by the same fabricator using the same process and materials as the TC lances that were used in the full scale High Burnup Dry Storage Cask Research and Development Project [EPRI, 2014]. The TC spacing was designed to correspond with TCs installed on the test assembly heater rod cladding to provide a direct comparison between the two measurements. Direct comparisons between TC lance and corresponding clad temperature measurements will aid in the interpretation of the TC lance data generated during the High Burnup Cask Project.

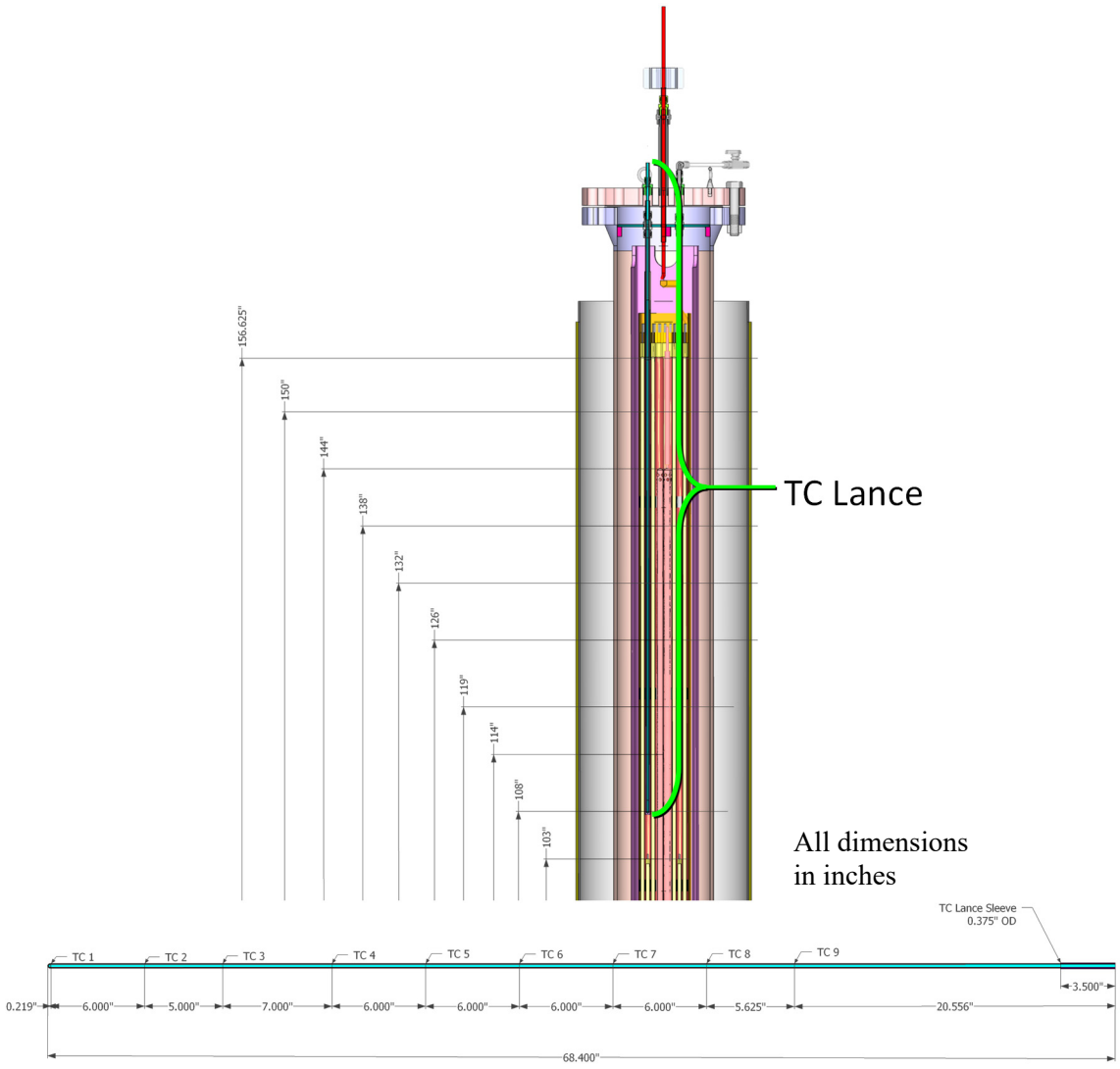

Figure 2.14 TC elevations for the TC lance.

2.3.2 Pressure Vessel

Two high accuracy 0 to 3447 kPa (0 to 500 psia) absolute pressure transducers (OMEGA PX409-500A5V-XL) were installed in the lower reducing tee for redundancy. The experimental uncertainty associated with these gauges is ±0.03% of full scale, or ±1.0 kPa (0.15 psi). At least one of these transducers was operational for each heated test. For testing below atmospheric pressure, a dedicated vacuum transducer 0 to 100 kPa (0 to 14.5 psia) absolute (OMEGA PXM409-001BV10V) was used in place of the higher range absolute pressure transducers.

All penetrations and fittings were selected for the apparatus to have helium leak rates of 1E-6 std. cm^3/s or better at 100 kPa. In addition, spiral wound gaskets capable of leak rates of better than 1E-7 std. cm^3/s were used to form the seals at each flange. The ANSI N14.5 leak rate of 1E-4 std. cm^3/s [ANSI, 2014] would result in an observable pressure drop of 0.03 kPa (4E-3 psi) after a one week period, which is far below the experimental uncertainty of 1.0 kPa (0.15 psi). Leaks in the as-built apparatus were identified and repaired as best as possible. Ultimately, a small leak path of undetermined origin remained, and a positive pressure control system was implemented to maintain pressure as described next. Under

subatmospheric (0.3 kPa) conditions, the system leak path resulted in air infiltrating the pressure vessel. Therefore, the residual gas composition for 0.3 kPa testing was air, not helium.

2.3.2.1 Pressure Control

A helium pressure control system was implemented using the high accuracy absolute pressure transducers, three low flow needle valves, and three positive shutoff actuator valves under control of the LabView DAC system. Two actuator valves (vent) controlled helium flow out of the vessel, and the third valve (fill) controlled helium flow into the vessel. As the vessel heated up, the expanding helium was vented out the first actuator and needle valve to maintain a constant pressure. A second vent valve (overflow) activated if the vessel continued to pressurize. As steady state was reached, the small helium leak slowly reduced the helium pressure at which point the control system opened the third actuator valve (fill) to allow a small helium flow through the third needle valve. Overall, the pressure control system maintained the helium pressure constant to ±0.3 kPa (0.044 psi).

For the subatmospheric tests, the pressure control system was not utilized. A vacuum pump was used to evacuate the vessel, and the ultimate vacuum achieved was a balance between the vacuum pump and the small air leak into the vessel.

2.3.2.1 Pressure Vessel Internal Volume Measurement

The pressure vessel was pressurized with air in a manner that allowed the measurement of the as-built total internal volume. The pressure vessel was first pressurized to 100 kPa (14.5 psia). The pressure vessel was then slowly pressurized to 200 kPa (29.0 psia) with a high accuracy 0 to 5 liters per minute flow controller (OMEGA FMA 2606A-TOT-HIGH ACCURACY). A high accuracy 0 to 3447 kPa (500 psia) absolute pressure transducer (OMEGA PX409-500A5V-XL) was used to monitor the transient fill progression. The transient mass flow and pressure data were used to determine the total internal volume to be 252.0 liters with an uncertainty of ±2.6 liters.

2.3.3 Power Control

A diagram of the test assembly power control system is shown in Figure 2.15 and the details inside the instrument panel are shown in Figure 2.16. The electrical voltage and current delivered to the test assembly heaters was controlled to maintain a constant power by a silicon controlled rectifier (SCR). The data acquisition (DAQ) system provided a power setpoint to a PID controller that sent a control signal to the SCR based on the power measurement. The power, voltage, and current measurements were collected by the DAQ. The details of the instrumentation used to control and measure the electrical power are provided in Table 2.2.

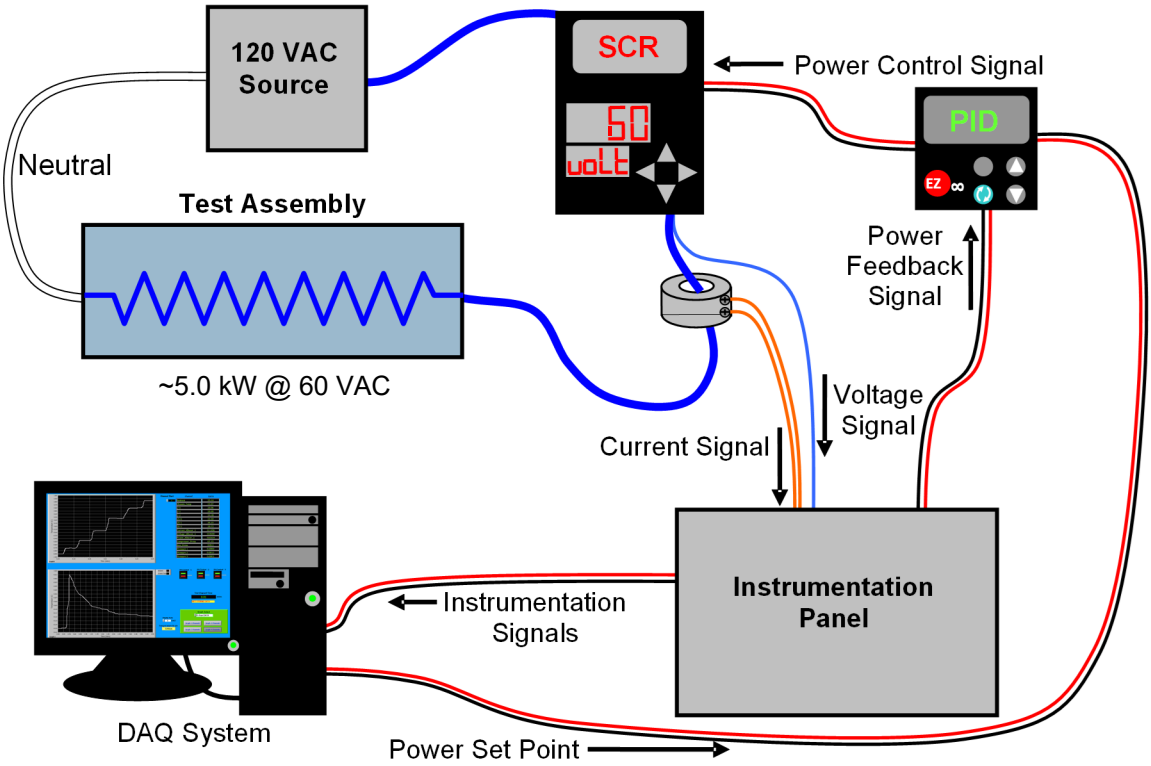

Figure 2.15 Power control system and test circuits.

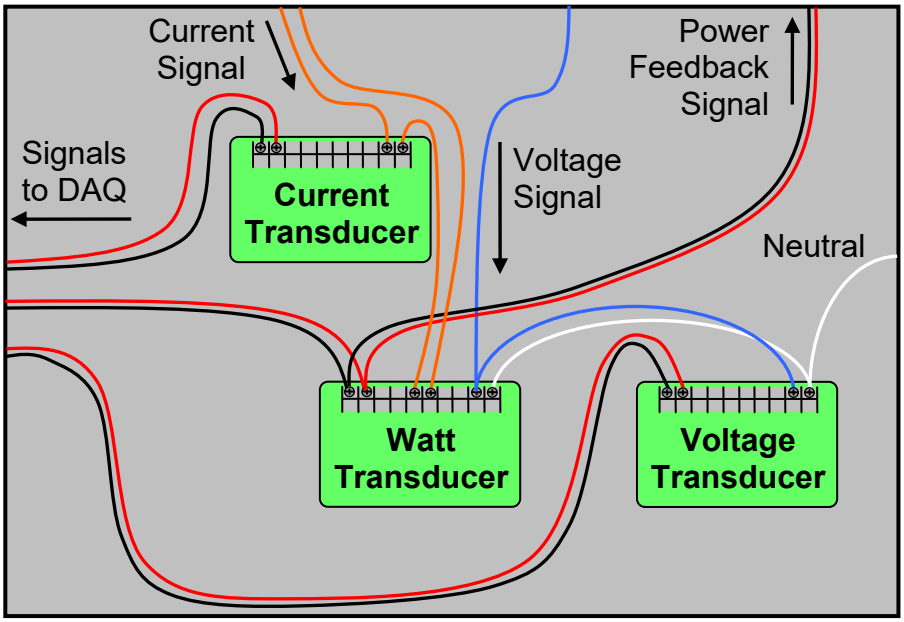

Figure 2.16 Schematic of the instrumentation panel for voltage, current and power measurements.

Table 2.2 List of proposed equipment for power control.

Description	Manufacturer	Model
AC Watt Transducer	Ohio Semitronics	PC5-001DY230
AC Voltage Transducer	Ohio Semitronics	AVTR-001D
AC Current Transducer	Ohio Semitronics	ACTR-005DY06
PID Controller	Watlow Electric Manufacturing	PM6C1FJ1RAAAAA
SCR Power Controller	Watlow Electric Manufacturing	PC91-F25A-1000

2.3.4 Hot Wire Anemometers

The hot wire anemometers used for this testing were TSI models 8475 and 8455. The sensor tip details are shown in Figure 2.17. For scale, the largest shaft diameter shown was 6.4 mm (0.25 in.). The sensing element of the model 8455 is protected inside of an open cage and is sensitive to flows down to 0.13 m/s (25 ft/min) with a fast response time of 0.2 seconds. The sensing element of the model 8475 is the ball at the tip, which results in sensitivity to flows down to 0.05 m/s (10 ft/min) but with a much larger response time of 5 seconds.

Hot wire anemometers were chosen to measure the inlet flow rate because this type of instrument is sensitive and robust while introducing almost no unrecoverable pressure loss. Due to the nature of the hot wire measurement, for best results the probes were placed in the gas flow at the flow inlets where temperature and thermal gradients were minimal.

Figure 2.17 Photographs of the two types of hot wire anemometer tips.

2.4 Air Mass Flow Rate

The methods for determining the induced air flow in the aboveground and belowground configurations were similar but have some distinct differences. Both methods used hot wire anemometers to measure inlet air velocity and subsequently calculate an overall air mass flow rate.

For the aboveground configuration, the hot wires were fixed in the center of the inlet ducts and subjected to known mass flow rates of air using mass flow controllers during a series of pre-test measurements. The output of the hot wires was then correlated to the forced mass flow rate input. Additionally, a velocity profile was measured along the short dimension of the center of the inlet during steady state operation of each heated, buoyancy-driven (natural) test. A mass flow rate was calculated from these velocity profiles and provided a correction correlation between the natural-to-forced flow data.

For the belowground configuration, forced flow calibration in the annulus between Shell 1 and Shell 2 was not possible. The mass flow was determined by integrating the velocity profiles of multiple hot wire anemometers positioned around the annulus. For belowground testing, eight hotwires were mounted on motorized stages (Velmex Stage XN10-0040-M02-71, Motor PK245-01AA) at equidistant positions. The data acquisition computer communicated with the stage controller (Velmex Controller VXM-4) to identify and verify hot wire positioning. An additional four hot wires were added to one half of the Shell

1 and Shell 2 annulus for belowground, cross-wind testing to more accurately measure the effect of larger velocity gradients.

2.4.1 Flow Straightening

To obtain the most stable and repeatable measurements possible, a honeycomb element was inserted into the inlets of both the aboveground and belowground configurations. This honeycomb served to align the flow in the desired direction and reduce any flow disturbances on the hot wire measurements. As shown in Figure 2.18, a plastic honeycomb element was chosen with a cell diameter, wall thickness, and flow length of 3.8, 0.1, and 51.6 mm (0.150, 0.004, and 2.030 in.), respectively. This type of flow straightening element was found to provide the greatest reduction in hot wire fluctuations while introducing the smallest pressure drop to the system. The effective, frictional coefficient for this honeycomb material was found to be D = 2.7E6 m^{-2} for porous media in CFD simulations.

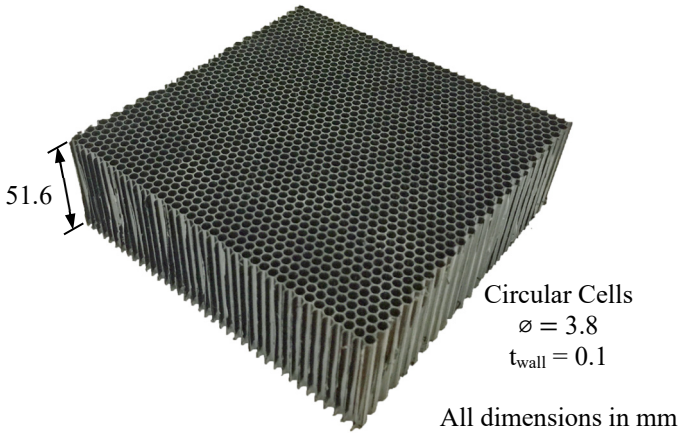

Figure 2.18 Photograph of the honeycomb element used for flow straightening.

2.4.2 Aboveground Air Flow Measurement

The inlet and hot wire arrangement for the aboveground configuration is shown in Figure 2.19. Four rectangular ducts with as-built cross sectional dimensions of 0.229 m (9.03 in.) by 0.100 m (3.94 in.) conveyed the inlet flow into the simulated cask. One TSI Model 8475 and three TSI Model 8455 hot wire anemometers were used for these tests. Hot wire anemometers were located 0.229 m (9.00 in.) downstream from the inlet of each duct along the centerline of flow.

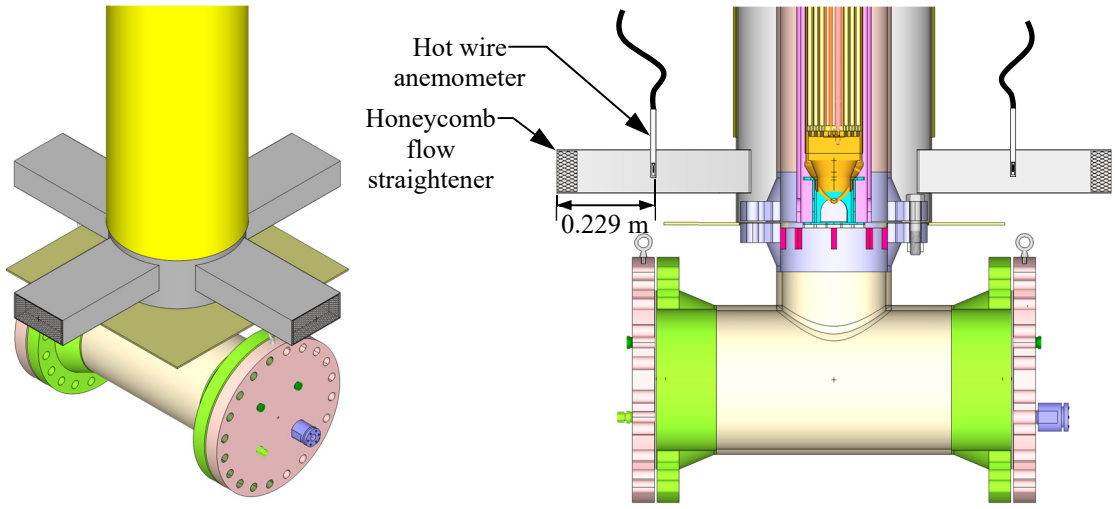

Figure 2.19 Aboveground configuration showing the location of the hot wire anemometer.

2.4.2.1 Forced Flow Correlation

The outputs of the hot wire anemometers were correlated using metered, forced flow. Air flow was metered into each of the inlet ducts individually, and the response of each anemometer in the center of the inlet recorded for a range of flow rates as shown in Figure 2.20. A least-squares regression was used to define the linear coefficients to convert the hot wire anemometer output to mass flow rate during heated testing.

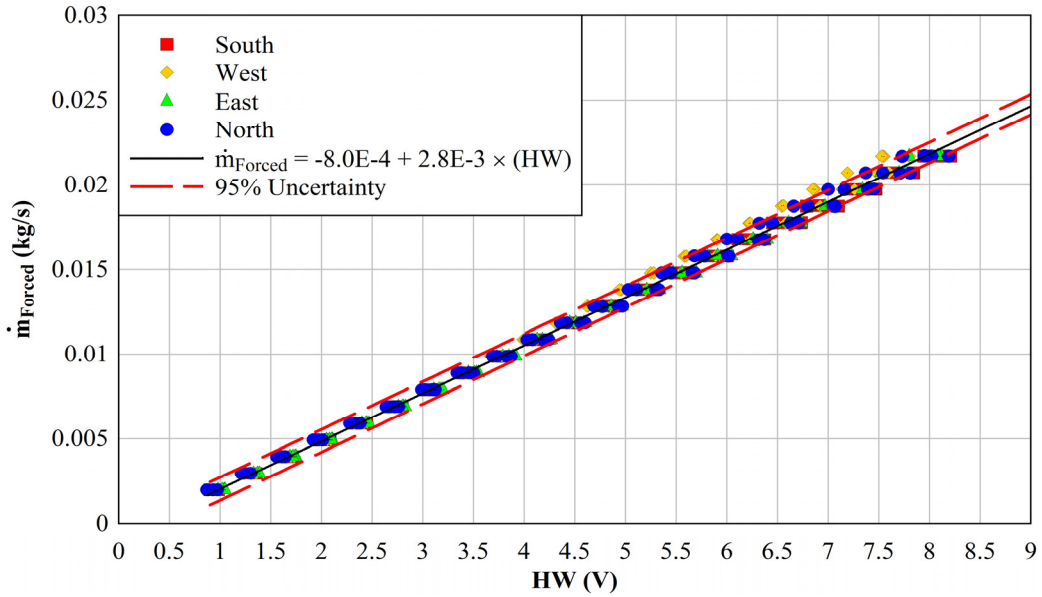

Figure 2.20 Mass flow rate as a function of hot wire output for forced flow.

2.4.2.2 Inlet Duct Flow Profiles

Velocity profiles were collected across the short dimension (0.100 m) at the end of each powered test. The profiles were measured with the hot wire anemometer along the *x*-axis of the duct at 0.229 m (9.00 in.) from the duct entrance as shown in Figure 2.21.

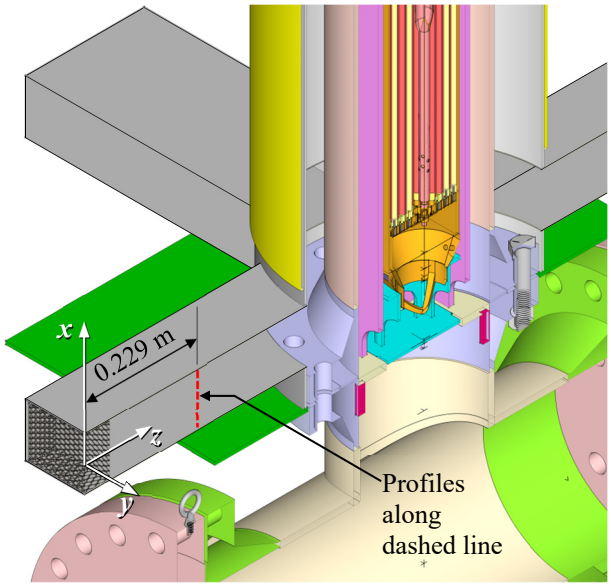

Figure 2.21 Schematic showing the location of the inlet duct profiles for aboveground testing.

These velocity profiles were integrated to determine the relationship of the air mass flow rate during heated, buoyancy-driven testing to that measured during the forced flow testing. The integrated, natural air mass flow rate is given in Equation 2.1. Here, the reference density is defined by the standard conditions for the TSI hot wires, or $\rho_{ref} = 1.2$ kg/m^3 at 21.1 °C and 101.4 kPa. The area for each measurement is given by the product of the profile step size, Δx, and the width of the inlet duct (W = 0.229 m). Figure 2.22 gives a visual representation of the integration scheme.

$$\dot{m}_{Natural} = \sum_{j=1}^{N} \rho_{ref} \cdot \Delta x \cdot W \cdot w_j \qquad 2.1$$

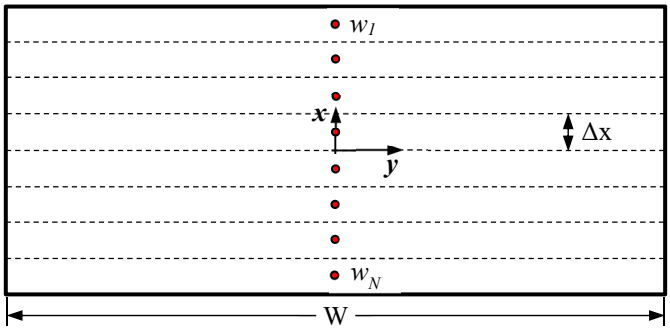

Figure 2.22 Diagram showing the integration scheme for the calculation of air mass flow rate for the aboveground configuration.

2.4.2.3 Natural-to-Forced Flow Correlation

Air mass flow rates from the natural (integrated profiles) and forced (mass flow controller) methods were compared after testing. Recall, flow velocity data was collected with the hot wires centrally located in the ducts during general testing and was converted to mass flow rate using the pre-test forced flow correlations. Velocity profiles were recorded only at the end of each heated test when steady state was achieved. This comparison as shown in Figure 2.23 revealed that the natural air mass flow rate was less than that indicated from the forced flow correlation by a factor of 0.9344. Therefore, the two correlations are applied successively to the hot wire voltage to obtain the best estimate of air mass flow rate. Comparisons of velocity profiles revealed that the boundary layer for the natural flow was larger than the forced flow case. This difference corresponded to the lower observed mass flow rate for natural conditions.

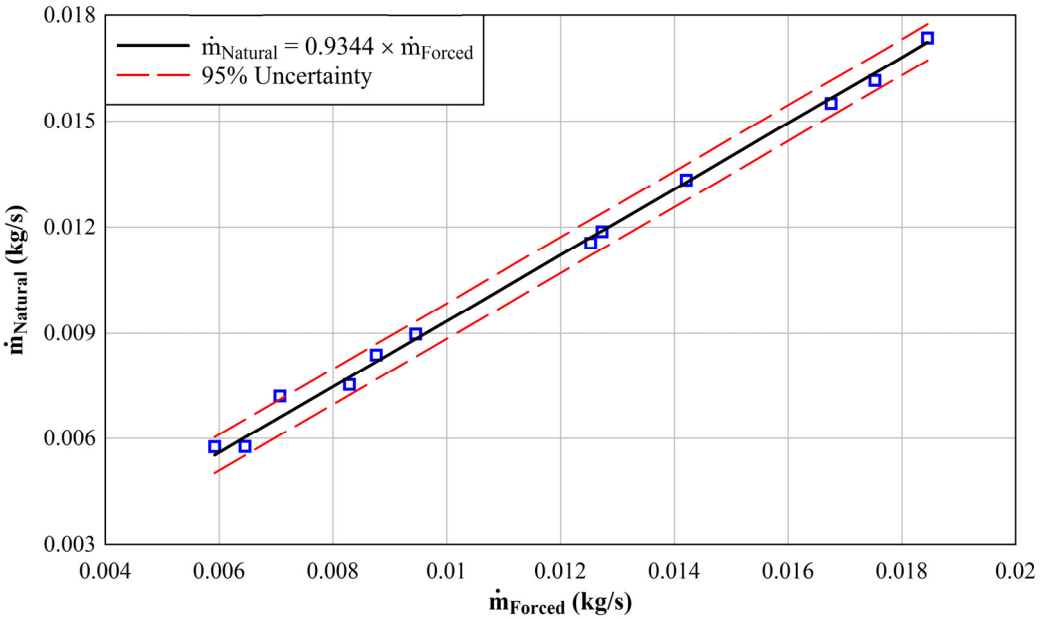

Figure 2.23 Natural-to-forced flow correlation.

2.4.3 Belowground Air Flow Measurement

The inlet and hot wire arrangement for the belowground configuration is shown in Figure 2.24. Velocity profiles were collected across the annular gap defined by shell 1 and shell 2 during heated testing at z = 0.508 m (20.00 in.) or 3.336 m (131.37 in.) from the bottom of the inlet duct. The profiles were measured from the inner surface of shell 2 to the outer surface of the insulation attached to shell 1 as shown in Figure 2.24.

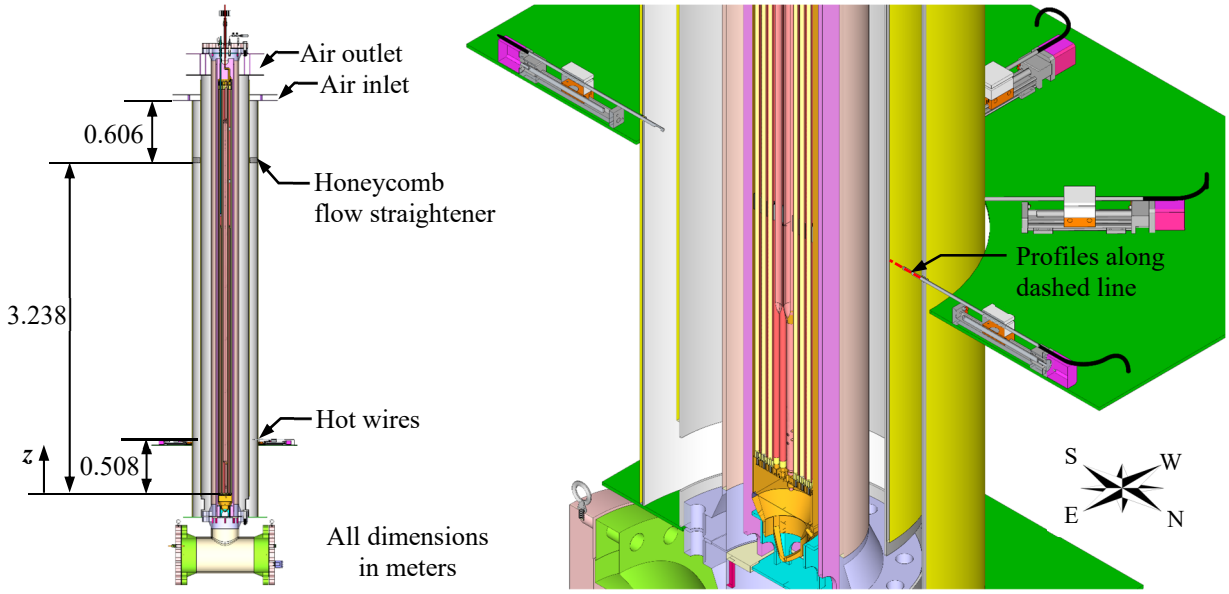

Figure 2.24 Location of air flow measurement instrumentation for the belowground configuration.

Figure 2.25 shows the radial positioning for the hot wire anemometers for the both phases of the belowground testing. The first arrangement with eight equally spaced hot wires was used for powered

testing without cross-wind. Four additional hot wires were added in the second configuration along one half of the annulus to measure larger velocity gradients than possible with 45° spacing.

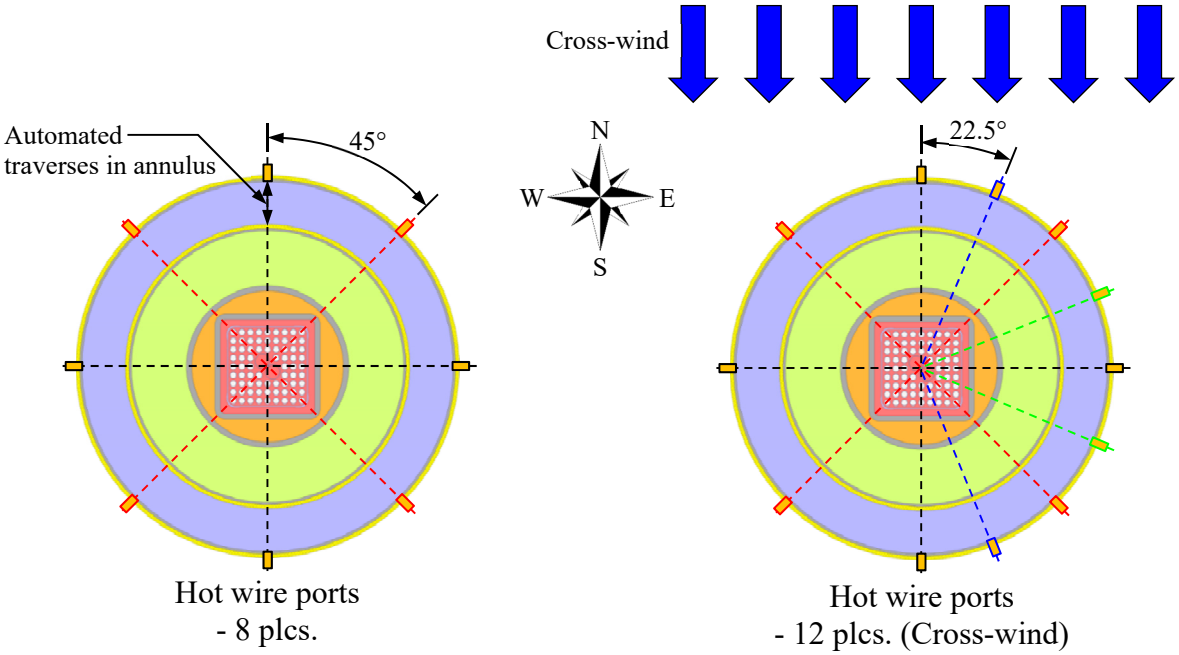

Figure 2.25 Radial positioning of the hot wire anemometers for belowground testing.

The velocity profiles from the hot wires were integrated to calculate the air mass flow rate during heated, buoyancy-driven testing. The integrated, natural air mass flow rate is given in Equation 2.2. Again, the reference density is defined by the standard conditions for the TSI hot wires, or $\rho_{ref} = 1.2$ kg/m^3 at 21.1 °C and 101.4 kPa. The area for each measurement is given by the product of the radius, r, profile step size, Δr, and the arc angle in radians, θ. The arc angle for a given hot wire is assumed to bisect the azimuths formed between the index hot wire and the nearest hot wires. The first index is defined as the hot wire identifier. The second index denotes the radial position. Figure 2.26 gives a visual representation of the integration scheme.

$$\dot{m}_{Natural} = \sum_{i=1}^{M}\sum_{j=1}^{N} \rho_{ref} \cdot \theta_i \cdot r_j \cdot \Delta r \cdot w_{i,j} \qquad 2.2$$

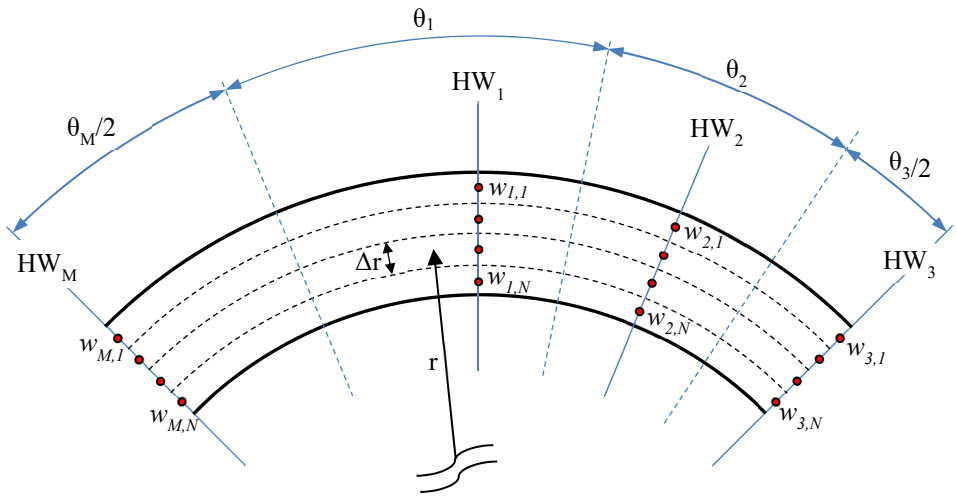

Figure 2.26 Diagram showing the integration scheme for the calculation of air mass flow rate for the belowground configuration.

2.5 Cross-Wind Testing

A wind machine was fabricated and installed in the CYBL vessel to study the effect of a continuous cross-wind on the thermal and hydraulic response of the system. This wind machine consisted of three air-driven blowers connected to a specially fabricated duct with outlet dimensions of 1.295 × 0.762 m (51.0 × 30.0 in.). The duct served two purposes. First, it redirected the flow from a vertical orientation to a horizontal direction via a long-sweep elbow. Second, the duct allowed the insertion of flow straightening elements to make the air velocity at the outlet as uniform as reasonably achievable. The top and bottom of the wind machine duct outlet were installed approximately 0.12 m (4.625 in.) above the DCS air outlet and 0.18 m (7.25 in.) below the DCS air inlet, respectively. The distance between the outer edge of the DCS air inlet and the duct outlet was 0.17 m (6.75 in.). The wind machine was centered side-to-side on the DCS assembly with the duct extending 0.13 m (5.25 in.) on either side of the DCS air inlet. Figure 2.27 shows the position of the wind machine relative to the assembly. A local coordinate system for the wind machine is defined in Figure 2.28.

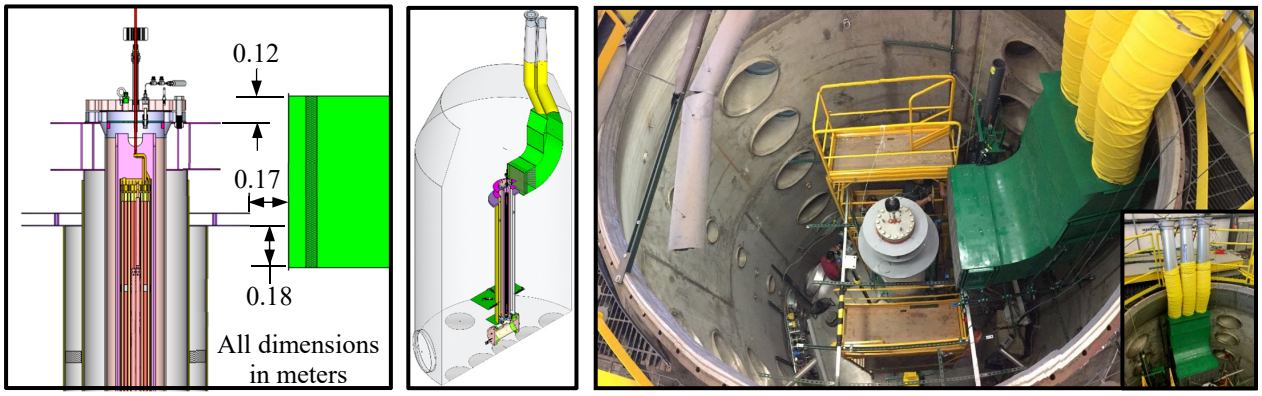

Figure 2.27 Layout of the cask simulator and wind machine for cross-wind testing.

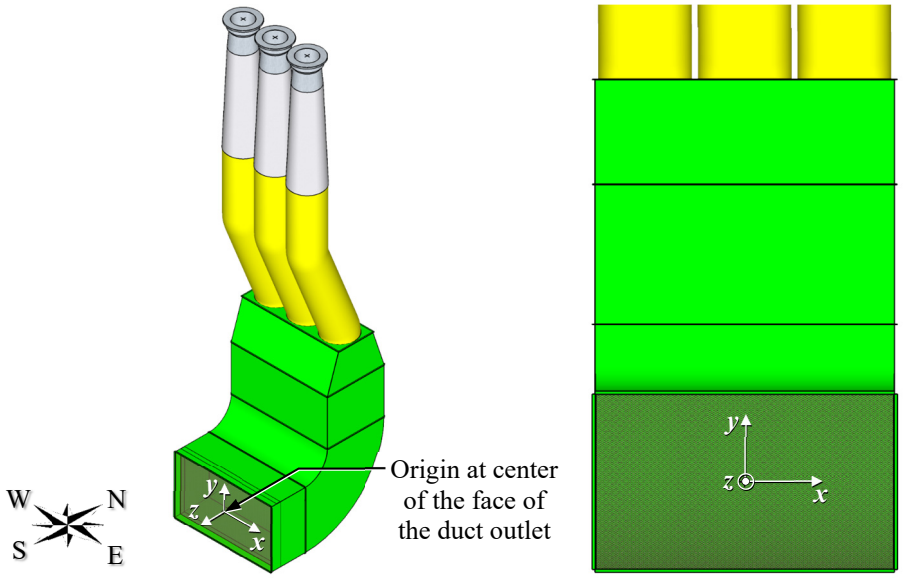

Figure 2.28 Schematic showing the local coordinates of the wind machine.

Hot wire measurements were taken across the wind machine outlet to determine wind speed and uniformity. Prior to heated testing, hot wire measurements were taken for three different wind speeds at 45 regularly spaced locations. Figure 2.29 shows the velocity contours of one such effort near the upper range of achievable wind speeds ($W_{2D, avg}$ = 5.2 m/s {11.6 mph}). For heated cross-wind testing, two-dimensional mapping was not possible. Therefore, hot wire anemometers were fixed at three locations as shown in Figure 2.29. Figure 2.30 gives the correlation between the integrated average velocity ($W_{2D, avg}$) and the average of the three hot wires ($W_{3\text{-}Pt, avg}$). This correlation was applied to the 3-point average to provide an estimate of the average wind speed at the outlet of the wind machine for heated testing.

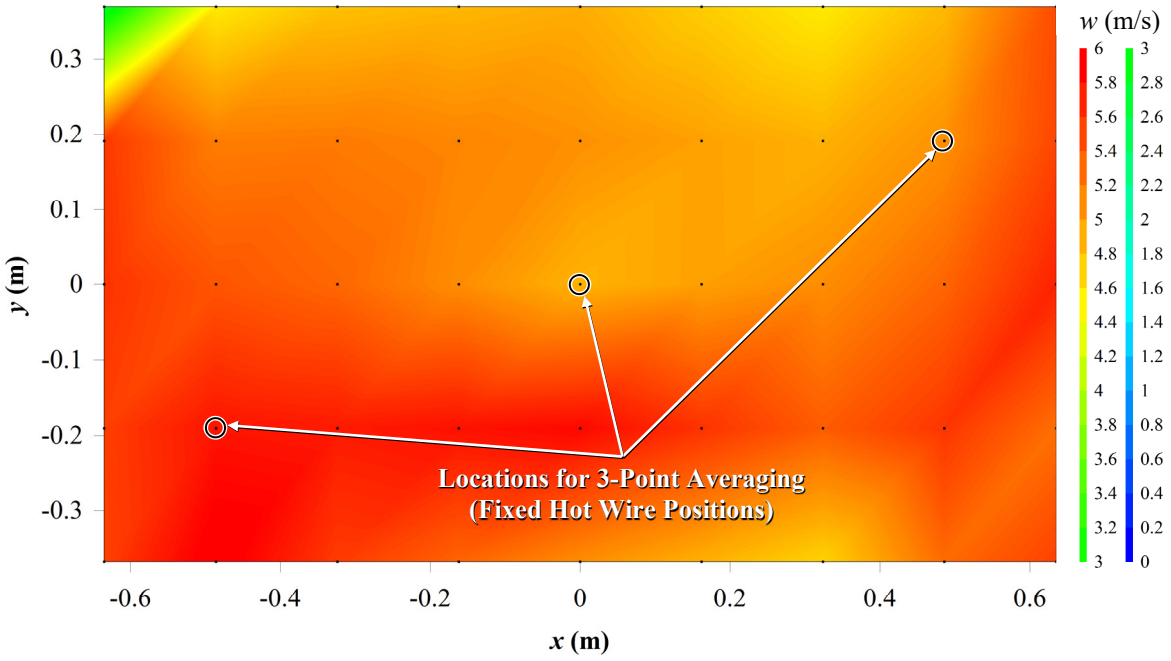

Figure 2.29 Velocity contours of the wind machine for maximum cross-wind.

Note: The fixed positions of the hot wires used for the 3-point average wind speed are marked in the figure.

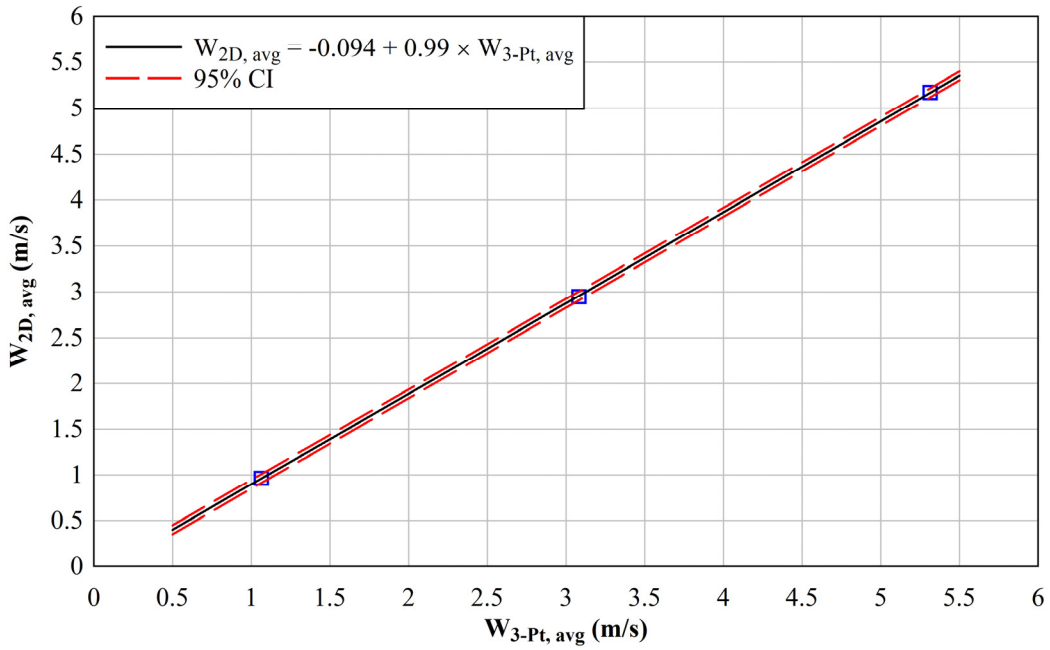

Figure 2.30 Correlation of the two-dimensional, integrated average velocity ($W_{2D, avg}$) to the average of the three fixed hot wire anemometers ($W_{3\text{-}Pt, avg}$).

This page intentionally blank.

3 ABOVEGROUND RESULTS

3.1 Steady State Analyses

A total of fifteen tests were conducted where the apparatus achieved steady state for various assembly powers and pressures. The power levels tested were 0.5, 1.0, 2.5, and 5.0 kW. The vessel pressures tested were vacuum (0.3 kPa), 100, 450, and 800 kPa absolute. A scaling analysis [Durbin, *et al.*, 2016] showed that elevated powers up to 5.0 kW were warranted to drive the induced air flow to prototypic levels.

The criterion for steady state was considered met when the first derivative with respect to time of any given TC in the test apparatus was ≤ 0.3 K/h. The steady state values reported here represent the average of data collected between the "start of steady state" and the end of the test.

3.1.1 Peak Cladding Temperature and Air Mass Flow Rate

Figure 3.1 and Figure 3.2 present the steady state data as peak cladding temperature (PCT) and total induced air flow rate, respectively, as a function of power for each vessel pressure tested. Figure 3.3 and Figure 3.4 present the same PCT and flow data but as a function of vessel pressure for each power tested. Generally, the peak temperatures and induced air flow both increased significantly with power level and decreased slightly with helium pressure. The notable exception was that the peak cladding temperature increased significantly as the vessel pressure was decreased from 100 kPa absolute helium to 0.3 kPa absolute air. Recall that subatmospheric testing resulted in a vessel gas composition of air due to the leak path discussed in Section 2.3.2.

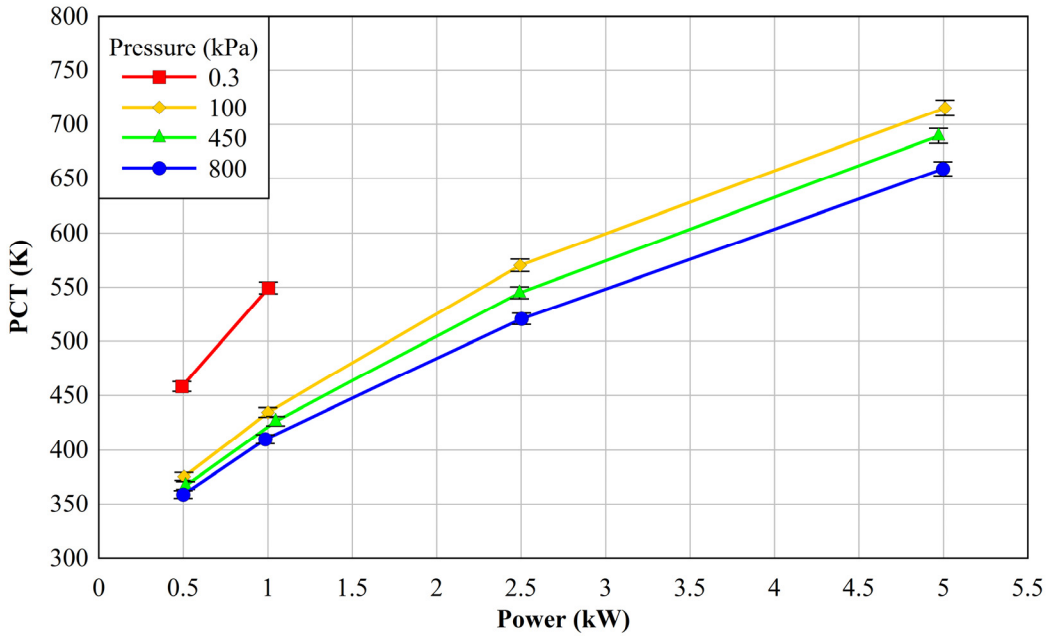

Figure 3.1 Steady state peak cladding temperature as a function of power.

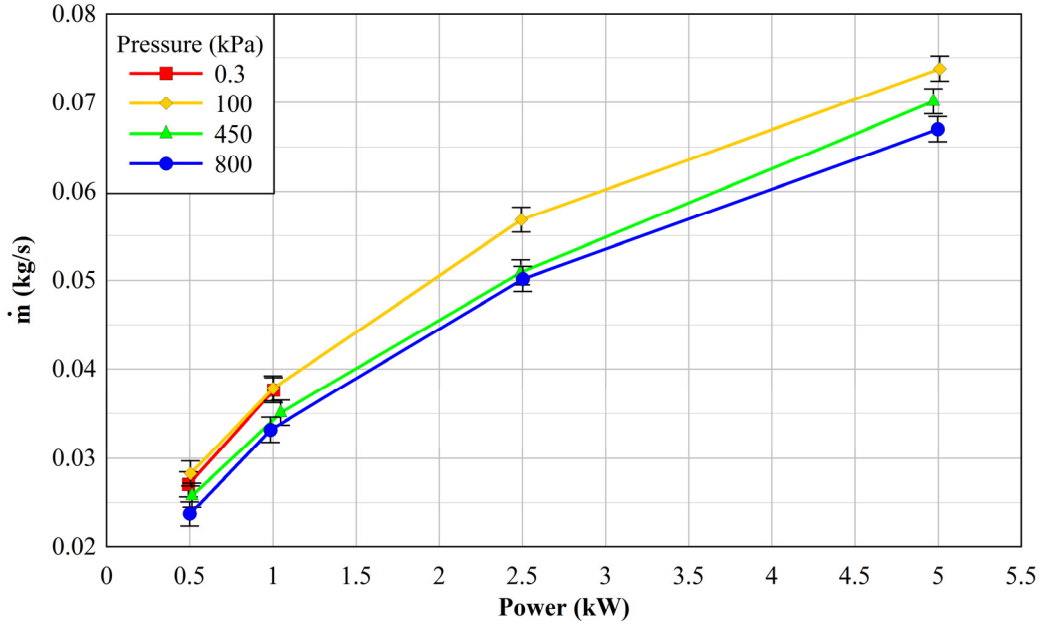

Figure 3.2 Steady state air flow rate as a function of power.

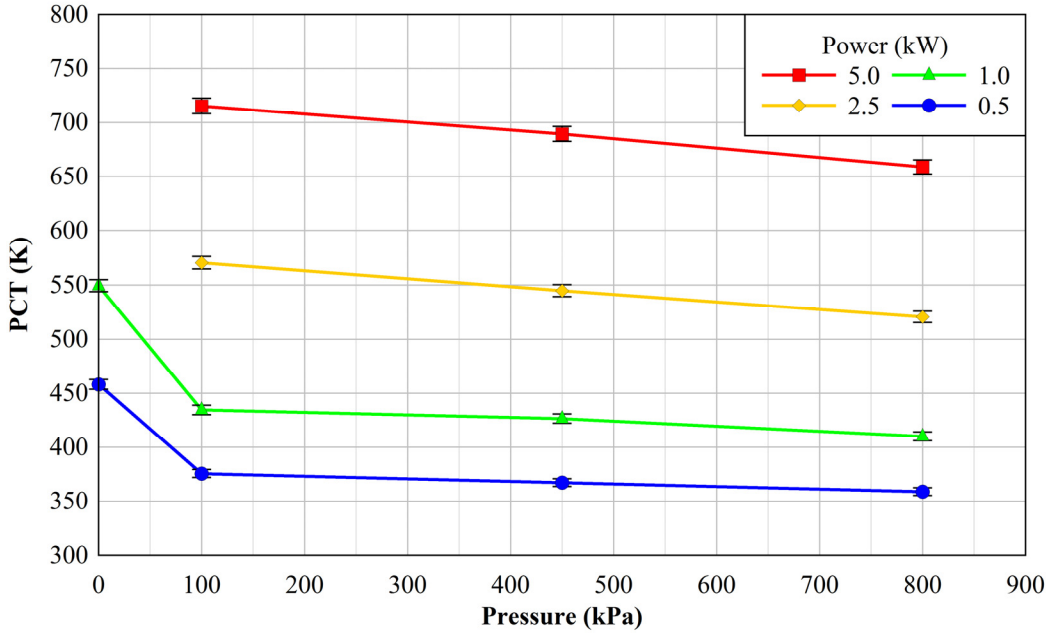

Figure 3.3 Steady state peak cladding temperature as a function of absolute internal vessel pressure.

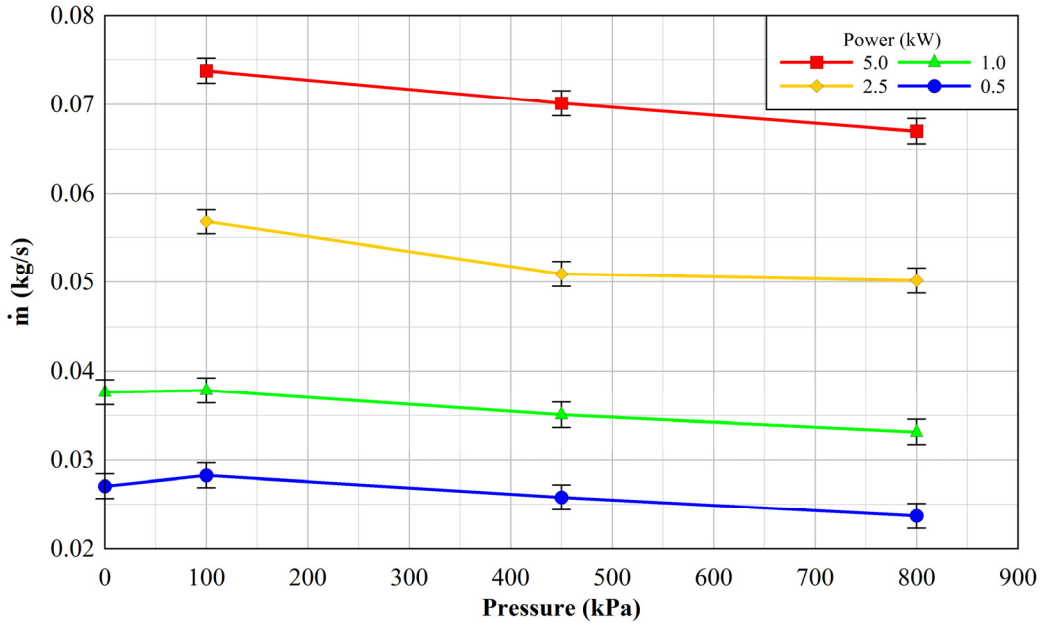

Figure 3.4 Steady state air mass flow rate as a function of absolute internal vessel pressure.

3.1.2 Two-Dimensional Temperature Contours

Figure 3.5 shows 2-D temperature contour plots from the center of the assembly through the basket, pressure vessel, shell 1, and ambient for the high-power tests (5.0 kW) at the three helium pressures tested (100, 450, and 800 kPa absolute). Figure 3.6 shows 2-D temperature contour plots for the low power tests (0.5 kW) at the four vessel pressures tested (0.3, 100, 450 and 800 kPa absolute). For both power levels, the peak temperatures decreased with increasing vessel pressure. The location of the PCT also shifted from ~1/3 of the assembly height to near the top of the assembly for vessel pressures of 0.3 to 800 kPa, respectively.

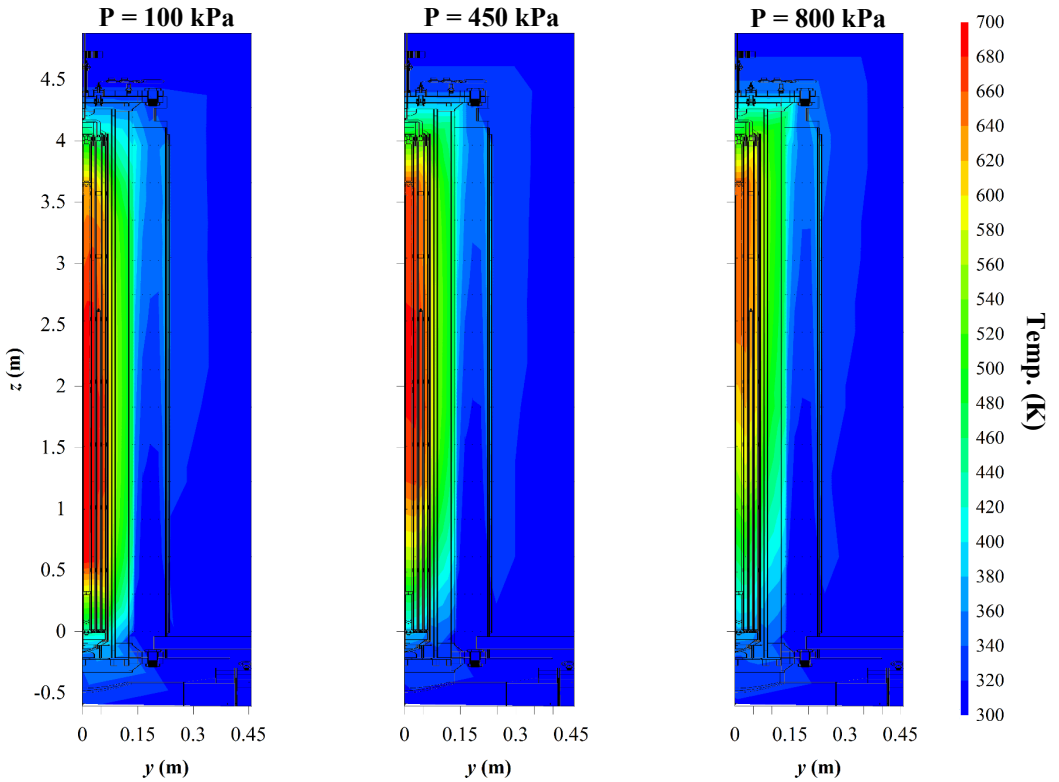

Figure 3.5 Steady state temperature contours for 5.0 kW at different internal helium pressures.

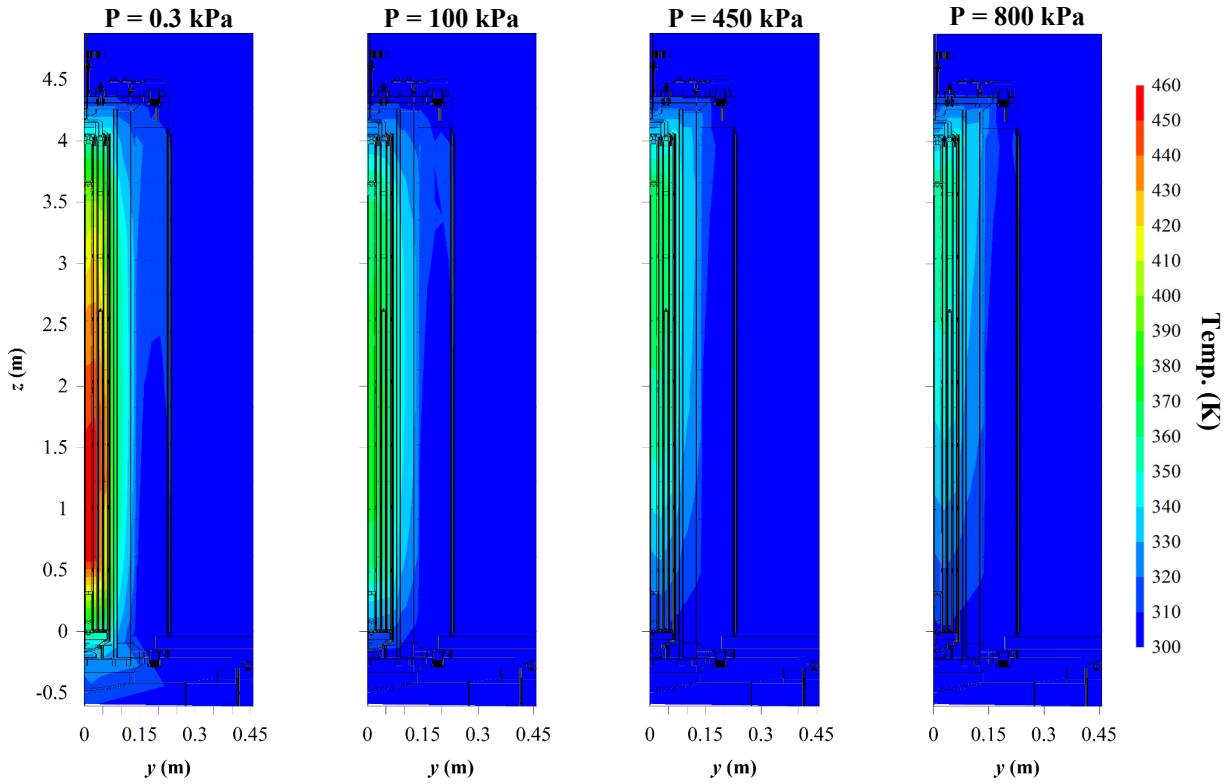

Figure 3.6 Steady state temperature contours for 0.5 kW at different internal vessel pressures.

3.1.3 Transverse Temperature Profiles including the TC Lance

Figure 3.7 shows the steady state transverse temperature profile at the z = 3.023 m elevation for the 5.0 kW and 800 kPa aboveground case. Figure 3.8 shows a similar steady state transverse temperature profile at the 3.023 m elevation for the 0.5 kW and 800 kPa case. The TC lance was located at y = -0.042 m. The assembly TCs for comparison with the TC lance were located starting at x = 0 m and continued along the negative x-direction. Assuming symmetry, the lance is plotted on the x-axis. The TC lance was in good agreement with the interpolated temperature of the two closest assembly TCs.

As received and installed, the lance TCs above the 3.023 m (119 in.) elevation exhibited anomalous behavior during some tests as discussed in detail in **Error! Reference source not found.**. TC lance data for the 3.023 m (119 in.) elevation is presented because no anomalous behavior was evident. A modification was made to the TC lance that eliminated the anomalous behavior for the affected TCs shortly before cross-wind testing of the belowground configuration, which was the last phase of testing. The behavior of the TCs at the 3.023 m (119 in.) elevation and below was not impacted by the modification.

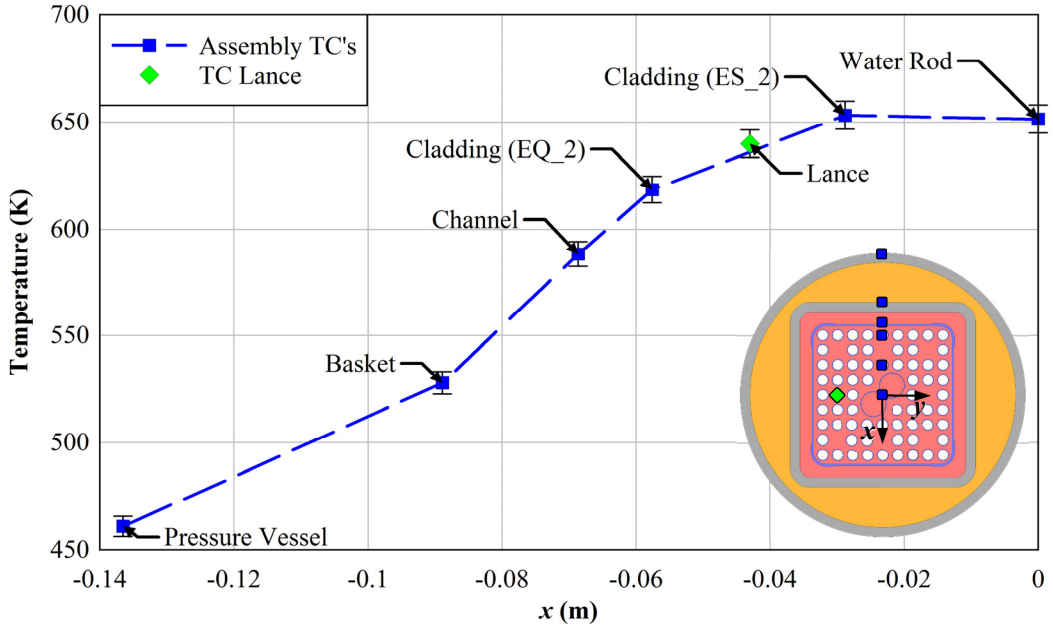

Figure 3.7 Steady state transverse temperature profile at z = 3.023 m (119 in.) for the test conducted at 5.0 kW and 800 kPa helium.

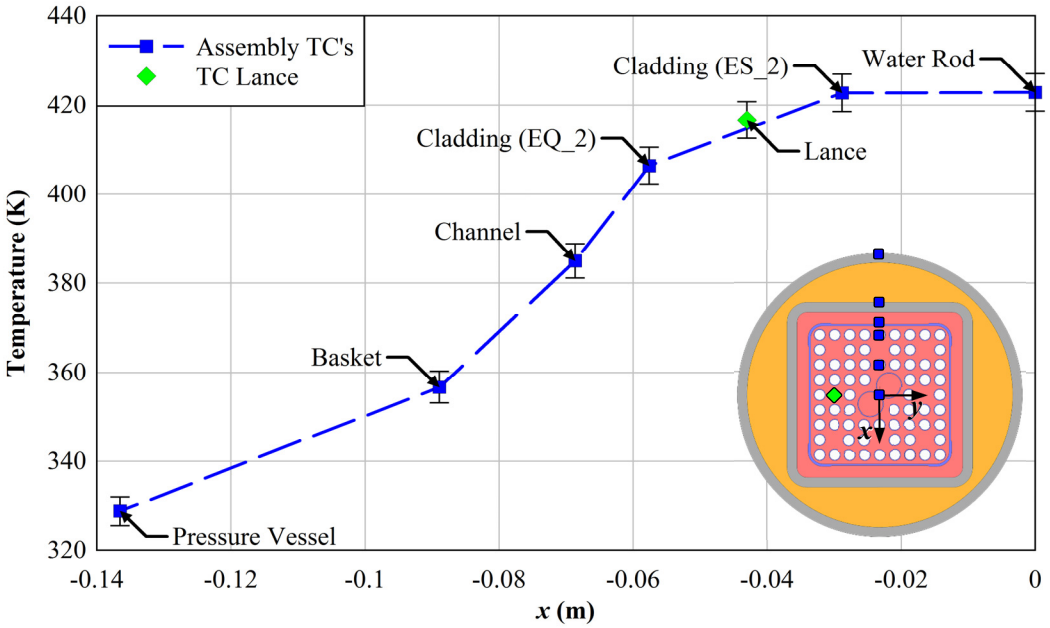

Figure 3.8 Steady state transverse temperature profile at z = 3.023 m (119 in.) for the test conducted at 0.5 kW and 0.3 kPa air.

3.1.4 Summary Data Tables

The steady-state value of the peak temperature for each region of the test apparatus is presented in the following summary tables. Table 3.1 through Table 3.4 present these peak temperatures and corresponding location along with the measured power, ambient temperature, and induced air mass flow rate for each power level tested at a given vessel pressure. The corresponding minimum and maximum values over the steady-state measurement period are also presented.

Table 3.1 Steady state results for the primary assembly measurements at 0.3 kPa air.

Nominal Power (kW)		Power (kW)	Cladding (K)	Channel (K)	Basket (K)	Vessel (K)	Shell 1 (K)	Ambient (K)	Air Flow Rate (kg/s)
0.5	Average	0.492	458	404	361	328	312	299	2.53E-02
	Max	0.510	459	405	362	330	315	303	2.87E-02
	Min	0.472	456	403	361	328	311	296	2.17E-02
	Location		DT_2_48	Channel_4_48	Basket_3_72	PV_2_108	S1_2_119	All	Assembly Total
1	Average	1.004	549	470	406	351	323	301	3.51E-02
	Max	1.041	550	471	407	352	324	303	3.84E-02
	Min	0.934	549	470	406	351	322	299	3.14E-02
	Location		DT_1_24	Channel_4_48	Basket_3_72	PV_1_96	S1_2_119	All	Assembly Total

Table 3.2 Steady state results for the primary assembly measurements at 100 kPa helium.

Nominal Power (kW)		Power (kW)	Cladding (K)	Channel (K)	Basket (K)	Vessel (K)	Shell 1 (K)	Ambient (K)	Air Flow Rate (kg/s)
0.5	Average	0.504	376	359	344	328	312	298	2.64E-02
	Max	0.525	376	359	344	328	312	300	2.88E-02
	Min	0.482	375	359	344	328	311	296	2.44E-02
	Location		FV_3_72	Channel_4_72	Basket_4_96	PV_2-3_119	S1_2_119	All	Assembly Total
1	Average	1.001	434	405	378	350	321	299	3.53E-02
	Max	1.017	435	405	379	350	321	301	3.75E-02
	Min	0.985	434	404	378	349	321	298	3.21E-02
	Location		FV_3_72	Channel_4_72	Basket_3_72	PV_2-3_119	S1_2_119	All	Assembly Total
2.5	Average	2.493	570	511	461	403	348	300	5.31E-02
	Max	2.516	570	511	461	403	348	302	5.61E-02
	Min	2.471	570	511	460	402	347	298	5.02E-02
	Location		DT_2_48	Channel_3_60	Basket_3_72	PV_2-3_119	S1_2_119	All	Assembly Total
5	Average	5.010	715	630	554	467	387	301	6.89E-02
	Max	5.039	716	631	555	468	389	305	7.21E-02
	Min	4.969	714	628	553	466	385	299	6.54E-02
	Location		DT_2_48	Channel_4_48	Basket_3_72	PV_2-3_119	S1_2_119	All	Assembly Total

Table 3.3 Steady state results for the primary assembly measurements at 450 kPa helium.

Nominal Power (kW)		Power (kW)	Cladding (K)	Channel (K)	Basket (K)	Vessel (K)	Shell 1 (K)	Ambient (K)	Air Flow Rate (kg/s)
0.5	Average	0.513	367	353	341	326	311	296	2.41E-02
	Max	0.529	367	353	341	327	312	299	2.66E-02
	Min	0.489	367	352	340	326	310	293	2.07E-02
	Location		FV_3_144	Channel_2_119	Basket_3_132	PV_2-3_119	S1_4_159	All	Assembly Total
1	Average	1.047	426	399	377	351	323	299	3.28E-02
	Max	1.073	427	399	377	351	324	302	3.63E-02
	Min	1.018	425	397	376	350	322	295	2.82E-02
	Location		FV_3_144	Channel_2_119	Basket_3_132	PV_3_144	S1_4_159	All	Assembly Total
2.5	Average	2.491	545	494	451	401	346	300	4.76E-02
	Max	2.551	546	495	452	402	348	303	5.06E-02
	Min	2.456	543	492	449	399	345	299	4.52E-02
	Location		DT_1_96	Channel_2_119	Basket_2_108	PV_2-3_119	S1_3_132	All	Assembly Total
5	Average	4.972	689	612	547	465	384	299	6.55E-02
	Max	5.030	690	613	548	466	386	302	6.87E-02
	Min	4.910	689	611	547	464	383	297	6.16E-02
	Location		DT_1_96	Channel_1_84	Basket_2_108	PV_2-3_119	S1_2_119	All	Assembly Total

Table 3.4 Steady state results for the primary assembly measurements at 800 kPa helium.

Nominal Power (kW)		Power (kW)	Cladding (K)	Channel (K)	Basket (K)	Vessel (K)	Shell 1 (K)	Ambient (K)	Air Flow Rate (kg/s)
0.5	Average	0.499	359	347	338	329	312	298	2.21E-02
	Max	0.516	359	347	338	329	312	299	2.43E-02
	Min	0.484	358	347	338	329	312	296	1.91E-02
	Location		FV_3_144	Channel_3_144	Basket_4_159	PV_1_156	S1_4_159	All	Assembly Total
1	Average	0.985	410	388	374	356	323	297	3.10E-02
	Max	1.058	410	389	374	356	324	300	3.48E-02
	Min	0.967	410	388	373	355	323	294	2.72E-02
	Location		FV_3_144	Channel_3_144	Basket_4_159	PV_4_159	S1_4_159	All	Assembly Total
2.5	Average	2.503	521	477	444	408	349	298	4.69E-02
	Max	2.547	521	477	444	409	350	303	4.92E-02
	Min	2.444	521	477	443	408	349	296	4.39E-02
	Location		FV_3_144	Channel_3_144	Basket_4_159	PV_4_159	S1_4_159	All	Assembly Total
5	Average	4.997	659	590	533	466	387	300	6.26E-02
	Max	5.021	659	590	533	467	387	303	6.60E-02
	Min	4.956	658	589	532	466	387	299	5.99E-02
	Location		FV_3_144	Channel_3_144	Basket_3_144	PV_4_159	S1_4_159	All	Assembly Total

3.2 Transient Analyses

Figure 3.9 and Figure 3.10 show the peak cladding temperature and total assembly air mass flow rate for each power tested at 800 kPa absolute helium pressure. The air flow rate data was smoothed over a fifteen-minute moving window for clarity of presentation. Ninety-five percent uncertainties are also presented for select data points, 1% of reading for temperature (±7 K maximum) and ±1.5E-3 kg/s for flow rate.

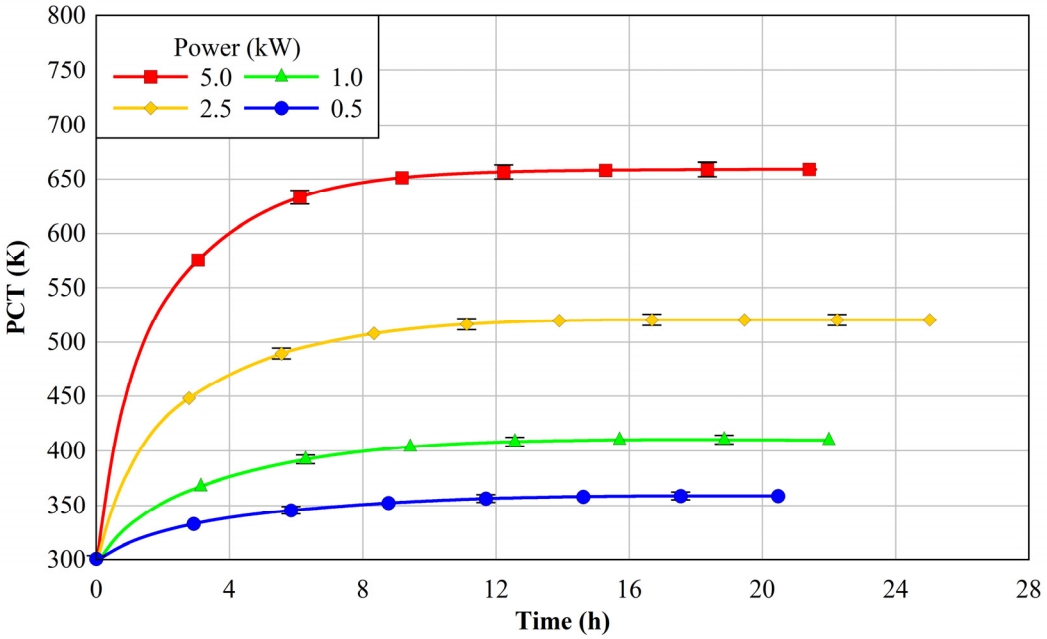

Figure 3.9 Peak cladding temperature as a function of time for tests conducted at 800 kPa helium.

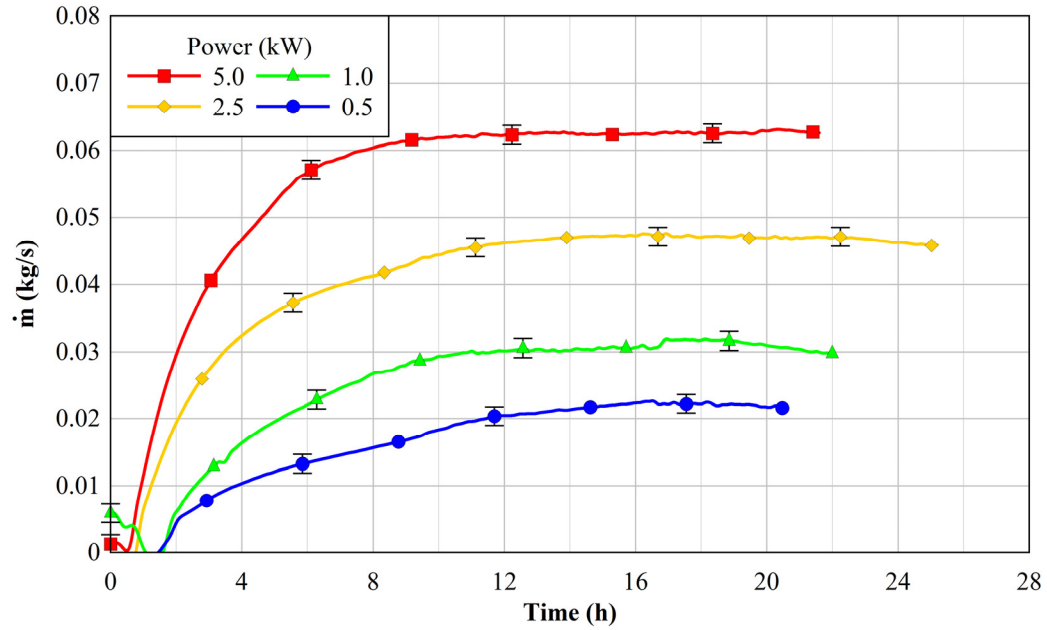

Figure 3.10 Total air mass flow rate as a function of time for tests conducted at 800 kPa helium.

Steady state conditions were reached in about 15 hours. Figure 3.11 shows the time required to reach steady state as function of power for the various test pressures. The time to steady state was independent of power and helium pressure for the 450 kPa and 800 kPa cases. For the 100 kPa helium pressure tests there was a slight dependence on power with 13 hours required at 5.0 kW and 18 hours required at 0.5 kW. The vacuum tests were the most sensitive to power with up to 31 hours required to reach steady state in the 0.5 kW case.

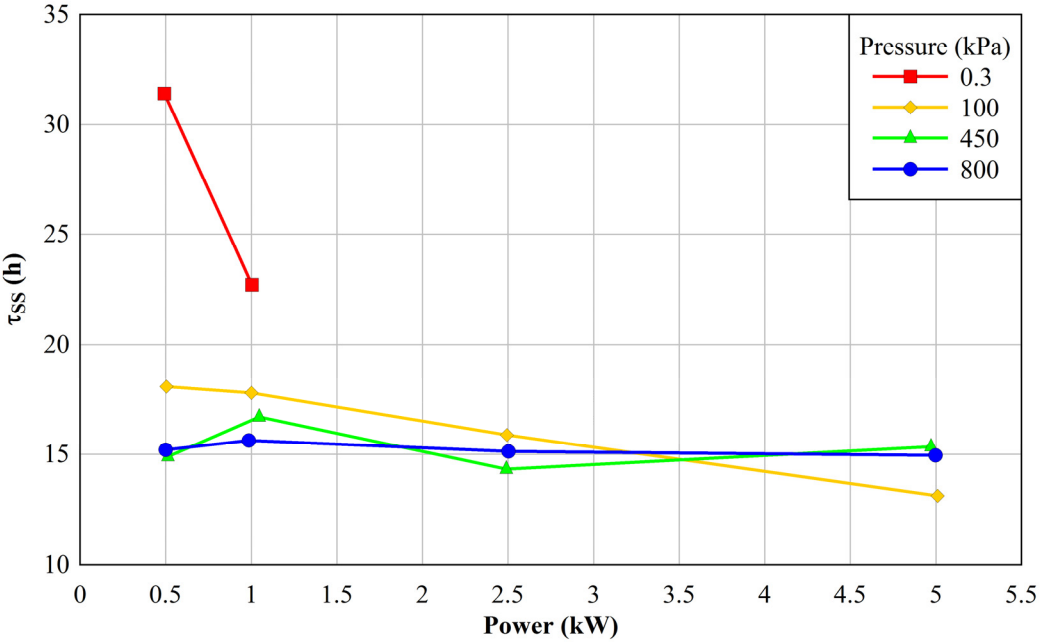

Figure 3.11 Time to reach steady state as a function of power for the various vessel pressures tested.

3.2.1 Transient Response of TC Lance and Corresponding Cladding

Figure 3.12 shows the temperature of the TC lance and adjacent cladding TCs (assuming symmetry) as a function of time at the 3.023 m elevation for the 5.0 kW and 800 kPa case. Figure 3.13 shows the temperature of the TC lance and adjacent cladding TCs at the same elevation for the 0.5 kW and 0.3 kPa case. Ninety-five percent uncertainties are also presented for select data points as 1% of reading for temperature (±7 K maximum). The transient response of the TC lance and the adjacent cladding TCs were similar. The temperature indicated by the lance TC was roughly midway between the adjacent clad TCs. The good agreement provided validation that the TC lance provides an accurate indication of nearby cladding temperatures.

Again, TC lance data for the 3.023 m (119 in.) location is presented because no anomalous behavior was evident at this elevation.

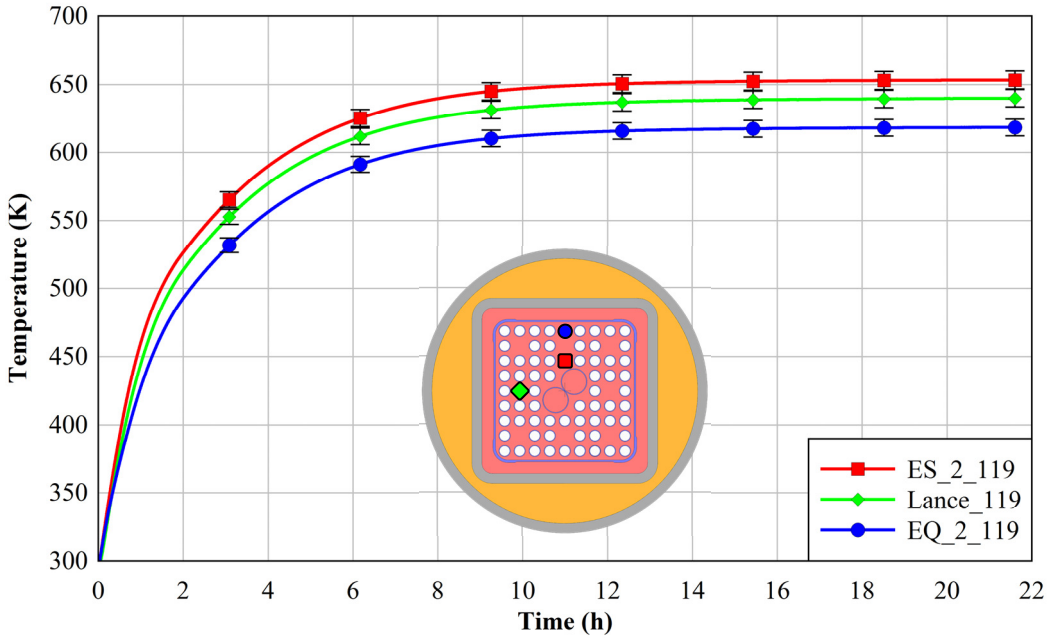

Figure 3.12 Comparison of TC lance and cladding temperatures at z = 3.023 m (119 in.) as a function of time for the test conducted at 5.0 kW and 800 kPa helium.

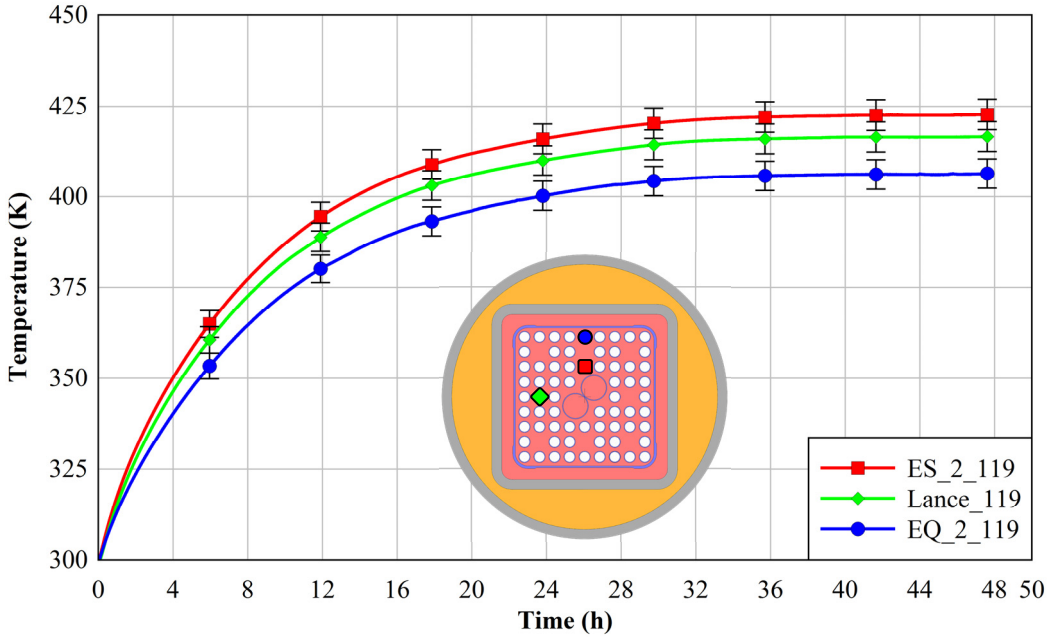

Figure 3.13 Comparison of TC lance and cladding temperatures at z = 3.023 m (119 in.) as a function of time for the test conducted at 0.5 kW and 0.3 kPa air.

This page intentionally blank.

4 BELOWGROUND RESULTS

4.1 Steady State Analyses

A total of fourteen tests were conducted where the apparatus achieved steady state for various assembly powers and vessel pressures. The power levels tested were 0.5, 1.0, 2.5 and 5.0 kW. The vessel pressures tested were vacuum (0.3 kPa), 100, 450 and 800 kPa absolute. A scaling analysis [Durbin, *et al.*, 2016] showed that elevated powers up to 5.0 kW were warranted to drive the induced air flow to prototypic levels.

The criterion for steady state was considered met when the first derivative with respect to time of any given TC in the test apparatus was ≤ 0.3 K/h. The steady state values reported here represent the average of data collected between the "start of steady state" and the end of the test.

4.1.1 Peak Cladding Temperature and Air Mass Flow Rate

Figure 4.1 and Figure 4.2 present the steady state data as peak cladding temperature (PCT) and integrated air mass flow rate in the inlet annulus, respectively, as a function of power for each vessel pressure tested. Figure 4.3 and Figure 4.4 present the same PCT and mass flow rate data but as a function of vessel pressure for each power tested. As in the aboveground configuration, the peak temperatures and induced air mass flow rate for the belowground configuration both increased significantly with power level and decreased slightly with helium pressure. The notable exception was that the peak cladding temperature increased significantly as the vessel pressure was decreased from 100 kPa absolute helium to 0.3 kPa absolute air. Recall that subatmospheric testing resulted in a vessel gas composition of air due to the leak path discussed in Section 2.3.2.

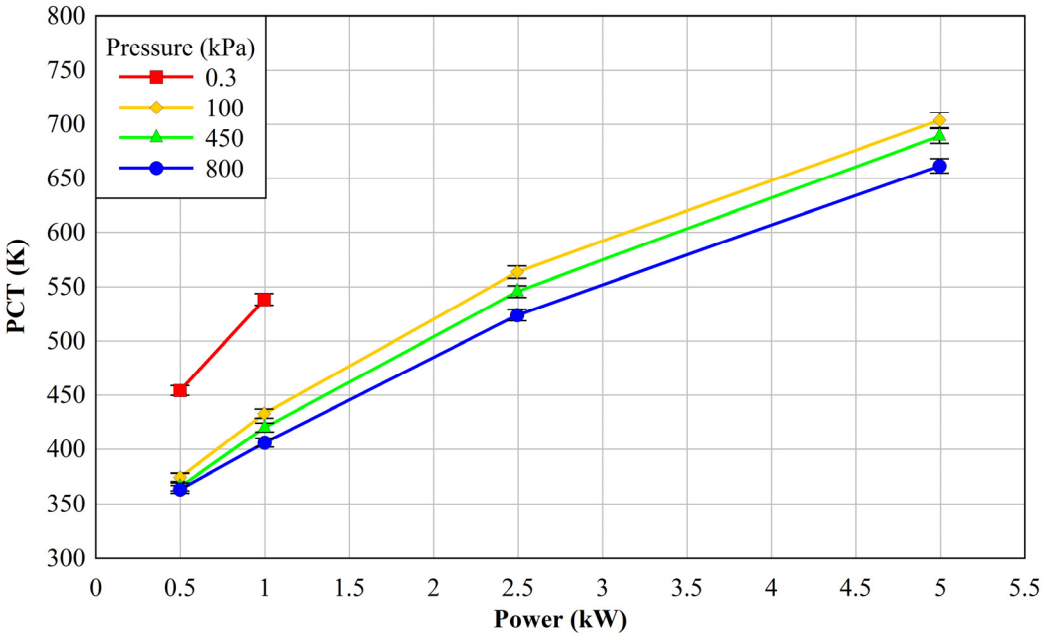

Figure 4.1 Steady state peak cladding temperature as a function of power.

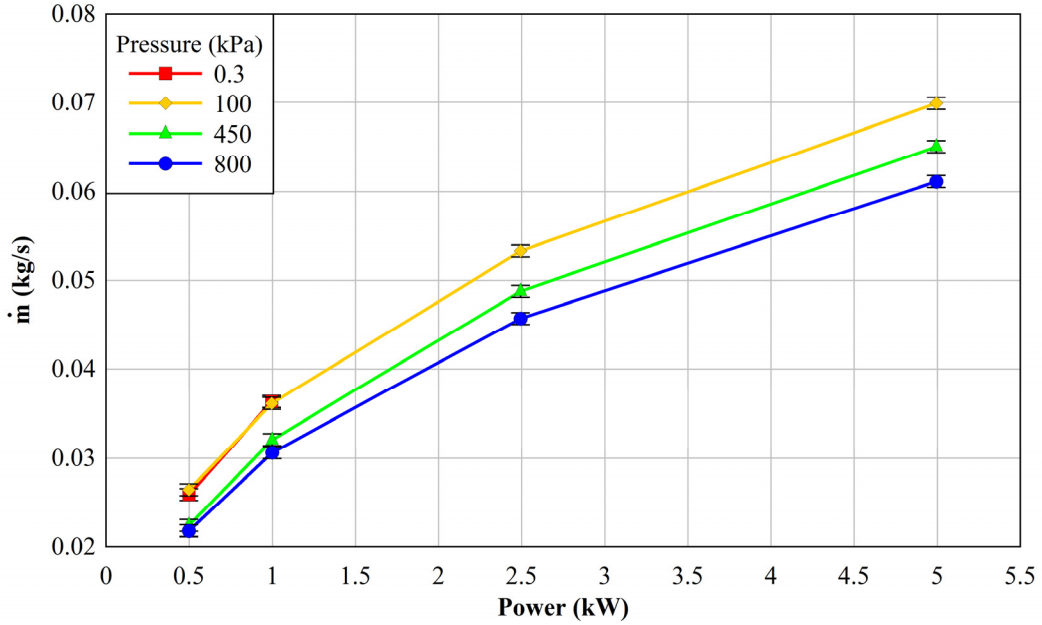

Figure 4.2 Steady state air mass flow rate in the inlet annulus as a function of power.

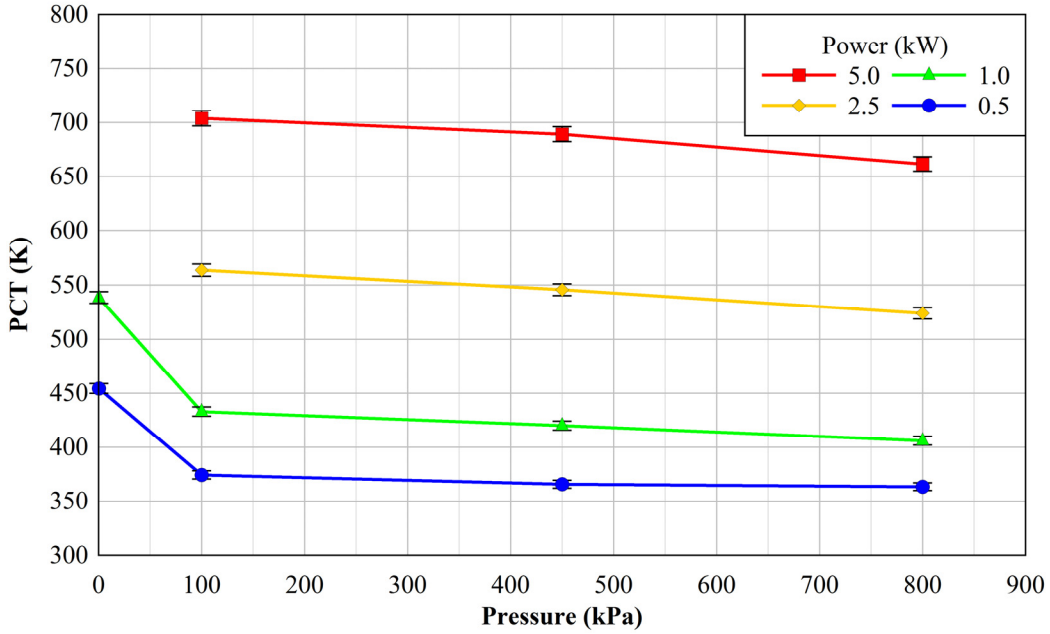

Figure 4.3 Steady state peak cladding temperature as a function of absolute internal vessel pressure.

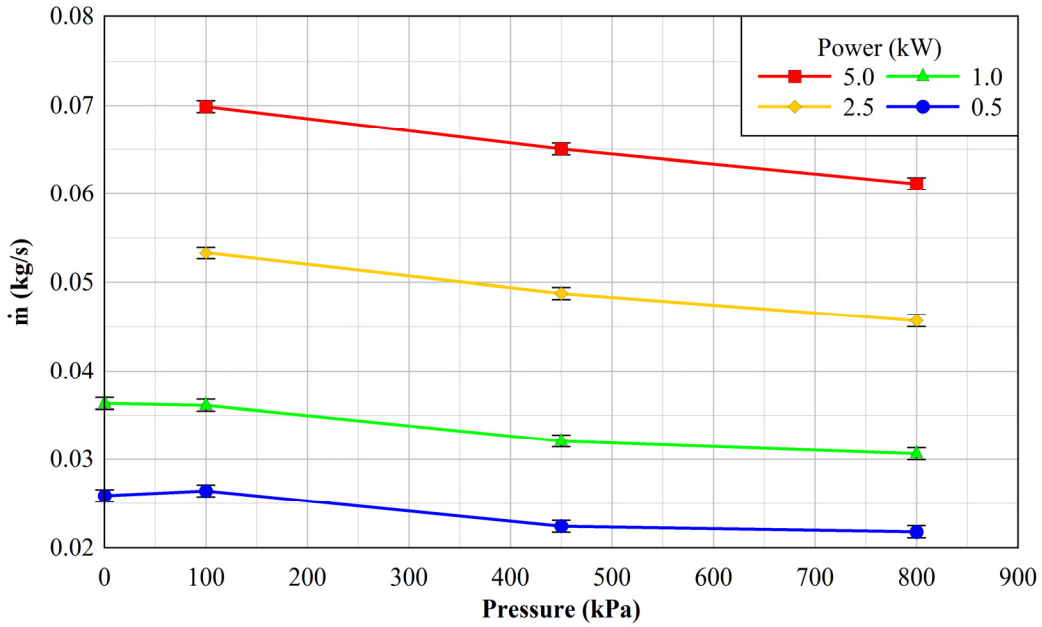

Figure 4.4 Steady state air mass flow rate in the inlet annulus as a function of absolute internal vessel pressure.

4.1.2 Two-Dimensional Velocity Contours

Figure 4.5 shows 2-D velocity contour plots in the inlet annulus of the assembly for the high-power tests (5.0 kW) at the three helium pressures tested (100, 450, and 800 kPa absolute). Figure 4.6 shows 2-D velocity contour plots for the low power tests (0.5 kW) at the four vessel pressures tested (0.3, 100, 450, and 800 kPa absolute).

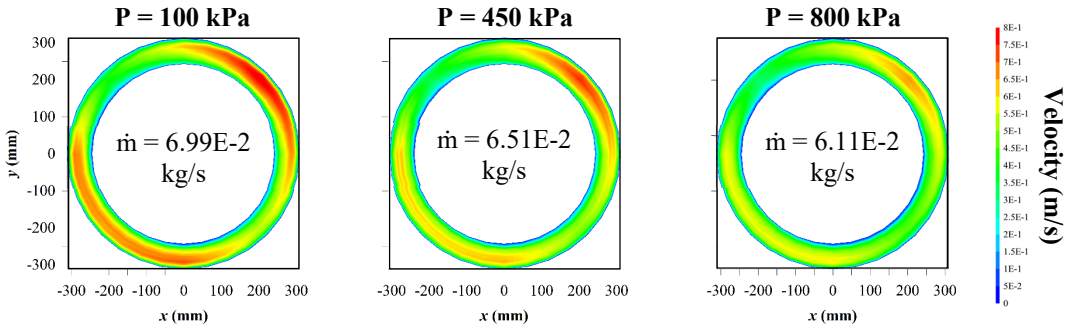

Figure 4.5 Steady state velocity contours for 5.0 kW at different internal helium pressures.

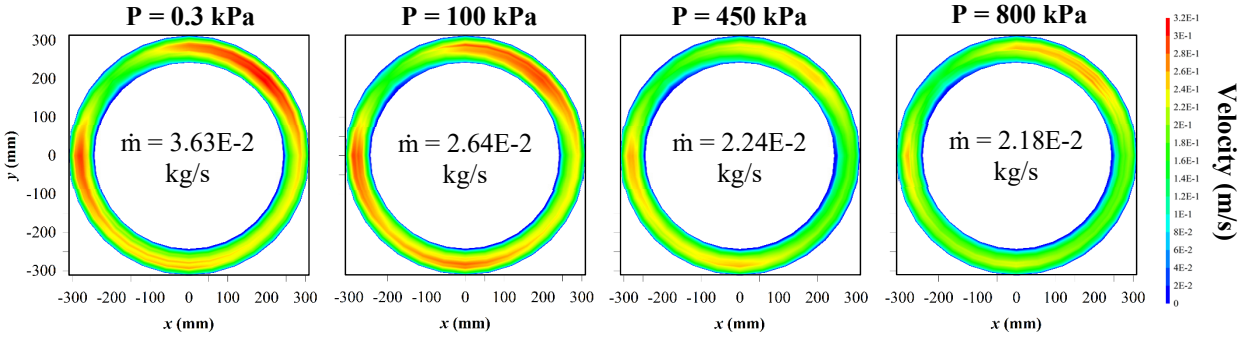

Figure 4.6 Steady state velocity contours for 0.5 kW at different internal vessel pressures.

4.1.3 Transverse Temperature Profiles Including the TC Lance

Figure 4.7 shows the steady state transverse temperature profile at the z = 3.023 m elevation for the 5.0 kW and 800 kPa belowground case. Figure 4.8 shows a similar steady state transverse temperature profile at the 3.023 m elevation for the 0.5 kW and 800 kPa case. The TC lance was located at y = -0.042 m. The assembly TCs for comparison with the TC lance were located starting at x = 0 m and continued along the negative x-direction. Assuming symmetry, the lance is plotted on the x-axis. The TC lance was in good agreement with the interpolated temperature of the two closest assembly TCs.

As received and installed, the lance TCs above the 3.023 m (119 in.) elevation exhibited anomalous behavior during some tests as discussed in detail in **Error! Reference source not found.**. TC lance data for the 3.023 m (119 in.) elevation is presented because no anomalous behavior was evident. A modification was made to the TC lance that eliminated the anomalous behavior for the affected TCs shortly before cross-wind testing of the belowground configuration, which was the last phase of testing. The behavior of the TCs at the 3.023 m (119 in.) elevation and below was not impacted by the modification.

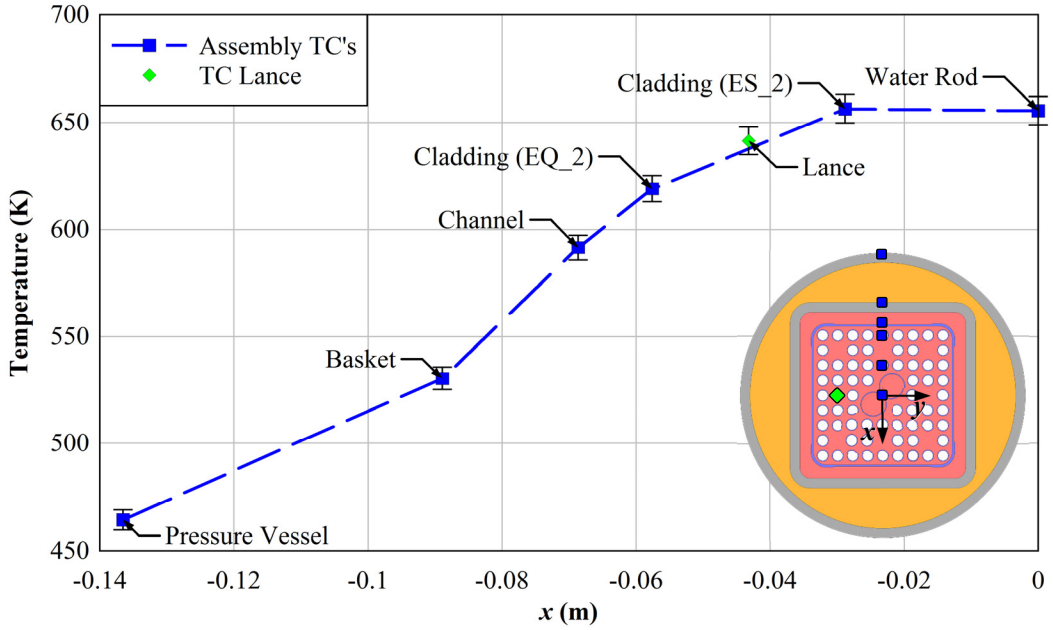

Figure 4.7 Steady state transverse temperature profile at z = 3.023 m (119 in.) for the test conducted at 5.0 kW and 800 kPa helium.

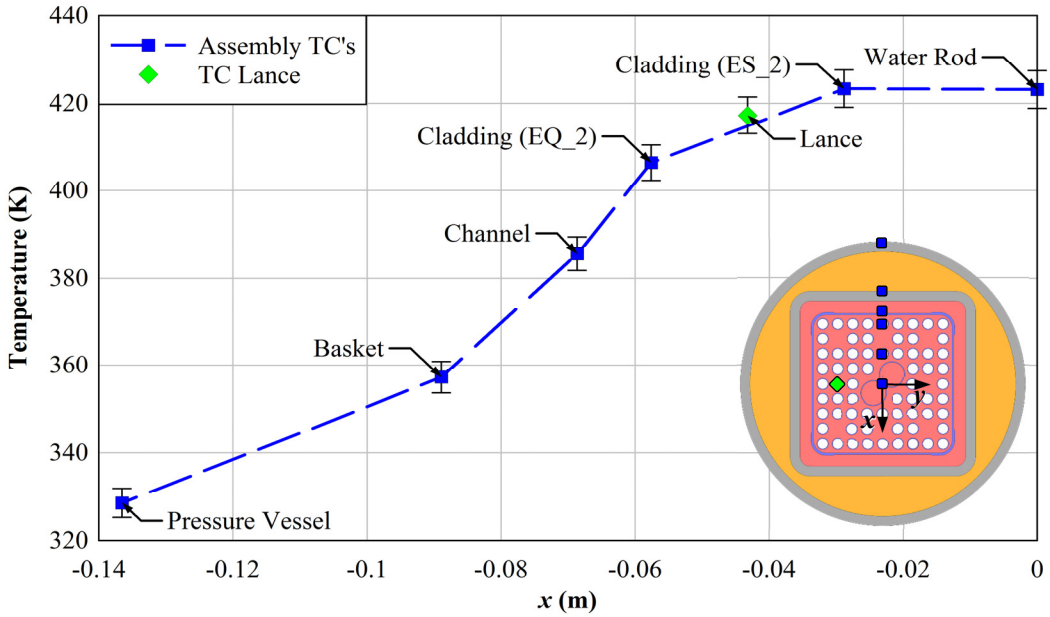

Figure 4.8 Steady state transverse temperature profile at z = 3.023 m (119 in.) for the test conducted at 0.5 kW and 0.3 kPa air.

4.1.4 Summary Data Tables

The steady-state value of the peak temperature for each region of the test apparatus is presented in the following summary tables. Table 4.1 through Table 4.4 present these peak temperatures and corresponding location along with the measured power, ambient temperature, and induced air flow rate for each power level tested at a given vessel pressure. The corresponding minimum and maximum values over the steady-state measurement period are also presented.

Table 4.1 Steady state results for the primary assembly measurements at 0.3 kPa air.

Nominal Power (kW)		Power (kW)	Cladding (K)	Channel (K)	Basket (K)	Vessel (K)	Shell 1 (K)	Shell 2 (K)	Ambient (K)	Air Flow Rate (kg/s)
0.5	Average	0.498	454	403	362	329	313	301	297	2.59E-02
	Max	0.524	455	403	363	330	314	303	299	2.73E-02
	Min	0.468	451	400	360	327	311	300	295	2.46E-02
	Location		DT_2_48	Channel_4_48	Basket_3_72	PV_4_72	S1_4_119	S2_4_48	All	Integrated Total
1	Average	0.996	538	466	406	352	323	304	298	3.63E-02
	Max	1.040	539	466	406	352	325	307	300	3.67E-02
	Min	0.956	537	465	406	351	323	303	296	3.54E-02
	Location		DT_1_24	Channel_4_48	Basket_3_72	PV_1_84	S1_2_119	S2_4_48	All	Integrated Total

Table 4.2 Steady state results for the primary assembly measurements at 100 kPa helium.

Nominal Power (kW)		Power (kW)	Cladding (K)	Channel (K)	Basket (K)	Vessel (K)	Shell 1 (K)	Shell 2 (K)	Ambient (K)	Air Flow Rate (kg/s)
0.5	Average	0.498	374	358	343	327	310	299	295	2.64E-02
	Max	0.523	374	358	343	327	311	301	296	2.67E-02
	Min	0.471	373	357	343	327	310	299	294	2.61E-02
	Location		FV_3_72	Channel_4_72	Basket_3_72	PV_4_72	S1_4_119	S2_4_48	All	Integrated Total
1	Average	0.996	433	403	378	349	321	301	295	3.61E-02
	Max	1.028	433	404	378	349	321	301	297	3.65E-02
	Min	0.967	432	403	377	349	321	300	293	3.58E-02
	Location		FV_3_72	Channel_3_60	Basket_3_72	PV_4_72	S1_2_119	S2_4_48	All	Integrated Total
2.5	Average	2.494	563	508	459	403	349	305	296	5.33E-02
	Max	2.545	564	508	460	403	349	306	297	5.35E-02
	Min	2.446	563	507	459	403	349	305	295	5.29E-02
	Location		DT_2_48	Channel_3_60	Basket_3_72	PV_3-4_72	S1_2_119	S2_2_48	All	Integrated Total
5	Average	4.994	704	624	556	473	394	313	296	6.99E-02
	Max	5.036	704	625	556	474	395	314	298	7.04E-02
	Min	4.954	703	624	556	472	393	312	295	6.94E-02
	Location		DT_2_48	Channel_3_60	Basket_3_72	PV_3-4_72	S1_2_119	S2_4_96	All	Integrated Total

Table 4.3 Steady state results for the primary assembly measurements at 450 kPa helium.

Nominal Power (kW)		Power (kW)	Cladding (K)	Channel (K)	Basket (K)	Vessel (K)	Shell 1 (K)	Shell 2 (K)	Ambient (K)	Air Flow Rate (kg/s)
0.5	Average	0.498	366	351	339	325	309	298	294	2.24E-02
	Max	0.526	366	352	339	325	309	299	297	2.33E-02
	Min	0.469	365	351	338	324	309	298	292	2.14E-02
	Location		DT_2_119	Channel_2_119	Basket_4_119	PV_2-3_119	S1_2_119	S2_4_48	All	Integrated Total
1	Average	0.999	420	394	372	347	320	300	296	3.21E-02
	Max	1.029	420	395	372	348	321	303	297	3.25E-02
	Min	0.967	420	394	371	347	319	300	294	3.12E-02
	Location		DT_2_119	Channel_2_119	Basket_4_119	PV_2-3_119	S1_2_119	S2_4_96	All	Integrated Total
2.5	Average	2.494	546	494	453	402	349	307	298	4.88E-02
	Max	2.538	546	495	453	403	351	309	300	4.93E-02
	Min	2.447	545	494	452	401	349	307	296	4.85E-02
	Location		DT_1_96	Channel_2_108	Basket_2_108	PV_2-3_119	S1_2_119	S2_4_96	All	Integrated Total
5	Average	4.994	689	612	547	466	389	312	296	6.51E-02
	Max	5.030	689	612	548	466	390	313	298	6.57E-02
	Min	4.933	689	612	547	465	389	311	293	6.42E-02
	Location		FV_3_72	Channel_4_72	Basket_2_108	PV_2_108	S1_2_119	S2_1_96	All	Integrated Total

Table 4.4 Steady state results for the primary assembly measurements at 800 kPa helium.

Nominal Power (kW)		Power (kW)	Cladding (K)	Channel (K)	Basket (K)	Vessel (K)	Shell 1 (K)	Shell 2 (K)	Ambient (K)	Air Flow Rate (kg/s)
0.5	Average	0.498	363	351	341	330	314	303	300	2.18E-02
	Max	0.523	364	351	341	330	315	305	302	2.26E-02
	Min	0.468	363	350	340	329	313	303	299	2.06E-02
	Location		FV_3_144	Channel_3_144	Basket_3_144	PV_1_156	S1_4_119	S2_3_72	All	Integrated Total
1	Average	0.999	406	384	367	349	320	301	296	3.06E-02
	Max	1.038	406	384	367	349	320	303	298	3.11E-02
	Min	0.964	405	384	367	349	319	300	294	3.01E-02
	Location		FV_3_144	Channel_3_144	Basket_3_144	PV_1_156	S1_1_144	S2_4_96	All	Integrated Total
2.5	Average	2.494	524	479	443	404	350	310	300	4.57E-02
	Max	2.546	525	479	443	404	351	312	302	4.62E-02
	Min	2.430	524	479	443	403	349	309	299	4.51E-02
	Location		FV_3_144	Channel_3_144	Basket_3_144	PV_1_156	S1_1_144	S2_4_96	All	Integrated Total
5	Average	4.994	661	591	531	465	389	313	297	6.11E-02
	Max	5.065	662	592	532	466	390	316	300	6.16E-02
	Min	4.879	661	591	530	464	388	312	296	6.08E-02
	Location		DT_2_119	Channel_2_119	Basket_2_108	PV_2-3_119	S1_2_119	S2_4_96	All	Integrated Total

4.2 Transient Analyses

Figure 4.9 and Figure 4.10 show the peak cladding temperature and total air mass flow rate for each power tested at 800 kPa absolute helium pressure. The integrated results from the air velocity profiles were converted to calculate the total air mass flow rate in the inlet annulus. Ninety-five percent uncertainties are also presented for select data points, 1% of reading for temperature (±7 K maximum) and ±6.7E-4 kg/s for mass flow rate.

On average, the pressurized belowground configurations took a couple hours longer to reach steady state than the corresponding aboveground configurations requiring about 17 hours. Figure 4.11 shows the time required to reach steady state as function of power for the various test pressures. The time to steady state was independent of power and helium pressures except for the vacuum case. For the 100 kPa helium pressure tests there was a slight dependence on power with 13 hours required at 5.0 kW and 18 hours required at 0.5 kW. The vacuum tests were the most sensitive to power with up to 27 hours required to reach steady state in the 0.5 kW case.

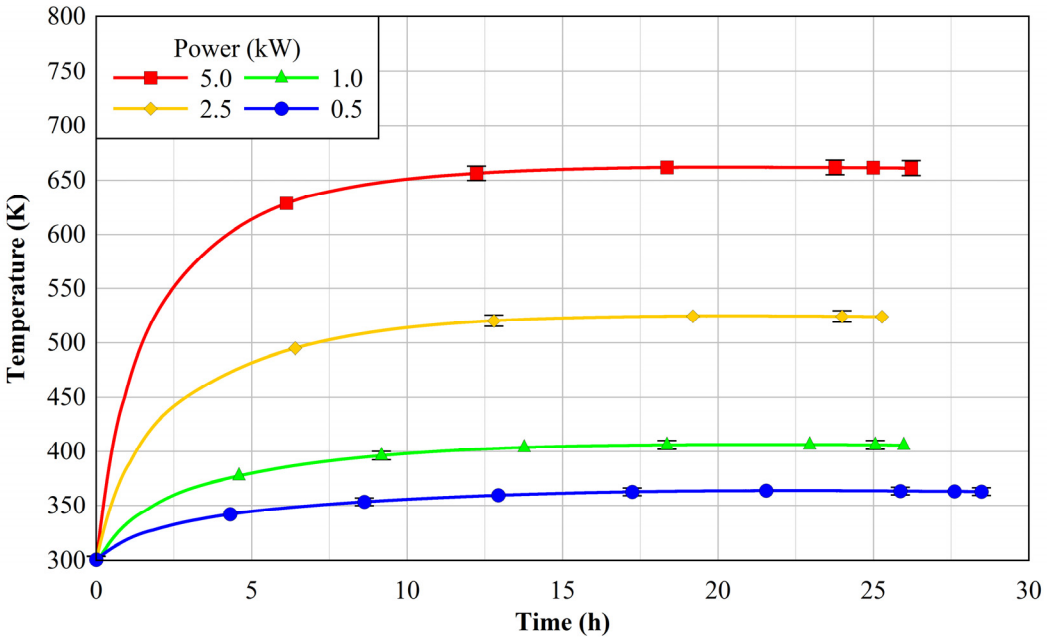

Figure 4.9 Peak cladding temperature as a function of time for tests conducted at 800 kPa helium.

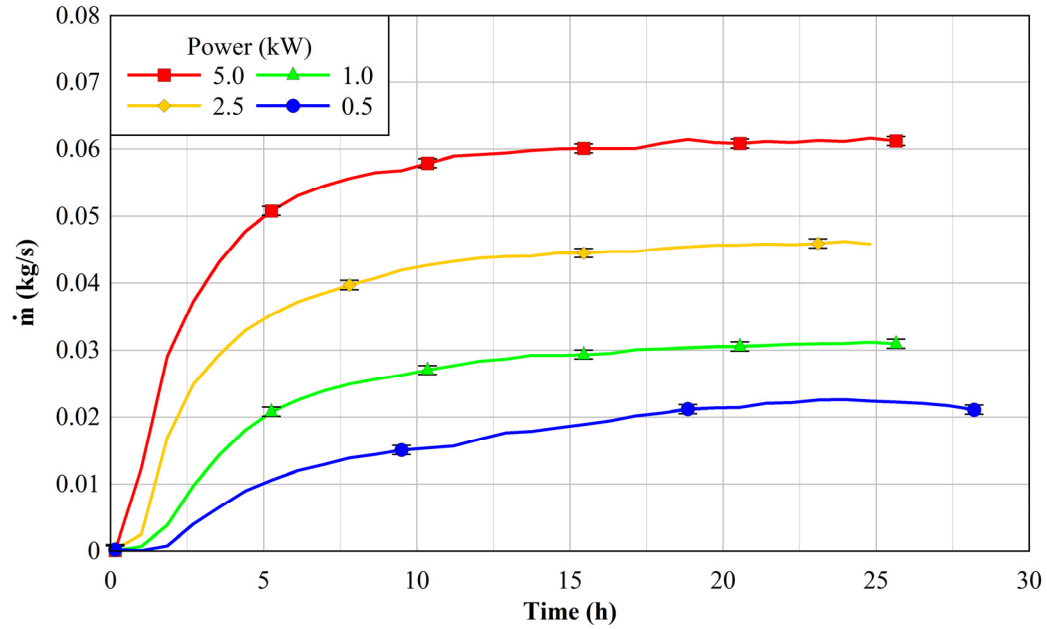

Figure 4.10 Total air mass flow rate as a function of time for tests conducted at 800 kPa helium.

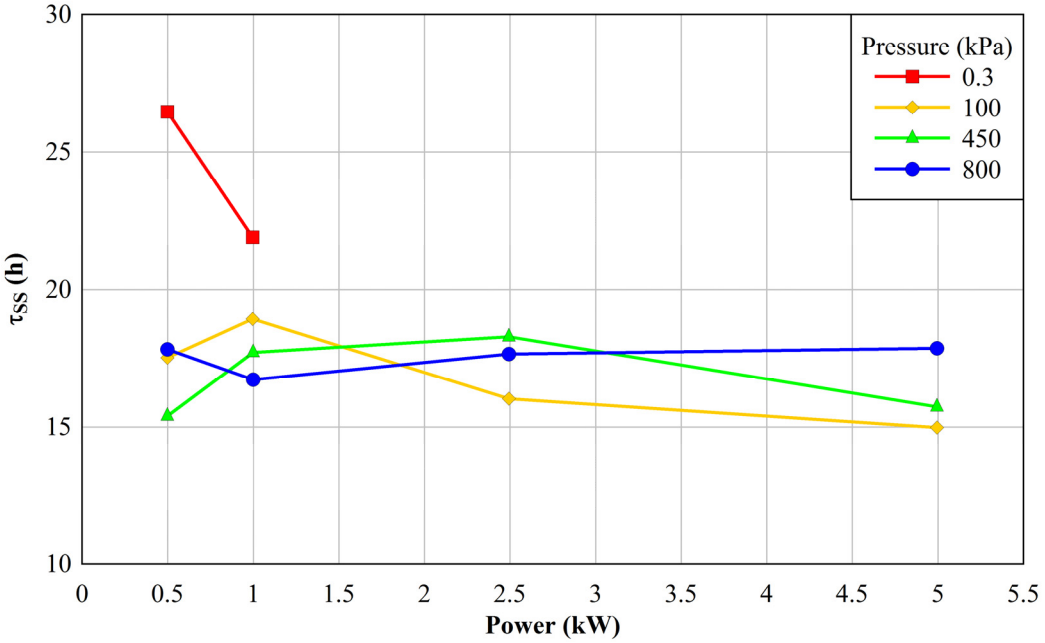

Figure 4.11 Time to reach steady state as a function of power for the various vessel pressures tested.

4.2.1 Transient Response of TC Lance and Corresponding Cladding

Figure 4.12 shows the temperature of the TC lance and adjacent cladding TCs (assuming symmetry) as a function of time at the 3.023 m elevation for the 5.0 kW and 800 kPa case. Figure 4.13 shows the temperature of the TC lance and adjacent cladding TCs at the same elevation for the 0.5 kW and 0.3 kPa case. Ninety-five percent uncertainties are also presented for select data points as 1% of reading for temperature (±7 K maximum). The transient response of the TC lance and the adjacent cladding TCs were similar. The temperature indicated by the lance TC was roughly midway between the adjacent clad TCs. The good agreement provided validation that the TC lance gives an accurate indication of nearby cladding temperatures.

Again, TC lance data for the 3.023 m (119 in.) location is presented because no anomalous behavior was evident at this elevation.

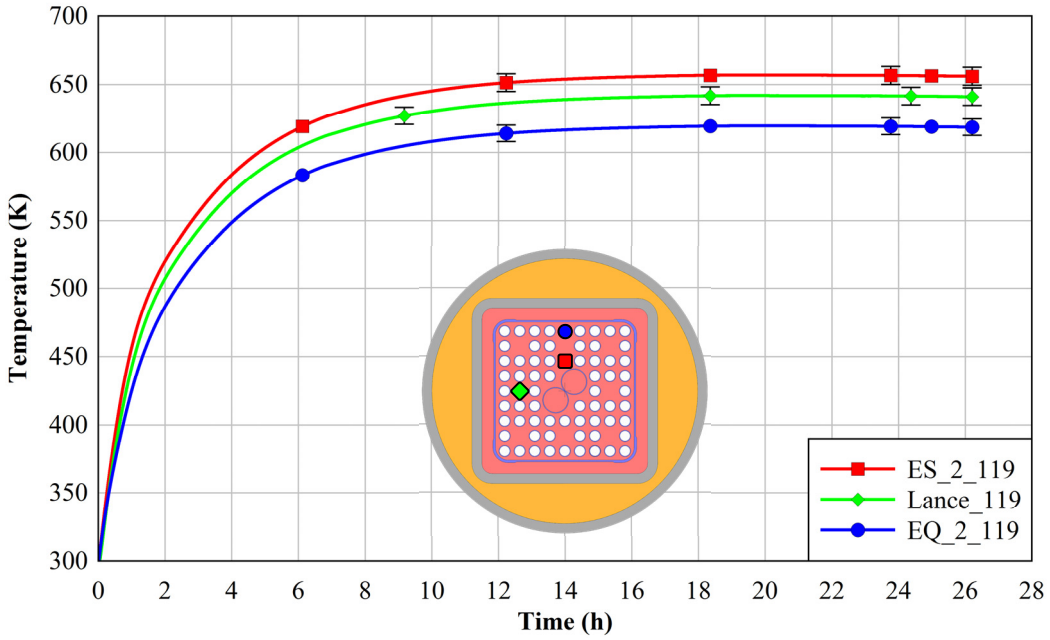

Figure 4.12 Comparison of TC lance and cladding temperatures at z = 3.023 m (119 in.) as a function of time for the test conducted at 5.0 kW and 800 kPa helium.

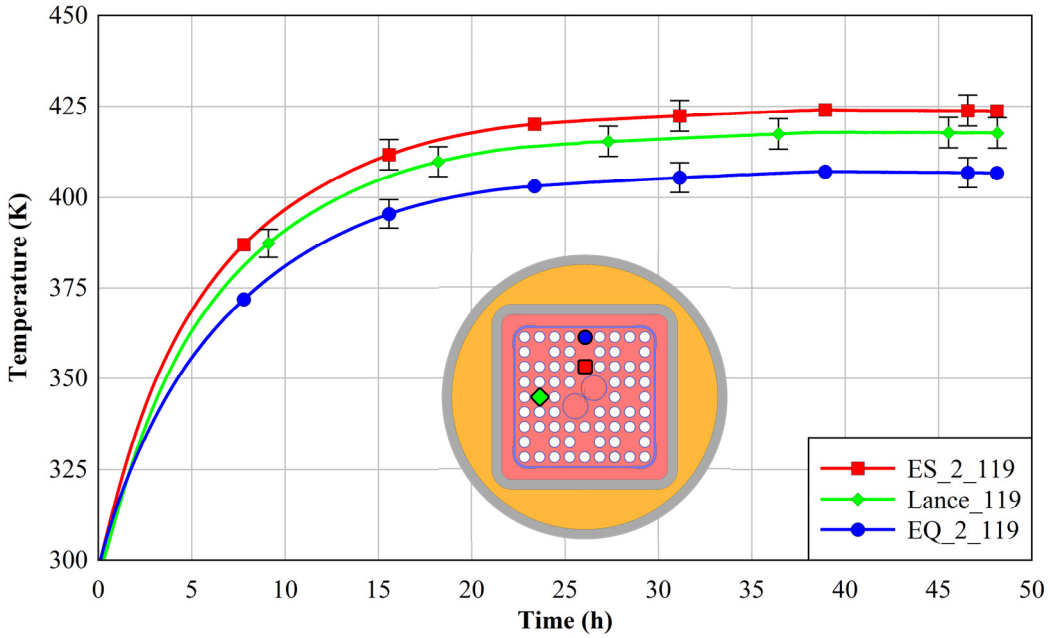

Figure 4.13 Comparison of TC lance and cladding temperatures at z = 3.023 m (119 in.) as a function of time for the test conducted at 0.5 kW and 0.3 kPa air.

4.3 Cross-Wind Analyses

Two types of cross-wind tests were conducted. In both types of test, the apparatus was first allowed to reach thermal steady-state for the given test conditions and zero cross-wind. For constant cross-wind testing, the wind machine was then started and wind speed was maintained for 12 to 18 hours. A limited

number of these extended duration tests were conducted. In all cases the rise in PCT attributed to the cross-wind was small and within the experimental error of the temperature measurement. Table 4.5 shows the temperature rise attributed to the cross-wind for each of these cases.

Table 4.5 Rise in peak cladding temperature attributed to cross-wind conditions.

Power (kW)	Pressure (kPa)	Cross-Wind (m/s)	ΔPCT (K)
1.0	100	1.3	0.2
1.0	100	2.7	0.6
1.0	100	5.3	1.7
5.0	100	1.4	1.7
5.0	100	2.7	3.7
5.0	100	5.3	5.8

At the higher wind speeds, the compressor was not able to run for these extended periods. During these tests the induced air mass flow rate obtained 95% or greater of the steady state value almost immediately. For the second type of cross-wind testing, the wind speed was changed at one hour intervals to more efficiently probe the effect of cross-wind speed on the induced air flow rate. Thermal steady-state was not reestablished. The effect of cross-wind velocity (from 0.5 to 5.4 m/s) on the induced air flow rate was measured for three powers (1.0 kW, 2.5 kW, and 5.0 kW) and three helium pressures (100 kPa, 450 kPa and 800 kPa). Figure 4.14 to Figure 4.18 present the normalized air mass flow rate as a function of cross-wind velocity for the various test cases.

As the wind speed increased from zero, the normalized air mass flow rapidly dropped to a minimum of between 0.5 to 0.6 at a cross-wind speed between 2.5 and 5.0 m/s and then slowly increased as the cross-wind speed was increased further.

Error bars are included on every other data point for enhanced clarity. As the applied power increased, the error in the normalized air mass flow rate decreased noticeably. The error did not change noticeably with helium pressure.

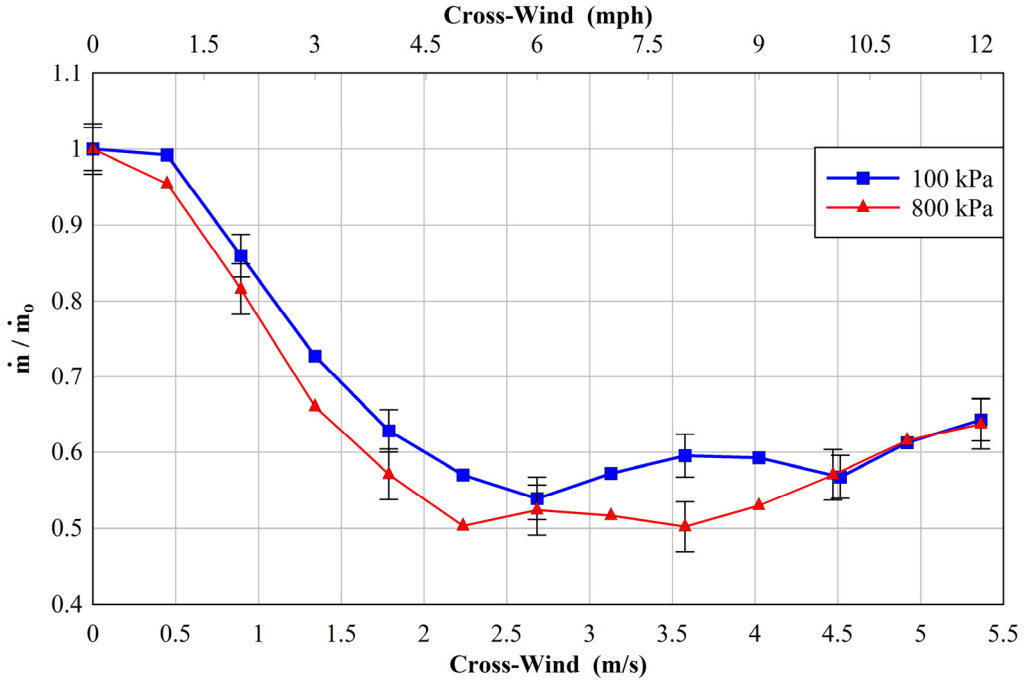

Figure 4.14 Normalized air mass flow rates as a function of cross-wind speed for 1.0 kW tests.

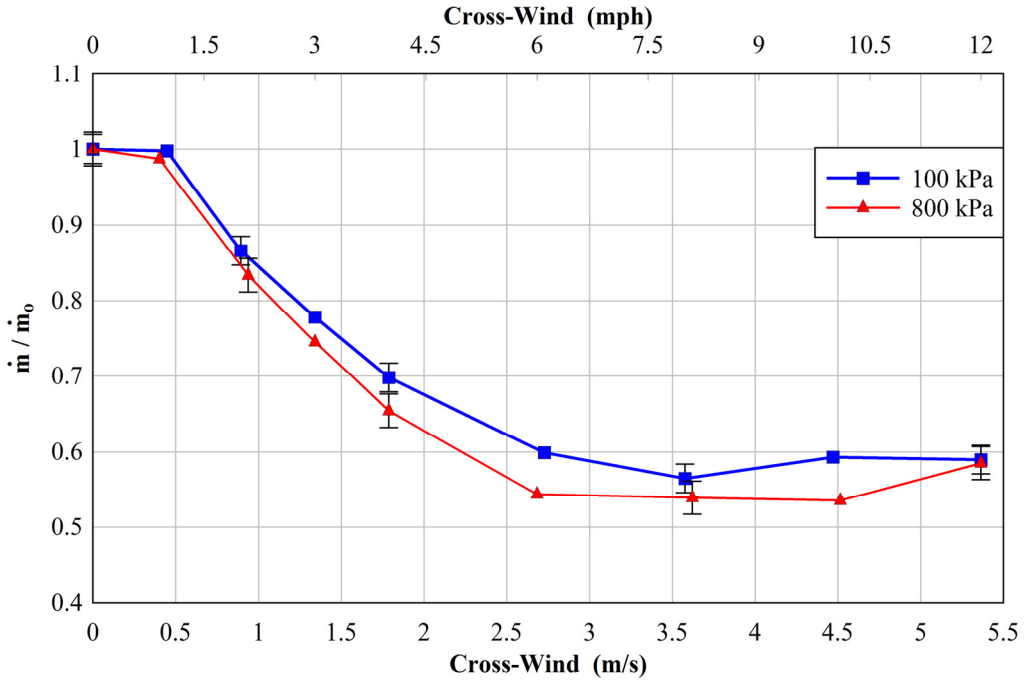

Figure 4.15 Normalized air mass flow rates as a function of cross-wind speed for 2.5 kW tests.

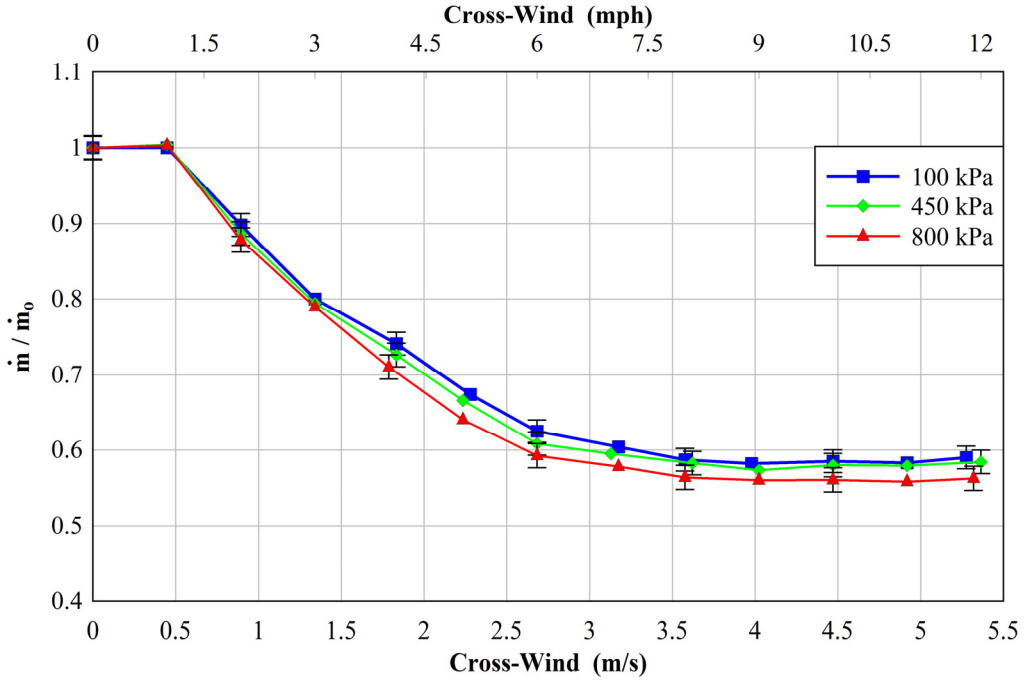

Figure 4.16 Normalized air mass flow rates as a function of cross-wind speed for 5.0 kW tests.

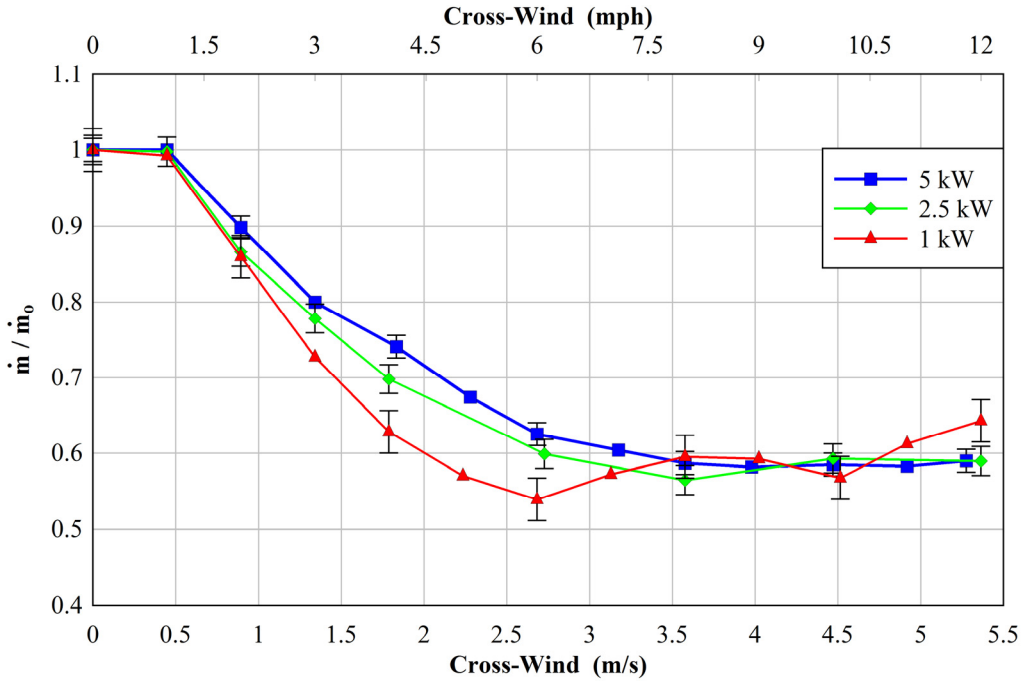

Figure 4.17 Normalized air mass flow rates as a function of cross-wind speed for 100 kPa tests.

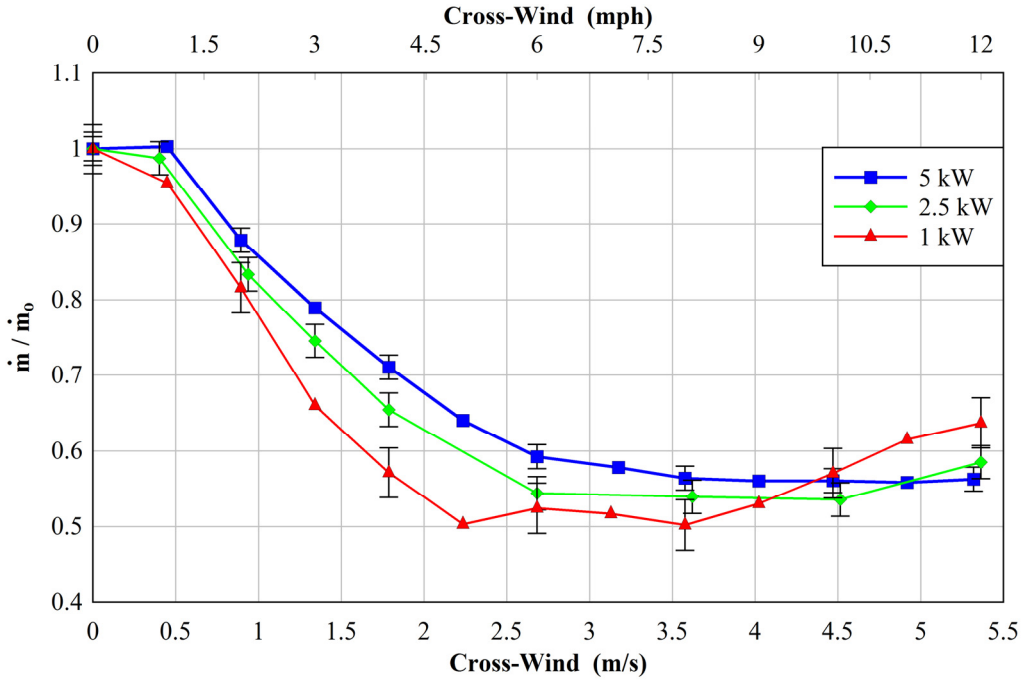

Figure 4.18 Normalized air mass flow rates as a function of cross-wind speed for 800 kPa tests.

Figure 4.20 shows velocity contours for the induced air flow in the annulus between shell 1 and shell 2 for the 5.0 kW and 100 kPa test at various cross-wind speeds. The wind was imposed on the top, or North side, of the image as indicated by the arrows. At zero cross-wind, the contours were not azimuthally symmetric with higher velocities in the Northeast and Southwest quadrants. The asymmetry was likely due to flow restrictions at the seam of the two halves of the honeycomb flow straightener located at the Northwest and Southeast quadrants. For a cross-wind speed of 1.3 m/s (3.0 mph), the

azimuthal symmetry was improved. At a cross-wind speed of 2.7 m/s (6.0 mph), the induced air flow velocity was enhanced on the windward side and nearly stagnant on the leeward side. The contrast between the induced air flow velocity on the windward and the leeward sides was diminished at 5.3 m/s (11.8 mph).

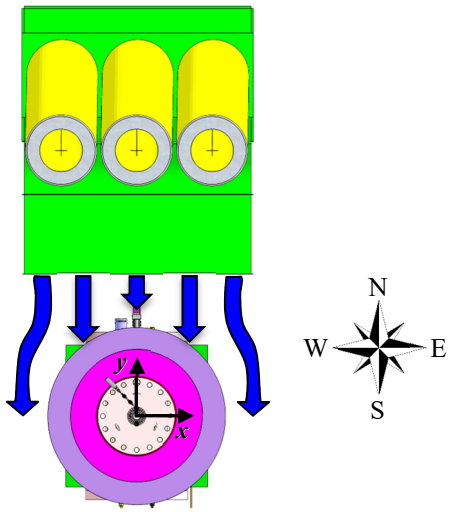

Figure 4.19 Orientation of the wind machine and test assembly.

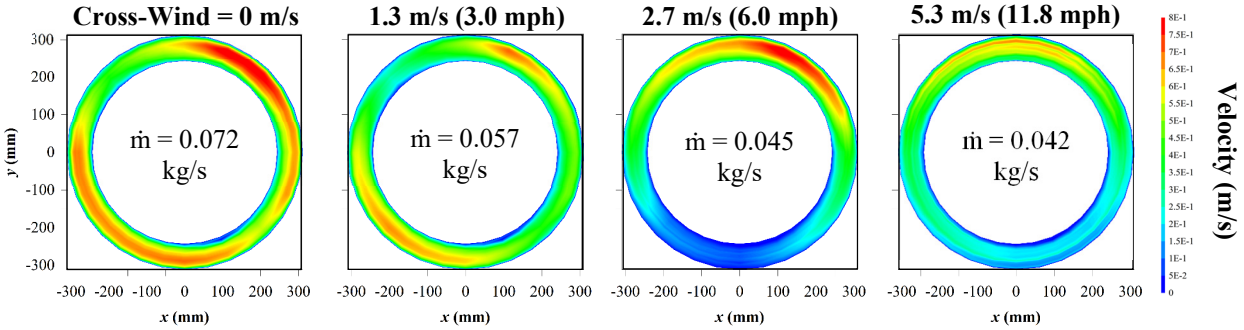

Figure 4.20 Velocity contours for 5.0 kW and 100 kPa at different cross-wind speeds.

5 SUMMARY

A test apparatus simulating a modern dry cask was successfully constructed and operated to produce first-of-a-kind, high-fidelity transient and steady-state thermal-hydraulic data sets suitable for CFD model validation. An existing electrically heated but otherwise prototypic BWR Incoloy-clad test assembly was deployed inside of a representative storage basket and cylindrical pressure vessel that represented the canister. Simulated decay power was scaled to mimic the desired range of prototypic dimensionless groups. One unique aspect of the test apparatus was the capability to pressurize the simulated canister to a wide range of pressures from subatmospheric (0.3 kPa) to the upper range of prototypic values (800 kPa). Test configurations for both vertical aboveground and belowground storage cask systems were tested. A wind machine was used to test the effect of wind speed on the peak cladding temperature and induced air mass flow rate in the belowground configuration. Cladding temperatures were measured with 0.762 mm (0.030 in.) diameter Type K thermocouples installed in direct contact with the Incoloy heater cladding. The induced air mass flow rate was determined by integrating velocity profiles measured with hot wire anemometers that impose negligible pressure drop.

A total of fourteen tests were conducted with the apparatus in the aboveground configuration. Similarly, fourteen tests were conducted with the apparatus in the belowground configuration. For these twenty-eight tests, the assembly was operated from initial, ambient conditions to thermal-hydraulic steady state for each unique combination of assembly power and vessel pressure. The power levels tested were 0.5, 1.0, 2.5, and 5.0 kW. The vessel pressures tested were vacuum (0.3 kPa), 100, 450, and 800 kPa absolute. A previous scaling analysis showed that elevated powers up to 5.0 kW were warranted to drive the induced air flow to prototypic levels. Over thirteen tests were conducted with the wind machine and the apparatus in the belowground configuration. The effect of cross-wind velocity (from 0.5 to 5.4 m/s) on the induced air mass flow rate was measured for three powers (1.0 kW, 2.5 kW, and 5.0 kW) and three helium pressures (100 kPa, 450 kPa, and 800 kPa).

The performance of the aboveground and belowground storage cask configurations were relatively similar, as expected. All steady state peak temperatures and induced air mass flow rates increased with increasing assembly power. Peak cladding temperatures decreased with increasing internal helium pressure for a given assembly power, indicating increased internal convection. In addition, the location of the PCT moved from near the top of the assembly to ~1/3 the height of the assembly for the highest (800 kPa absolute) to the lowest (0.3 kPa absolute) pressure studied, respectively. This shift in PCT location is consistent with convective heat transfer increasing with internal helium pressure. The highest average steady state PCT achieved was 715 K for 5.0 kW and 100 kPa helium pressure. This temperature was in the range of the NRC limits for allowable PCT of 673 K for normal operation and 723 K for off-normal operation. For the cross-wind test series, as the wind speed increased from zero, the normalized air mass flow rate rapidly dropped to a minimum of between 0.5 to 0.6 at a cross-wind speed between 2.5 and 5.0 m/s and then slowly increased as the cross-wind speed increased further.

Over 40 unique data sets were collected and analyzed for these efforts. The results documented in this report highlight a small, but representative, subset of the available data. This addition to the experimental database signifies a substantial addition of first-of-a-kind, high-fidelity transient and steady-state thermal-hydraulic data sets suitable for CFD model validation.

This page intentionally blank.

6 REFERENCES

ANSI, American National Standards Institute, "American National Standard for Radioactive Materials – Leakage Tests on Packages for Shipment," ANSI N14.5-2014, June 2014.

Bates, J.M., "Single PWR Spent Fuel Assembly Heat Transfer Data for Computer Code Evaluations," Pacific Northwest Laboratory, Richland, Washington, PNL-5571, January 1986.

Creer, J.M., T.E. Michener, M.A. McKinnon, J.E. Tanner, E.R. Gilbert, R.L. Goodman, "The TN-24P PWR Spent Fuel Storage Cask: Testing and Analyses", EPRI NP-5128 Proj. 2406-4, PNL-6054, Pacific Northwest Laboratory, Richland, Washington, April 1987.

Durbin, S.G., E.R. Lindgren, A. Zigh, and J. Solis, "Description of Dry Cask Simulator for Measuring Internal and External Thermal-Hydraulic Performance," SAND2016-0176C, Trans. Am. Nucl. Soc., New Orleans, LA, June 2016.

Dziadosz, D., E.V. Moore, J.M. Creer, R.A. McCann, M.A. McKinnon, J.E. Tanner, E.R. Gilbert, R.L. Goodman, D.H. Schoonen, M Jensen, and C. Mullen, "The Castor-V/21 PWR Spent-Fuel Storage Cask: Testing and Analyses," Electrical Power Research Institute, EPRI NP-4887, Project 2406-4, PNL-5917, Pacific Northwest Laboratory, Richland, Washington, November 1986.

EPRI, Electric Power Research Institute, "High Burnup Dry Storage Cask Research and Development Project: Final Test Plan," Contract No.: DE-NE-0000593, February 2014.

Irino, M., M. Oohashi, T. Irie, and T. Nishikawa, "Study on Surface Temperatures of Fuel Pins in Spent Fuel Dry Shipping/Storage Casks," IAEA-SM-286/139P, in Proceedings of Packaging and Transportation of Radioactive Materials (PATRAM '86), Volume 2, p. 585, International Atomic Energy Agency Vienna, 1987.

Lindgren, E.R. and S.G. Durbin, "Characterization of Thermal-Hydraulic and Ignition Phenomena in Prototypic, Full-Length Boiling Water Reactor Spent Fuel Pool Assemblies after a Complete Loss-of-Coolant Accident", SAND2007-2270, Sandia National Laboratories, Albuquerque, New Mexico, April 2007.

McKinnon, M.A., J.W. Doman, J.E. Tanner, R.J. Guenther, J.M. Creer and C.E. King, "BWR Spent Fuel Storage Cask Performance Test, Volume 1, Cask Handling Experience and Decay Heat, Heat Transfer, and Shielding Data," PNL-5777 Vol. 1, Pacific Northwest Laboratory, Richland Washington, February 1986.

McKinnon, M.A., J.M. Creer, C. L. Wheeler , J.E. Tanner, E.R. Gilbert, R.L. Goodman, D.P. Batala, D.A. Dziadosz, E.V. Moore, D.H. Schoonen, M.F. Jensen, and J.H. Browder, "The MC-10 PWR Spent Fuel Storage Cask: Testing and Analysis," EPRI NP-5268, PNL-6139, Pacific Northwest Laboratory, Richland, Washington, July 1987.

McKinnon, M.A., TE Michener, M.F. Jensen, G.R. Rodman, "Testing and Analyses of the TN-24P Spent Fuel Dry Storage Cask Loaded with Consolidated Fuel", EPRI NP-6191 Project 2813-16, PNL-6631, Pacific Northwest Laboratory, Richland, Washington, February 1989.

McKinnon, M.A., R.E. Dodge, R.C. Schmitt, L.E. Eslinger, & G. Dineen,, "Performance Testing and Analyses of the VSC-17 Ventilated Concrete Cask", EPRI-TR-100305, Electric Power Research Institute, Palo Alto, California, May 1992.

Nakos, J.T., "Uncertainty Analysis of Thermocouple Measurements Used in Normal and Abnormal Thermal Environment Experiments at Sandia's Radiant Heat Facility and Lurance Canyon Burn Site," SAND2004-1023, Sandia National Laboratories, Albuquerque, New Mexico, April 2004.

Zigh, A., S. Gonzalez, J. Solis, S.G. Durbin, and E.R. Lindgren, “Validation of the Computational Fluid Dynamics Method using the Aboveground Configuration of the Dry Cask Simulator,” SAND2017-6104C, Trans. Am. Nucl. Soc., San Francisco, CA, June 2017.

APPENDIX A ERROR PROPAGATION ANALYSIS

The error and uncertainty inherent to an experimental result are critical to the accurate interpretation of the data. Therefore, the uncertainties in the experimental measurements are estimated in this section. Results of this analysis are given, followed by a general description of the method used and a brief explanation of the source of each reported measurement uncertainty.

The overall standard uncertainty of an indirect measurement y, dependent on N indirect measurements x_i, is defined in Equation A.1. The standard uncertainty associated with an indirect measurement is analogous to the standard deviation of a statistical population.

$$u^2 = \sum_{i=1}^{N} \left(\frac{\partial y}{\partial x_i} u_i \right)^2 \quad \text{A.1}$$

Here, u is used to define the standard uncertainty of a measurement.

The expanded uncertainty, U, is reported in this appendix and defines the bounds that include 95% of the possible data. The expanded uncertainty is assumed to be defined as the product of the standard uncertainty and the Student's t-value. Unless otherwise stated, all uncertainty measurements are assumed to be based on a Student's t-distribution with no fewer than 30 measurements. The associated t-value for 95% intervals is 2.0 for 29 degrees of freedom. Therefore, Equation A.2 shows the definition of the expanded uncertainty as used in the following sections for a 95% confidence interval.

$$U = t_{\text{value}}\, u \quad \text{A.2}$$

Table A.1 summarized the expanded uncertainty determined below for each measurement used in this report.

Table A.1 Summary of the expanded uncertainty determined for each measurement.

Measurement, x	Units	Expanded Uncertainty, U_x
Peak clad temperature	K	7.0E+00
Ambient temperature	K	3.0E+00
Ambient pressure	kPa, abs	1.1E-01
Helium pressure	kPa, abs	1.0E+00
Vacuum	kPa, abs	3.0E-01
Voltage	V	3.8E-01
Current	A	3.8E-01
Power	kW	7.5E-02
Forced air mass flow rate	kg/s	5.9E-04
Induced air mass flow rate (aboveground)	kg/s	1.5E-03
Induced air mass flow rate (belowground)	kg/s	6.8E-04
Induced air mass flow rate (cross-wind)	kg/s	7.5E-04
Normalized air mass flow rate, $\dot{m}/\dot{m}_o$	-	3.4E-02
Cross-wind speed	m/s	4.9E-02

A.1 Temperature Measurements

A.1.1 Uncertainty in Clad Temperature Measurement

Clad temperature was measured with a standard k-type TC. The expanded uncertainty for this type of TC is U_T = 1% of the reading in Kelvin [Nakos, 2004]. The maximum peak clad temperature reading was 716 K for the aboveground 5.0 kW 100 kPa helium test. The maximum expanded uncertainty for the cladding temperature is U_{PCT} = ±7.0 K.

A.1.2 Uncertainty in Ambient Air Temperature

The air temperature was measured with a standard k-type TC. The expanded uncertainty for this type of TC is U_T = 1% of the reading in Kelvin [Nakos, 2004]. The maximum ambient temperature reading was 305 K for the aboveground 5.0 kW 100 kPa helium test. The maximum expanded uncertainty for the ambient temperature is $U_{T\text{-}amb}$ = ±3.0 K.

A.2 Pressure Measurements

A.2.1 Uncertainty in Ambient Air Pressure

The air pressure was measured with a Setra Systems barometer (Model 276). The uncertainty of the ambient air pressure was taken from the manufacturer's calibration sheet, which indicated an expanded uncertainty in the instrument of ±0.1% of full scale (110 kPa). Therefore, the expanded uncertainty in the pressure reading is $U_{P\text{-}atm}$ = ±0.11 kPa.

A.2.2 Uncertainty in Helium Vessel Pressure

The helium pressure was measured using an Omega model PX409-500A5V-XL 0 to 3447 kPa (500 psia) pressure transducer. The resolution of the transducer allowed the pressure control system described in Section 2.3.2.1 to maintain the pressure constant to ±0.3 kPa (0.044 psi). However, with the "–XL" accuracy identifier the linearity deviates ±0.03% from the best straight line, which at full scale is ±1.0 kPa (±0.15 psi). Therefore, the expanded uncertainty is $U_{P\text{-}He}$ = ±1.0 kPa.

A.2.3 Uncertainty in Air Vessel Pressure

The residual air pressure was measured using an Omega model PXM409-001BV10V 0 to 100 kPa absolute (0 to 14.5 psia) pressure transducer. The linearity deviates ±0.08% from the best straight line, which at full scale is ±0.08 kPa (±0.012 psi). However, the span and zero shift for temperature compensation are each ±0.5%, which for full scale is ±0.5 kPa (±0.073 psi). The geometric mean of these three expanded uncertainties is ±0.3%, or ±0.3 kPa (±0.044 psi). This value of 0.3 kPa absolute was assumed to be the smallest determinable pressure under vacuum conditions. Therefore, all vacuum tests are reported as 0.3 kPa even though the gage typically read less than this value.

A.3 Uncertainty in Electrical Measurements

The voltage, current and power supplied to the internal spent fuel assembly heater rods were measured by Ohio Semitronics, Inc. instrumentation. The voltage was monitored by a model AVTR-001D voltmeter with an expanded uncertainty of U_{Volt} = ±0.38 V. The current was monitored by a model ACTR-005DY06 current meter with an expanded uncertainty of U_{Amp} = ±0.38 A. The power was monitored with a model PC5-001DY230 Watt meter with an expanded uncertainty of U_{Watt} = ±0.075 kW.

A.4 Flow Measurements

The methodology for determining the induced air flow in the aboveground and belowground configurations was different. As described in detail in Section 2.4.2 for the aboveground configuration, correlation of the hot wires in the inlet ducts was performed by imposing a known mass flow rate of air through the ducting with the hot wires held in a fixed location and then implementing a small correction based on velocity profile measurement and integrating to a total mass flow for the buoyancy driven flows. For the belowground configuration described in detail in Section 2.4.3, forced flow correlation in the annulus between Shell 1 and Shell 2 was not possible so the mass flow was determined by integrating eight velocity profiles (twelve for cases with wind).

A.4.1 Aboveground Configuration

A.4.1.1 Uncertainty in Air Mass Flow Controllers

The air flow was controlled using an OMEGA FMA-2623A 0 to 3000 slpm (or 5.92E-2 kg/s at the standard conditions of 25 °C and 101.4 kPa) mass flow controller. The maximum expanded uncertainty is ±1.0% of full scale at full flow or ±5.9E-4 kg/s.

A.4.1.2 Uncertainty in Hot Wire Anemometer Measurements

The parameter values needed to determine the induced air flow from the hot wire measurements are listed in Tables A.2 and A.3 along with the parameter's expanded uncertainty, influence coefficient and contribution to the error. V_{TSI} is the voltage output of the TSI Model 8455 hot wire anemometer. The expanded uncertainty is given by the manufacturer as ±0.025 m/s for the ambient temperatures encountered. The full-scale voltage output is 10 V so the expanded error in the voltage output is ±0.25 V. Standard conditions for the TSI hotwire are 21.1 °C and 101.4 kPa. The primary calibration of the hot wires was performed by metering a measured flow of air with the hot wire centered in the duct at the position indicated in Figure 2.19. Figure 2.20 shows the forced flow calibration curve for the TSI Model 8455 hot wire located in a fixed position in the center of an inlet duct as shown in Figure 2.21 along with the equation for the best linear through the data. The constant linear fit coefficient, $a_{TSI,0}$ is -8.0E-04 kg/s with an expanded error of 9.0E-05 kg/s based on the fit of the linear correlation. The first order linear fit coefficient, $a_{TSI,1}$ is 2.8E-03 kg/s/V with an expanded uncertainty of 1.8E-05 kg/s/V. An additional correlation was needed to relate the naturally induced flow to the metered forced flow. After each powered test during steady state, the hot wire was traversed across the narrow dimension of the duct as shown in Figure 2.21 to generate a velocity profile. The profile was integrated across the area of the duct to calculate the total naturally induce flow. Figure 2.23 shows the correlation between the more direct measurements of the naturally induced flow based on the velocity profile measurement made only at the end of the test and the less direct measurement based on the forced flow correlation with the hot wire in the fixed location maintained throughout the ~24 hour transient to steady-state. The correlation coefficient, C_{corr}, is 0.9344 with an expanded uncertainty of 1.3E-2 based on a *t*-value of 2.2 for the 12 data points used to define the correlation. The mass flow in each duct is determined with an expanded error of ±7.4E-04 kg/s. The error in the hot wire air velocity measurement contributed 80% of the error followed by the natural flow to forced flow correlation, which contributed 15% of the error.

Table A.2 Parameters values and uncertainty analysis for a single hotwire measurement in the aboveground configuration.

Measurement, x_i	Units	Value	Expanded uncertainty, U_i	Influence coefficient ($U_i \cdot [(\partial \dot{m}/\partial x_i)/\dot{m}]$)	Contribution
V_{TSI}	V	8.0E+00	2.5E-01	3.2E-02	0.80
$a_{TSI,0}$	kg/s	-8.0E-04	9.0E-05	4.1E-03	0.01
$a_{TSI,1}$	(kg/s)/V	2.8E-03	1.8E-05	6.7E-03	0.03
C_{corr}	--	9.3E-01	1.3E-02	1.4E-02	0.15
$\dot{m}$	kg/s	2.0E-02	7.4E-04	3.6E-02	1.00

Table A.3 outlines the calculation of the total mass flow from the four ducts. The expanded error in the total air mass flow of U_m = ±1.5e-03 kg/s.

Table A.3 Uncertainty analysis for combining multiple hotwire measurements into a total induced flow rate in the aboveground configuration.

Measurement, x_i	Units	Value	Expanded uncertainty, U_i	Influence coefficient ($U_i \cdot [(\partial \dot{m}/\partial x_i)/\dot{m}]$)	Contribution
$\dot{m}_1$	kg/s	2.0E-02	7.4E-04	9.0E-03	0.25
$\dot{m}_2$	kg/s	2.0E-02	7.4E-04	9.0E-03	0.25
$\dot{m}_3$	kg/s	2.0E-02	7.4E-04	9.0E-03	0.25
$\dot{m}_4$	kg/s	2.0E-02	7.4E-04	9.0E-03	0.25
$\dot{m}$	kg/s	8.2E-02	1.5E-03	1.8E-02	1.00

A.4.2 Belowground Configuration (Annular Gap)

The details for the determination of the total induced air mass flow rate in the belowground configuration are given in Section 2.4.3. In the belowground configuration, forced flow correlation in the annulus between Shell 1 and Shell 2 was not possible so the mass flow was determined by integrating eight velocity profiles. Hotwire air velocity measurements were made at fourteen equidistant locations across the annular gap. The temperature of the air flow in the annular gap was up to 41°C, which raises the expanded error of the measurement to ±0.051 m/s. The integration process involves calculation of an associated flow area for each velocity measurement. Table A.4 presents the pertinent inputs for the calculation along with the expanded error, influence coefficient and error contribution. The expanded error in the flow area for each air velocity measurement is ±2.4E-05 m^2. Table A.5 presents a representative integration calculation to determine the mass flow and expanded error for one of the eight hotwires.

Table A.4 Representative calculation to estimate the expanded error of flow area determination.

Measurement, x_i	Units	Value	Expanded uncertainty, U_i	Influence coefficient ($U_i \cdot [(\partial \Delta A/\partial x_i)/\Delta A]$)	Contribution
r	m	3.1E-01	6.4E-03	2.0E-02	1.00
Δr	m	4.8E-03	5.0E-06	5.2E-04	0.00
$\theta/2\pi$	--	1.3E-01	--	--	--
ΔA	m^2	1.2E-03	2.4E-05	2.0E-02	1.00

Table A.5 Representative integration calculation to determine the mass flow and expanded error for one of the eight hotwires.

Measurement, x_i	Units	Value	Expanded uncertainty, U_i	Influence coefficient ($U_i \cdot [(\partial \dot{m}_i/\partial x_i)/\dot{m}_i]$)	Contribution
$v_{i,1}$	m/s	3.1E-01	5.1E-02	6.9E-03	0.06
$\Delta A_{i,1}$	m^2	7.8E-03	2.4E-05	1.3E-04	0.00
$v_{i,2}$	m/s	4.8E-01	5.1E-02	8.1E-03	0.09
$\Delta A_{i,2}$	m^2	9.1E-03	2.4E-05	2.0E-04	0.00
$v_{i,3}$	m/s	6.1E-01	5.1E-02	7.9E-03	0.09
$\Delta A_{i,3}$	m^2	9.0E-03	2.4E-05	2.5E-04	0.00
$v_{i,4}$	m/s	6.0E-01	5.1E-02	7.8E-03	0.08
$\Delta A_{i,4}$	m^2	8.9E-03	2.4E-05	2.5E-04	0.00
$v_{i,5}$	m/s	6.4E-01	5.1E-02	7.7E-03	0.08
$\Delta A_{i,5}$	m^2	8.7E-03	2.4E-05	2.6E-04	0.00
$v_{i,6}$	m/s	6.1E-01	5.1E-02	7.5E-03	0.08
$\Delta A_{i,6}$	m^2	8.6E-03	2.4E-05	2.5E-04	0.00
$v_{i,7}$	m/s	6.0E-01	5.1E-02	7.4E-03	0.08
$\Delta A_{i,7}$	m^2	8.4E-03	2.4E-05	2.5E-04	0.00
$v_{i,8}$	m/s	5.7E-01	5.1E-02	7.3E-03	0.07
$\Delta A_{i,8}$	m^2	8.3E-03	2.4E-05	2.4E-04	0.00
$v_{i,9}$	m/s	5.5E-01	5.1E-02	7.2E-03	0.07
$\Delta A_{i,9}$	m^2	8.1E-03	2.4E-05	2.3E-04	0.00
$v_{i,10}$	m/s	5.2E-01	5.1E-02	7.0E-03	0.07
$\Delta A_{i,10}$	m^2	8.0E-03	2.4E-05	2.1E-04	0.00
$v_{i,11}$	m/s	4.8E-01	5.1E-02	6.9E-03	0.07
$\Delta A_{i,11}$	m^2	7.8E-03	2.4E-05	2.0E-04	0.00
$v_{i,12}$	m/s	4.0E-01	5.1E-02	6.8E-03	0.06
$\Delta A_{i,12}$	m^2	7.7E-03	2.4E-05	1.6E-04	0.00
$v_{i,13}$	m/s	3.6E-01	5.1E-02	6.7E-03	0.06
$\Delta A_{i,13}$	m^2	7.6E-03	2.4E-05	1.5E-04	0.00
$v_{i,14}$	m/s	2.5E-01	5.1E-02	5.4E-03	0.04
$\Delta A_{i,14}$	m^2	6.1E-03	2.4E-05	1.0E-04	0.00
ρ_{Ref}	kg/m^3	1.2E+00	--	--	--
$\dot{m}_i$	kg/s	8.7E-03	2.3E-04	2.7E-02	1.00

Table A.6 presents the calculation of the total air mass flow and expanded error based on all eight hotwires. The expanded error for the total air mass flow determination in the belowground configuration is $U_m = \pm$6.8E-04 kg/s.

Table A.6 Calculation of the total mass flow and expanded error from the eight hotwires used in the belowground configuration.

Measurement, x_i	Units	Value	Expanded uncertainty, U_i	Influence coefficient ($U_i \cdot [(\partial \dot{m}/\partial x_i)/\dot{m}]$)	Contribution
$\dot{m}_1$	kg/s	8.7E-03	2.3E-04	3.3E-03	0.12
$\dot{m}_2$	kg/s	1.1E-02	3.1E-04	4.4E-03	0.21
$\dot{m}_3$	kg/s	8.8E-03	2.4E-04	3.4E-03	0.12
$\dot{m}_4$	kg/s	7.5E-03	2.0E-04	2.9E-03	0.09
$\dot{m}_5$	kg/s	9.6E-03	2.6E-04	3.7E-03	0.14
$\dot{m}_6$	kg/s	9.6E-03	2.6E-04	3.7E-03	0.14
$\dot{m}_7$	kg/s	9.0E-03	2.4E-04	3.5E-03	0.13
$\dot{m}_8$	kg/s	5.5E-03	1.5E-04	2.1E-03	0.05
$\dot{m}$	kg/s	7.0E-02	6.8E-04	9.7E-03	1.00

A.4.3 Cross-Wind Configuration

The determination of the total mass flow of air for the belowground configuration with cross-wind was similar to the belowground configuration except twelve hot wires were used as described in detail in Section 2.5. Tables A.4 and A.5 are applicable. Table A.7 shows the calculation using twelve hotwires. Using the twelve hotwires the expanded error for the total air mass flow determination in the belowground configuration is U_m = ±7.5E-04 kg/s.

Table A.7 Calculation of the total mass flow and expanded error from the twelve hotwires used in the cross-wind configuration.

Measurement, x_i	Units	Value	Expanded uncertainty, U_i	Influence coefficient ($U_i \cdot [(\partial \dot{m}/\partial x_i)/\dot{m}]$)	Contribution
$\dot{m}_1$	kg/s	6.8E-03	2.3E-04	3.3E-03	0.10
$\dot{m}_2$	kg/s	5.6E-03	1.9E-04	2.7E-03	0.07
$\dot{m}_3$	kg/s	5.8E-03	2.0E-04	2.8E-03	0.07
$\dot{m}_4$	kg/s	4.7E-03	1.6E-04	2.3E-03	0.05
$\dot{m}_5$	kg/s	4.4E-03	1.5E-04	2.1E-03	0.04
$\dot{m}_6$	kg/s	4.5E-03	1.6E-04	2.2E-03	0.04
$\dot{m}_7$	kg/s	3.8E-03	1.3E-04	1.8E-03	0.03
$\dot{m}_8$	kg/s	4.2E-03	1.4E-04	2.0E-03	0.04
$\dot{m}_9$	kg/s	7.2E-03	2.5E-04	3.5E-03	0.11
$\dot{m}_{10}$	kg/s	9.8E-03	3.4E-04	4.7E-03	0.20
$\dot{m}_{11}$	kg/s	9.3E-03	3.2E-04	4.5E-03	0.19
$\dot{m}_{12}$	kg/s	5.6E-03	1.9E-04	2.7E-03	0.07
$\dot{m}$	kg/s	7.2E-02	7.5E-04	1.0E-02	1.00

The effect of cross-wind was evaluated using a normalized flow variable, $\dot{m}/\dot{m}_o$, defined as the air mass flow with wind divided by the mass flow without wind under the same conditions. The expanded uncertainties for $\dot{m}/\dot{m}_o$ are presented in Table A.8 for various test conditions.

Table A.8 Expanded uncertainties in normalized mass flow, $\dot{m}/\dot{m}_o$, for various conditions tested.

Conditions	Expanded uncertainty, U_i
5 kW, 100 kPa	1.50E-02
5 kW, 800 kPa	1.70E-02
2.5 kW, 100 kPa	2.00E-02
2.5 kW, 800 kPa	2.30E-02
1.0 kW, 100 kPa	2.90E-02
1.0 kW, 800 kPa	3.40E-02

A.4.3.1 Cross-Wind Velocity

The area weighted average cross-wind velocity was determined using the same type TSI Model 8455 hot wire anemometers fixed at three locations shown in Figure 2.29. As discussed in Section 2.5, the average of the three fixed hotwires was correlated with the area weighted average of 45 regularly spaced points. The standard error about the best straight line was ±0.0113 m/s. Using the *t*-value of 4.3 for the three data-point correlation, the expanded error for the area weighted cross-wind velocity is U_{wind} = ±0.049 m/s.

APPENDIX B THERMOCOUPLE LANCE ANOMALY

B.1 Background

The results generated in this test series supplement thermal data collected as part of the High Burnup Dry Storage Cask Project [EPRI, 2014]. A shortened version of the thermal lance design deployed in the Cask Project was installed in the DCS. Installation of this lance in the DCS assembly allows the measurement of temperatures inside of a "guide tube" structure for comparison with a temperature measured directly on the fuel cladding. The TC spacing on the lance matched the elevation of the TCs in the upper portion of the A1 and A2 axial arrays and the radial array at 3.023 m (119 in.) and 3.658 m (144 in.) elevations.

The lance was made by the same fabricator using the same process and materials as the TC lances that will be used in the full scale High Burnup Dry Storage Cask Research and Development Project [EPRI, 2014]. The TC spacing was designed to correspond with TCs installed on the test assembly heater rod cladding to provide a direct comparison between the two measurements. Direct comparisons between TC lance and corresponding clad temperature measurements are expected to aid in the interpretation of the TC lance data generated during the High Burnup Cask Project.

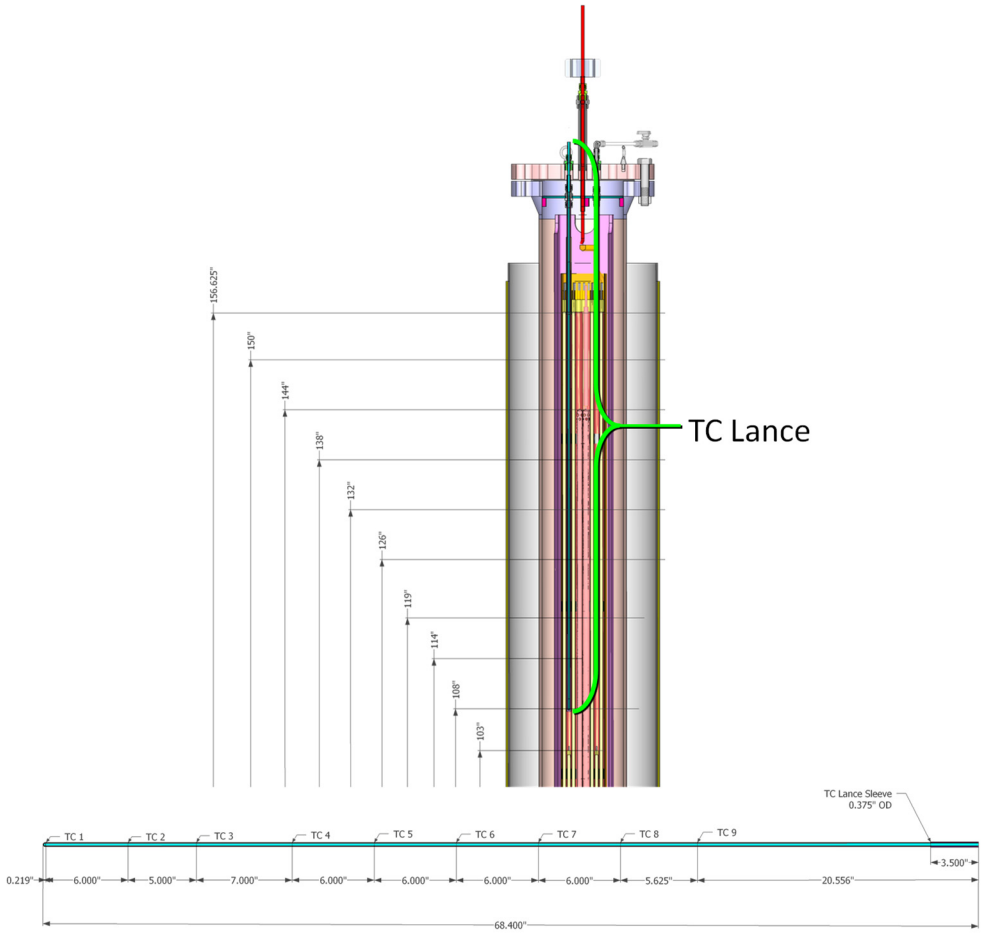

Figure B.1 TC lance installation and TC spacing details.

B.2 Anomalous Transient Behavior

Some of the lance TCs exhibited unusual behavior under certain conditions. Figure B.2 to Figure.16 shows the lance data collected between 23 June 2016 and 22 August 2016. When it occurs, the anomalous behavior is characterized by a rapid increase in temperature followed by a brief to prolong leveling which is sometimes followed by a second rise and leveling in temperature. The lower three TC locations at 108", 114" and 119" do not seem to be effected. None of the lance TCs are effected in the tests where all the lance TC temperatures remained below 373 K (100°C). When the lower lance TCs reach 373 K (100°C) the upper lance TCs often start to show an increased heating rate.

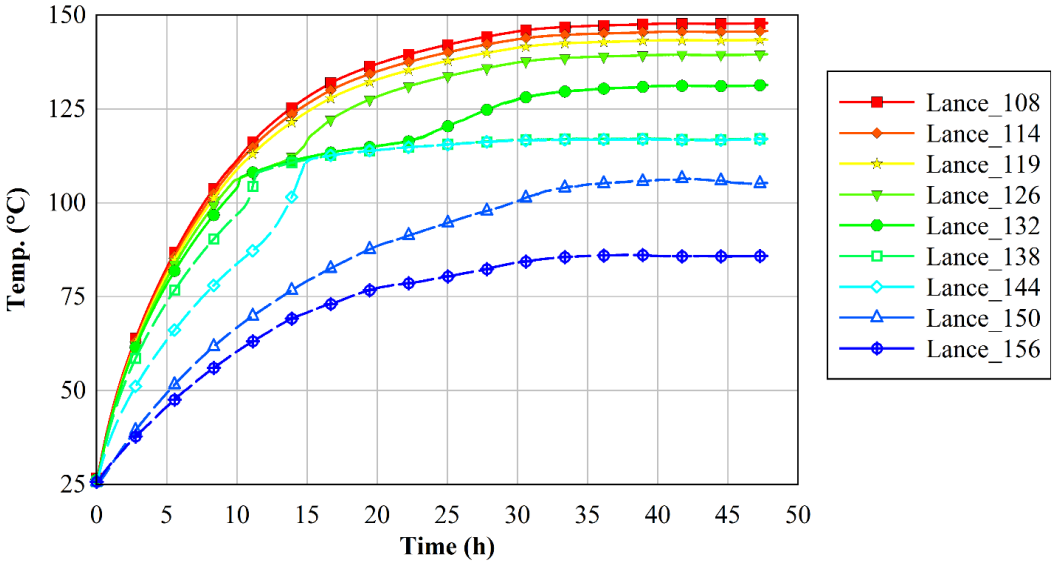

Figure B.2 TC lance data for the 0.5 kW test at 3 kPa on 8/3/2016.

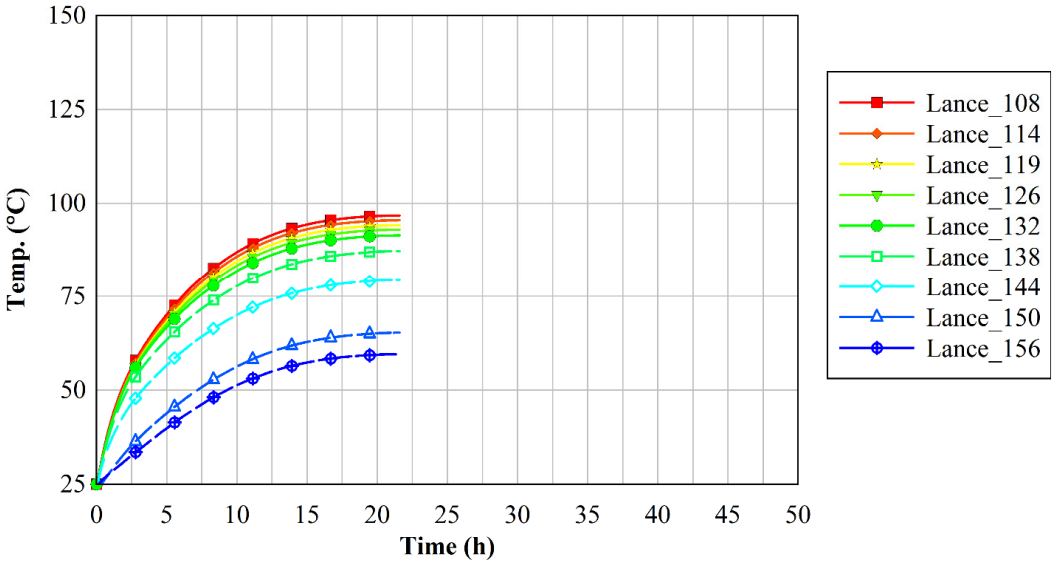

Figure B.3 TC lance data for the 0.5 kW test at 100 kPa on 7/18/2016.

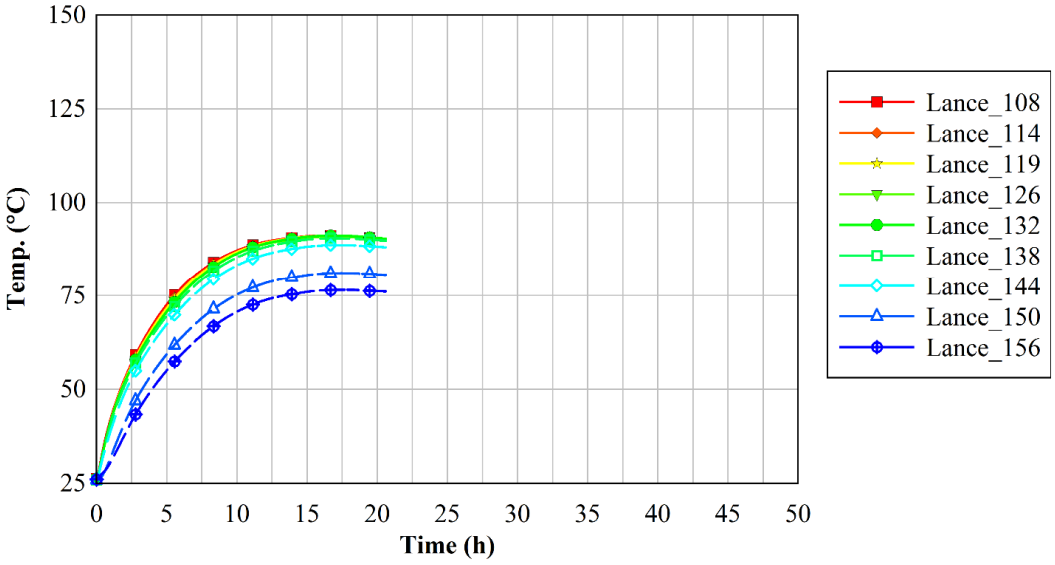

Figure B.4 TC lance data for the 0.5 kW test at 450 kPa on 7/11/2016.

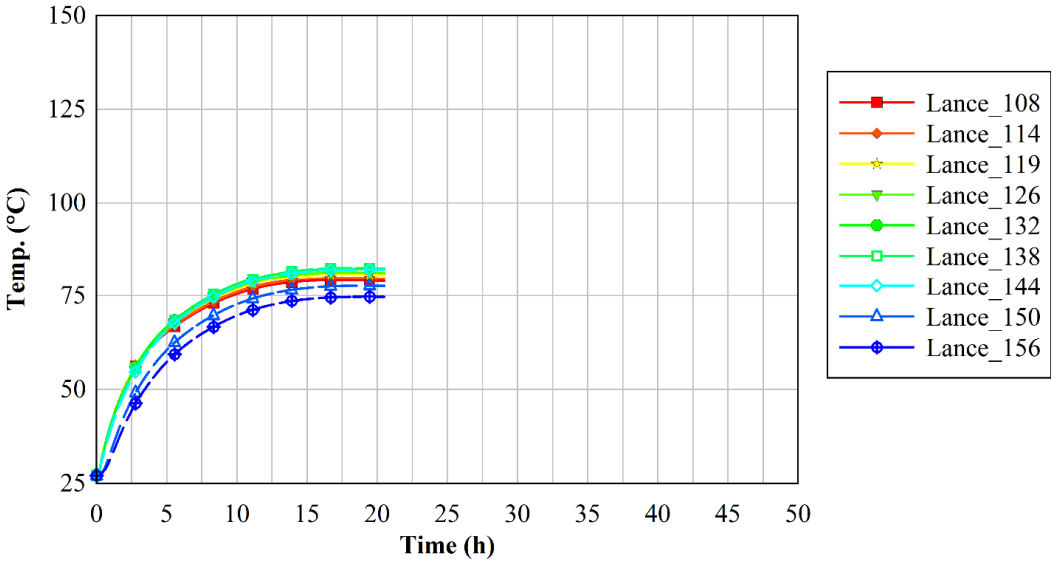

Figure B.5 TC lance data for the 0.5 kW test at 800 kPa on 6/29/2016.

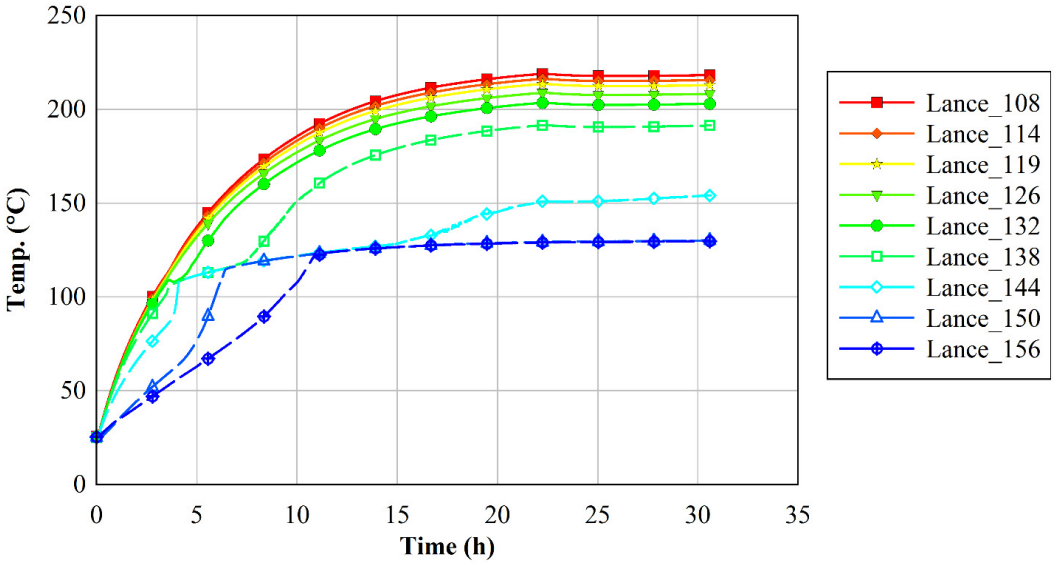

Figure B.6 TC lance data for the 1.0 kW test at 3 kPa on 8/8/2016.

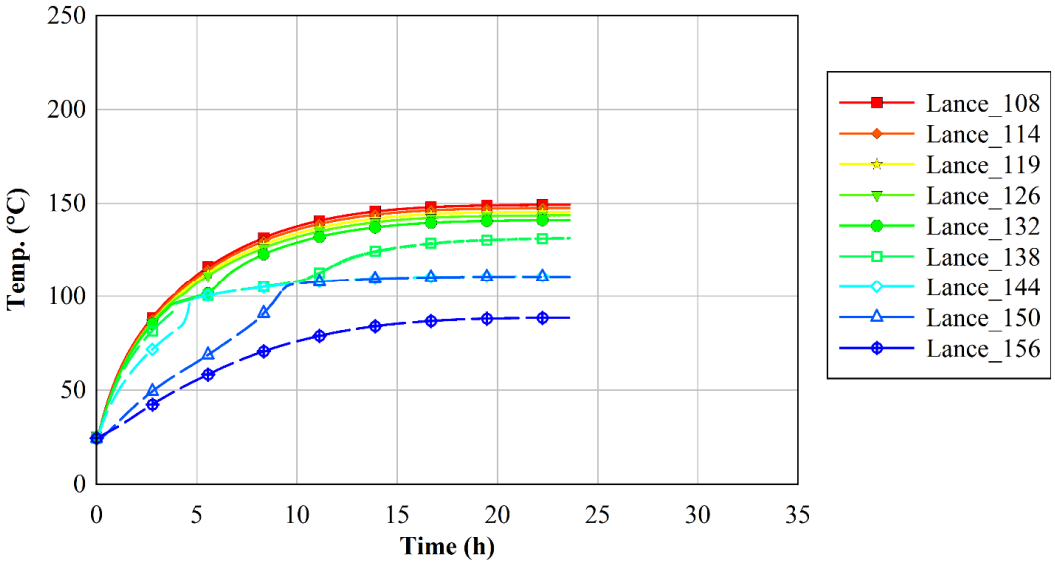

Figure B.7 TC lance data for the 1.0 kW test at 100 kPa on 7/25/2016.

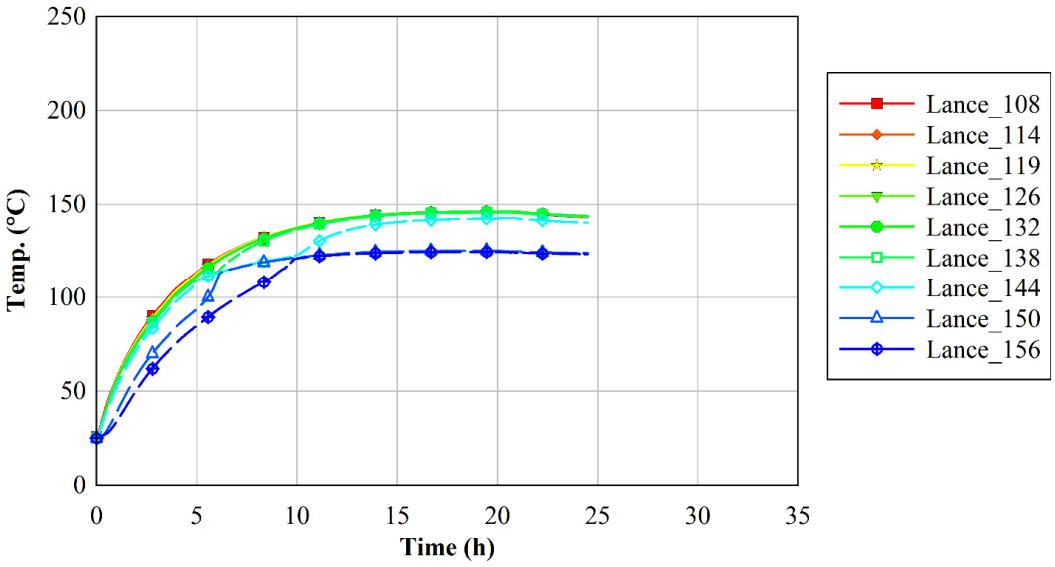

Figure B.8 TC lance data for the 1.0 kW test at 450 kPa on 7/21/2016.

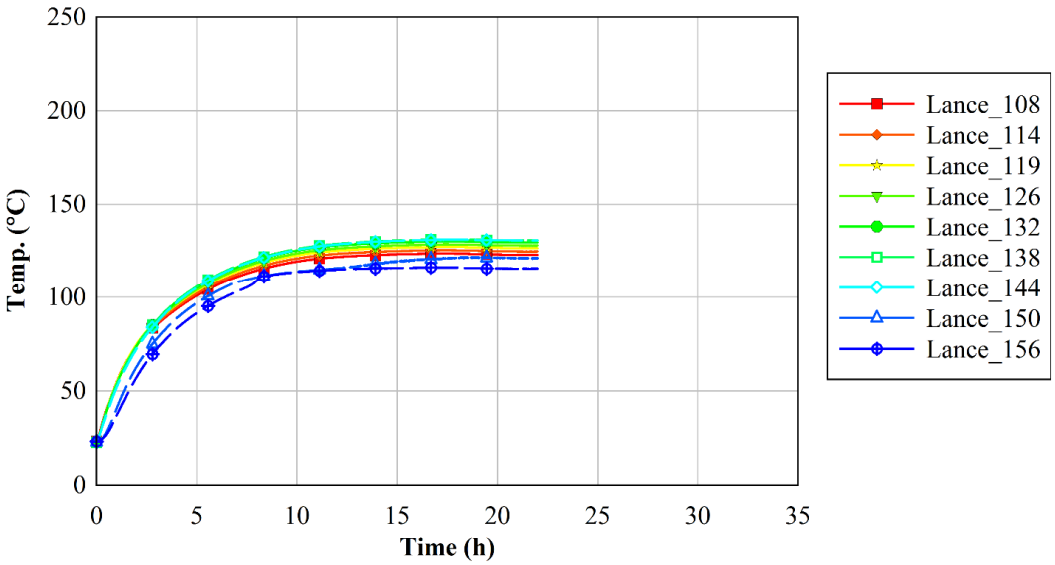

Figure B.9 TC lance data for the 1.0 kW test at 800 kPa on 7/7/2016.

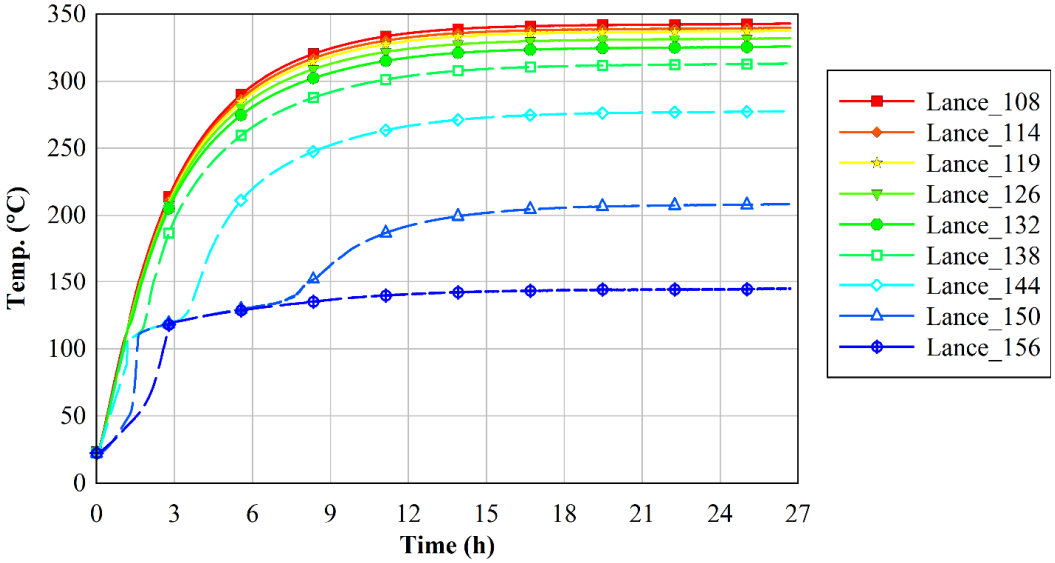

Figure B.10 TC lance data for the 2.5 kW test at 3 kPa on 8/22/2016.

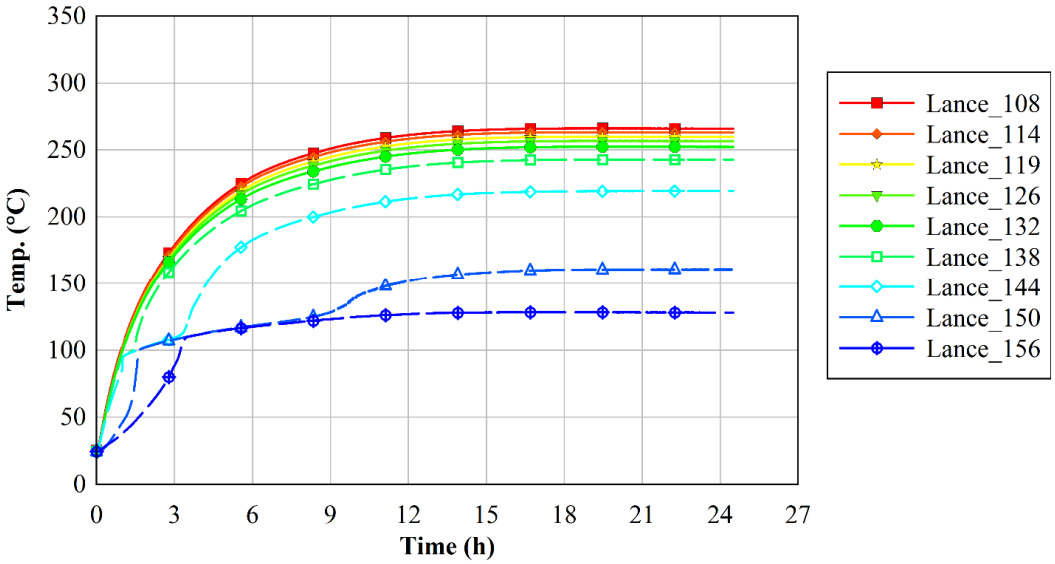

Figure B.11 TC lance data for the 2.5 kW test at 100 kPa on 7/27/2016.

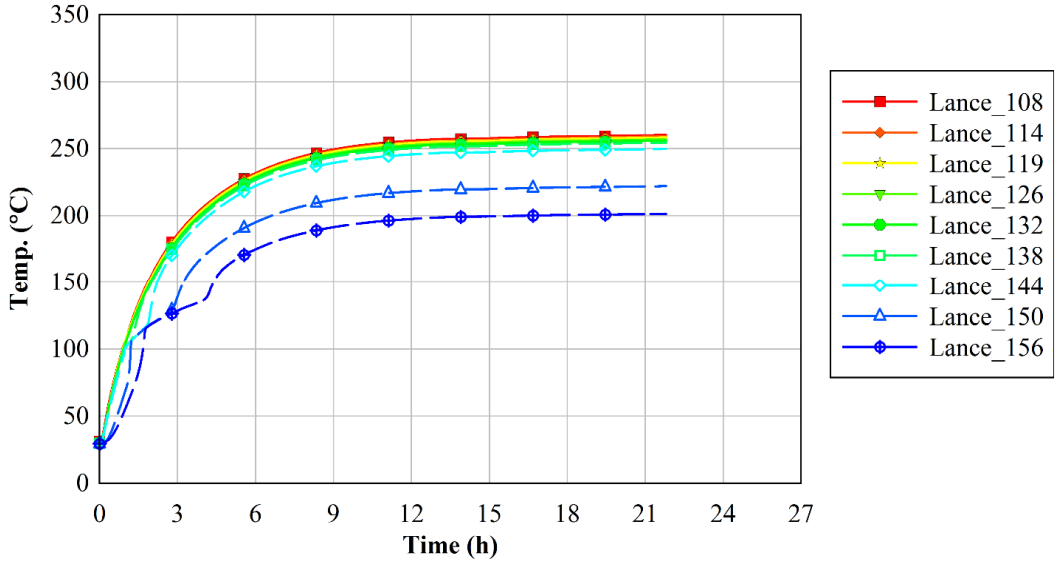

Figure B.12 TC lance data for the 2.5 kW test at 450 kPa on 7/19/2016.

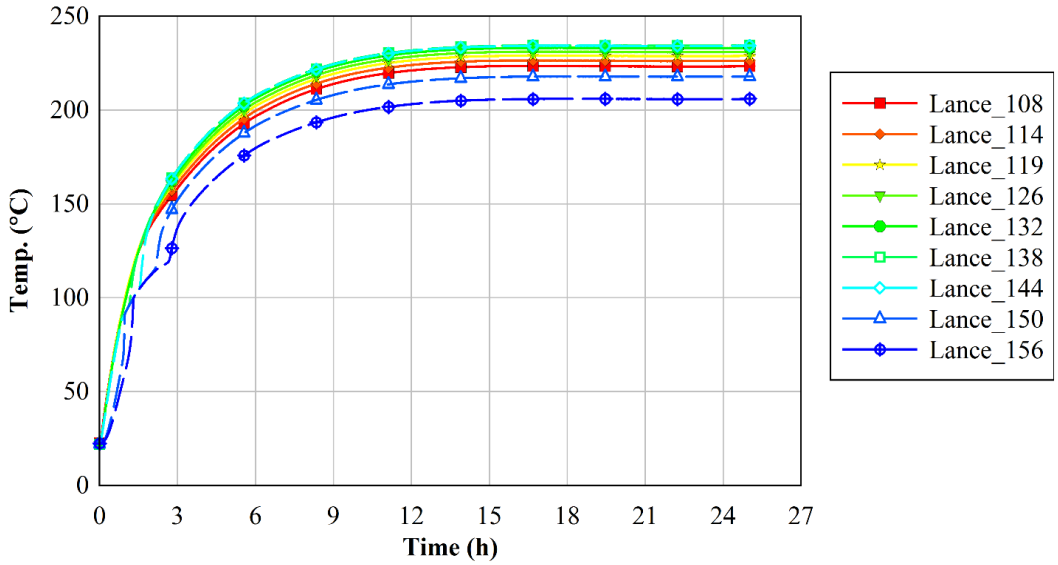

Figure B.13 TC lance data for the 2.5 kW test at 800 kPa on 6/27/2016.

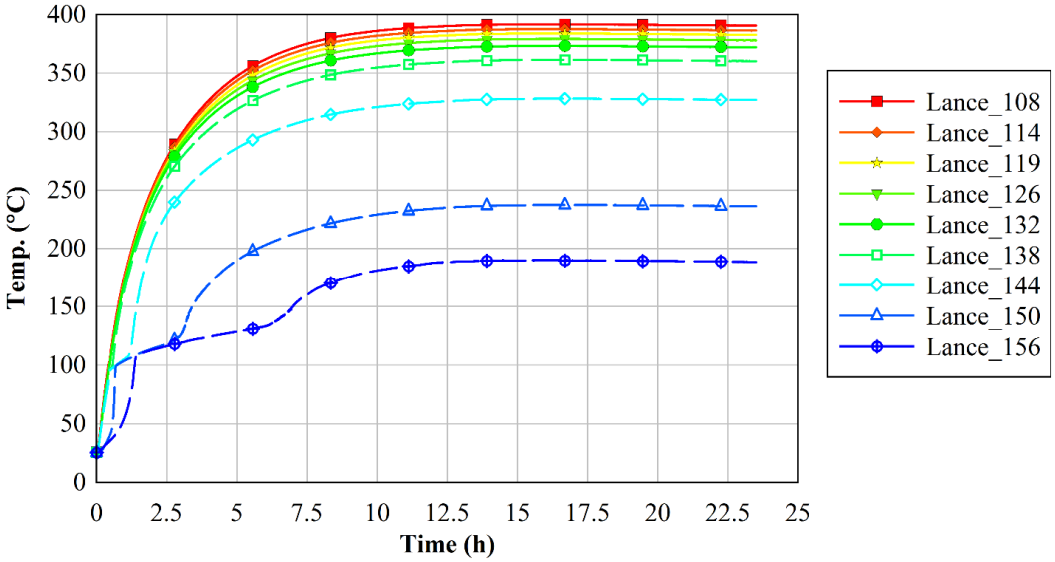

Figure B.14 TC lance data for the 5.0 kW test at 100 kPa on 8/1/2016.

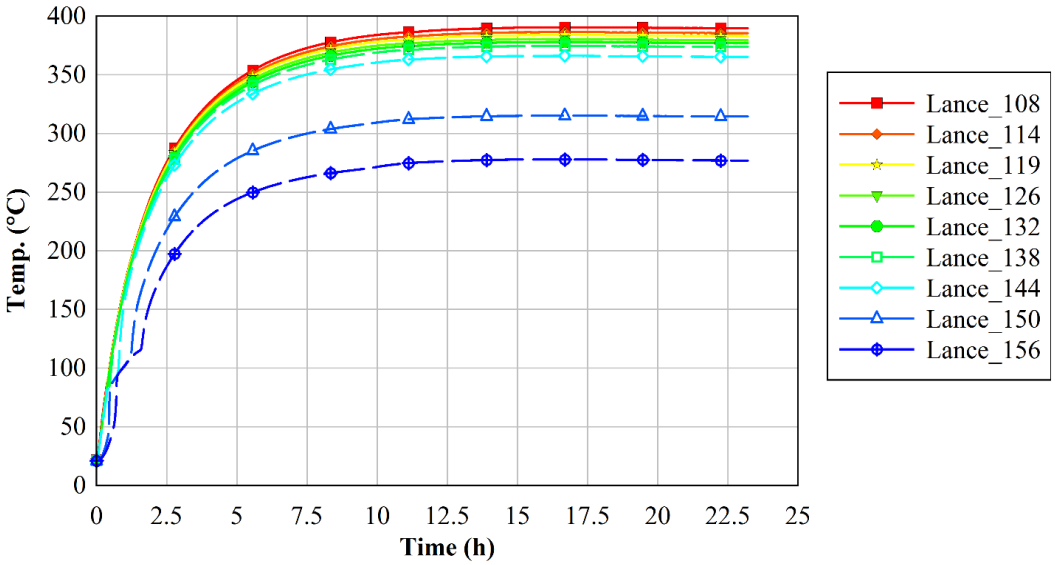

Figure B.15 TC lance data for the 5.0 kW test at 450 kPa on 7/13/2016.

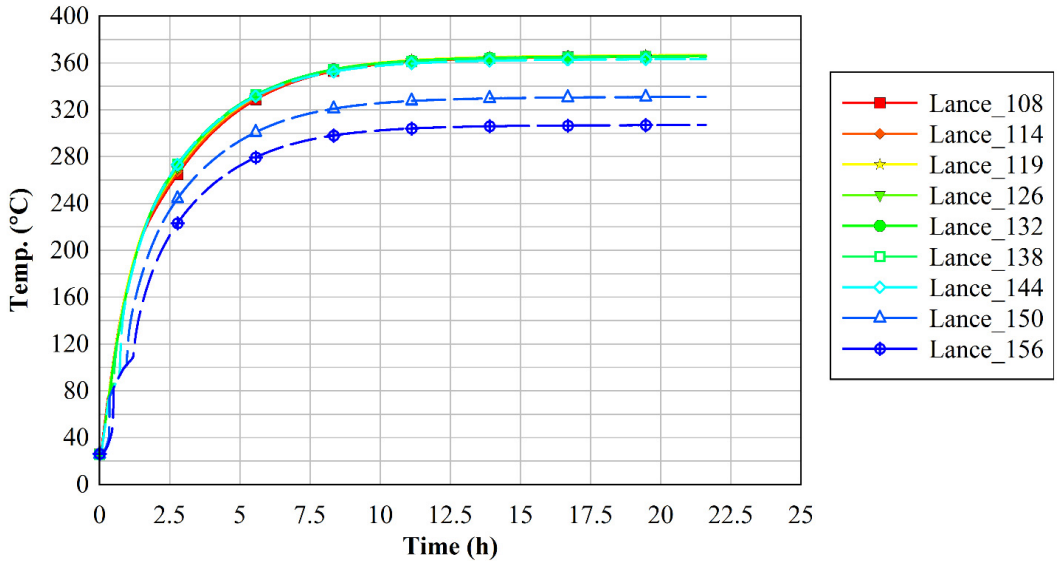

Figure B.16 TC lance data for the 5.0 kW test at 800 kPa on 6/23/2016.

Figure B.17 to Figure B.28 shows the lance TC at the 144" level along with the two closest neighboring (by symmetry) heater rod clad TCs. The heater rod clad TCs do not show any of the anomalous behavior. The lance TC is expected to indicate a temperature midway between the two heater rod TCs. For many tests the steady state lance temperature was midway between the two heater rod TCs. This was true for cases with and without anomalous behavior evident in the 144" lance TC. However, there were two cases where the steady state temperature of the 144" lance TC was clearly not midway between the neighboring heater rod TCs. The anomalous behavior of the lance TCs brought into question the validity of using the TC lance to measure the clad temperatures in the Cask Demonstration Project.

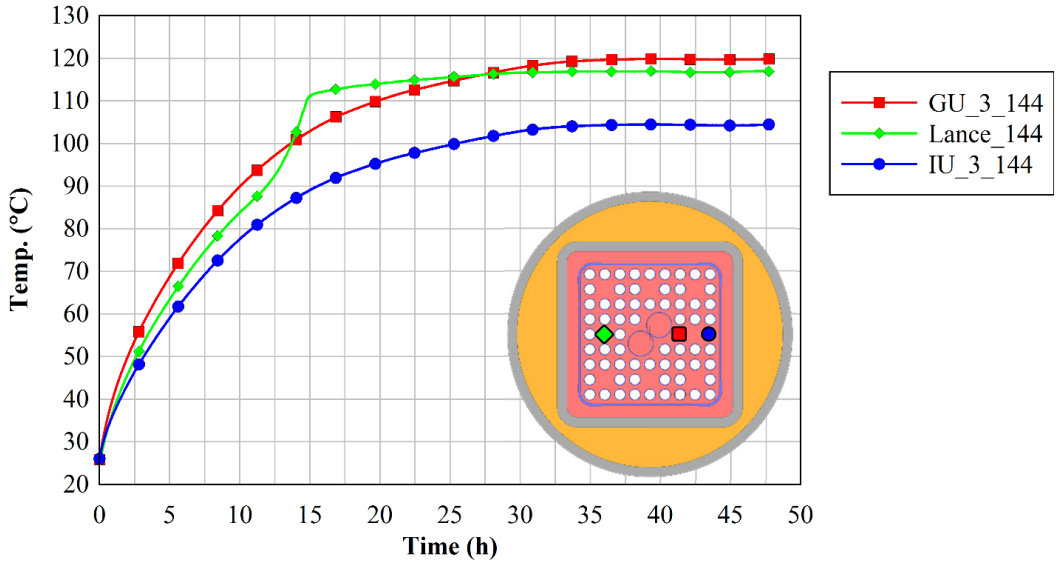

Figure B.17 Comparison of 144" TC lance data with 144" heater rod data for the 0.5 kW test at 3 kPa on 8/3/2016.

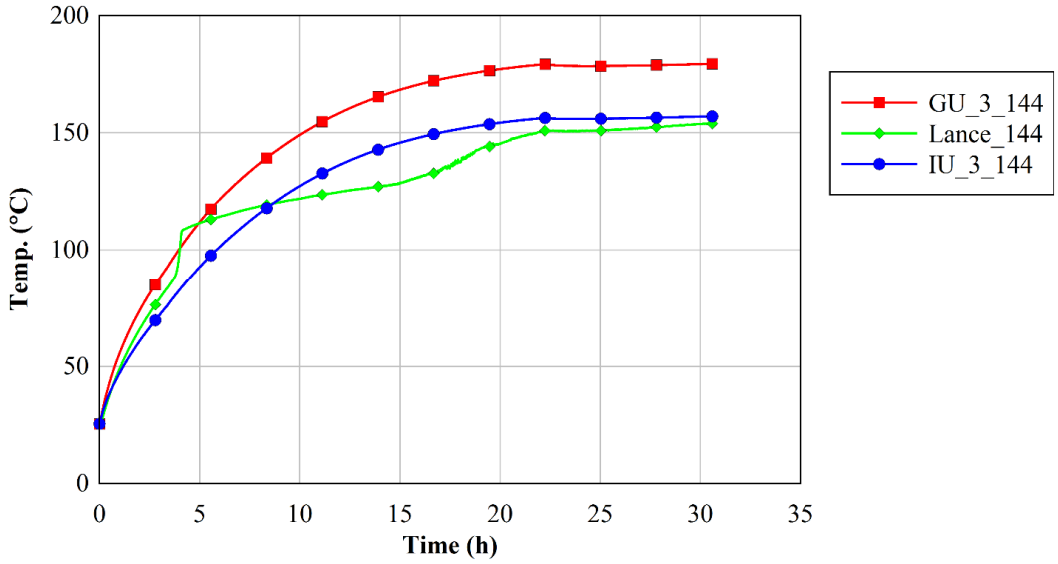

Figure B.18 Comparison of 144" TC lance data with 144" heater rod data for the 1.0 kW test at 3 kPa on 8/8/2016.

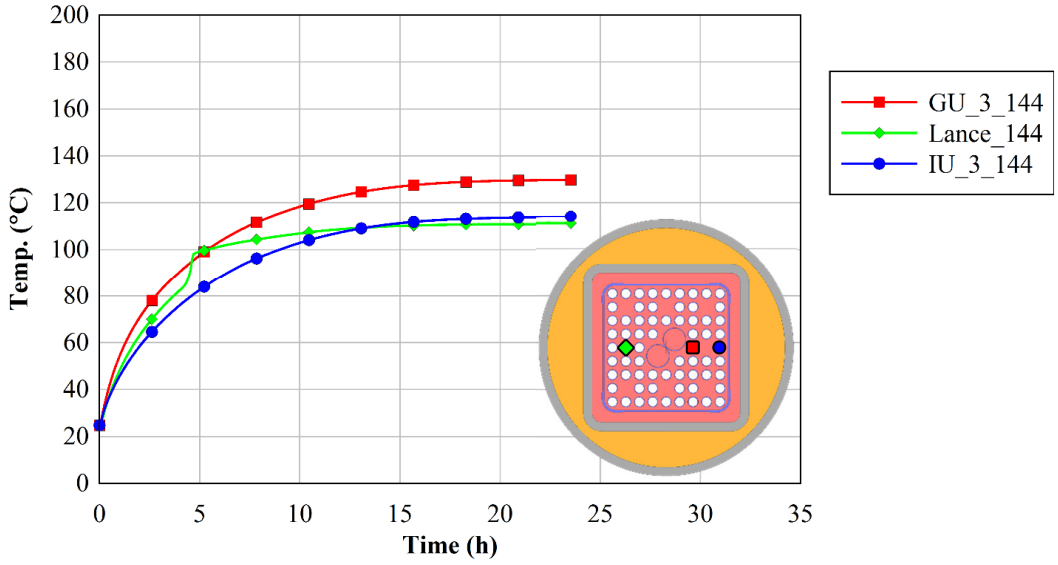

Figure B.19 Comparison of 144" TC lance data with 144" heater rod data for the 1.0 kW test at 100 kPa on 7/25/2016.

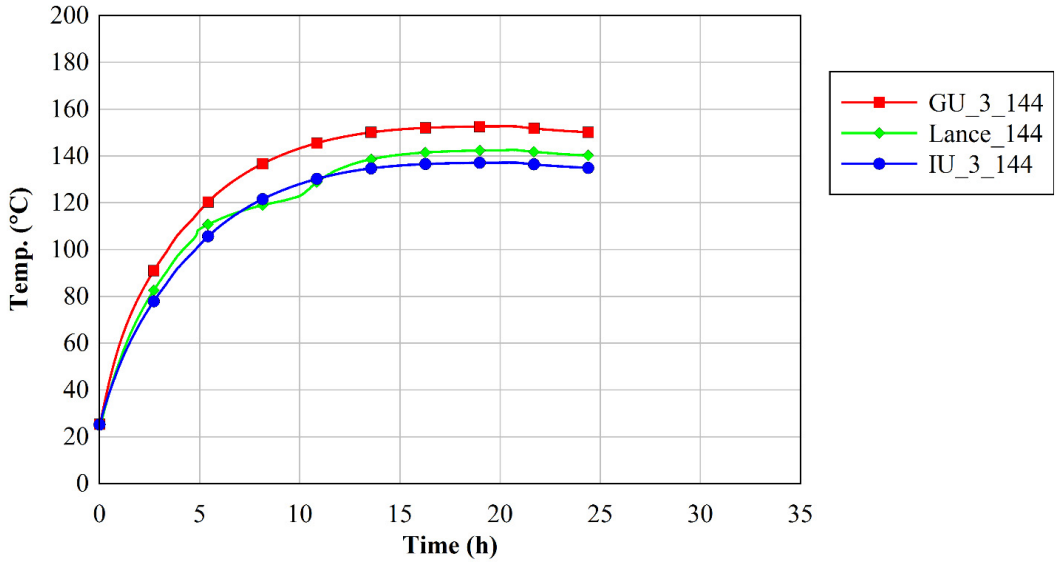

Figure B.20 Comparison of 144" TC lance data with 144" heater rod data for the 1.0 kW test at 450 kPa on 7/21/2016.

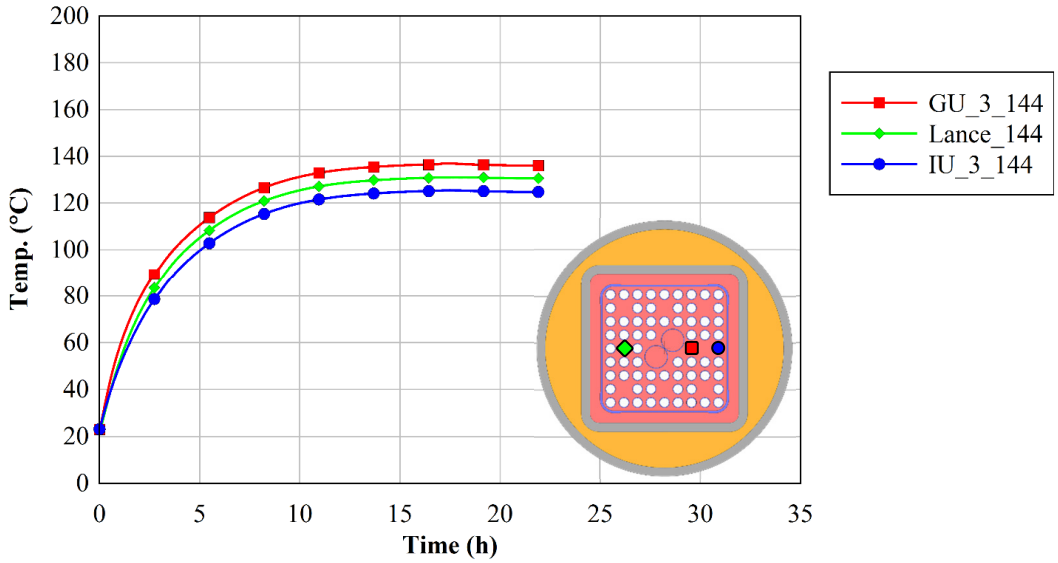

Figure B.21 Comparison of 144" TC lance data with 144" heater rod data for the 1.0 kW test at 800 kPa on 7/7/2016.

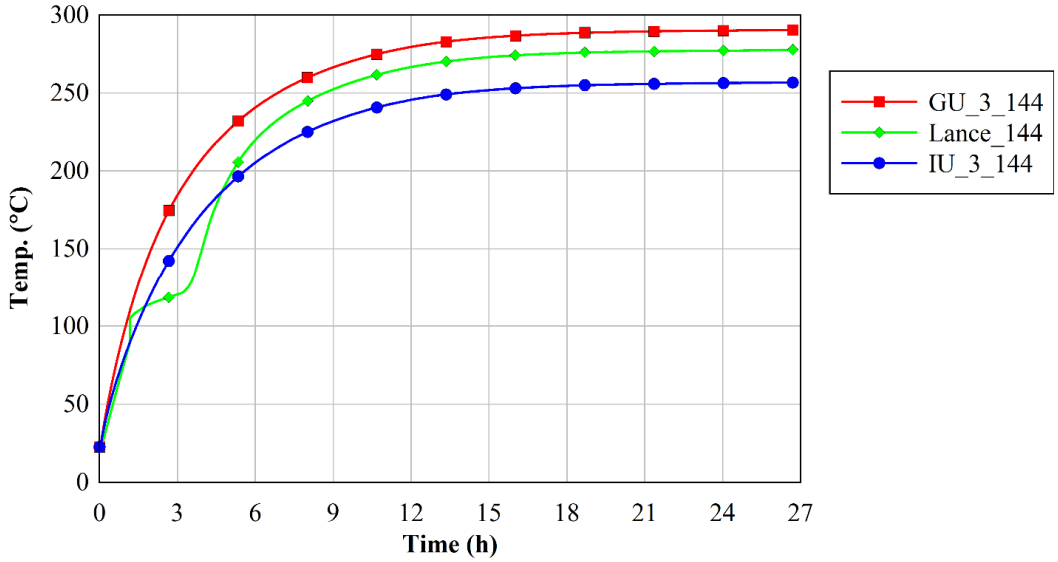

Figure B.22 Comparison of 144" TC lance data with 144" heater rod data for the 2.5 kW test at 3 kPa on 8/22/2016.

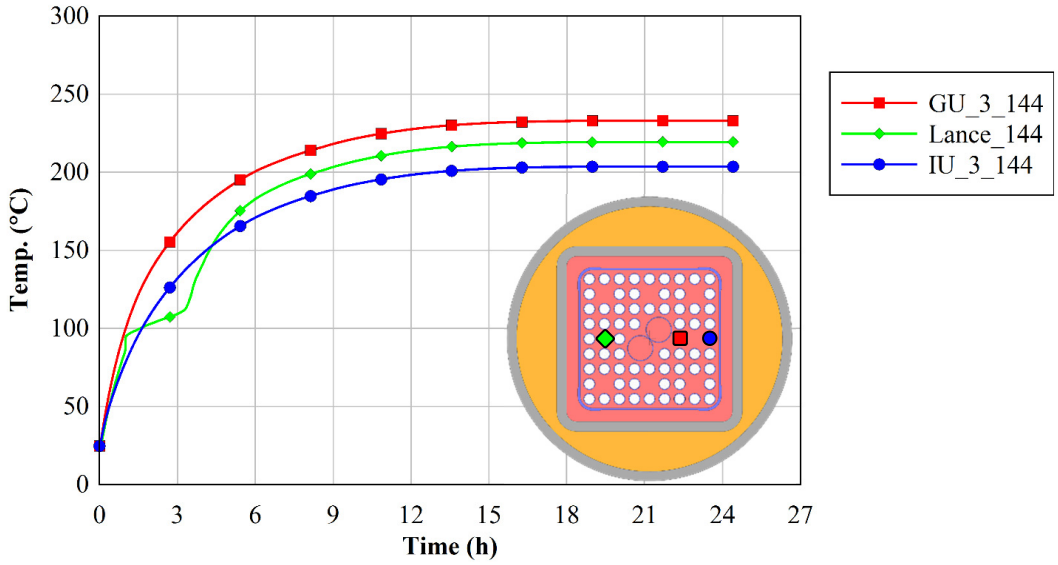

Figure B.23 Comparison of 144" TC lance data with 144" heater rod data for the 2.5 kW test at 100 kPa on 7/27/2016.

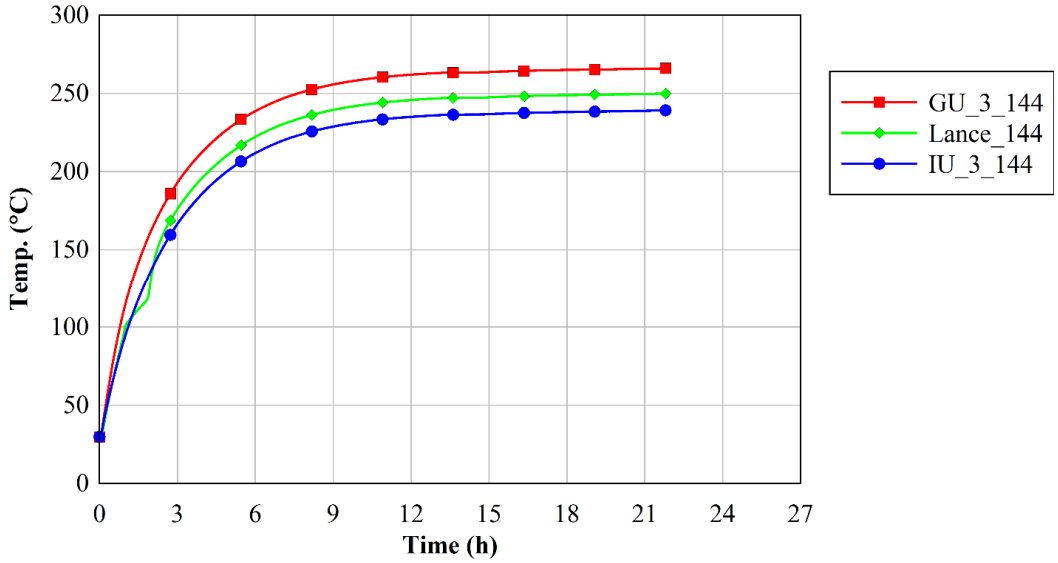

Figure B.24 Comparison of 144" TC lance data with 144" heater rod data for the 2.5 kW test at 450 kPa on 7/19/2016.

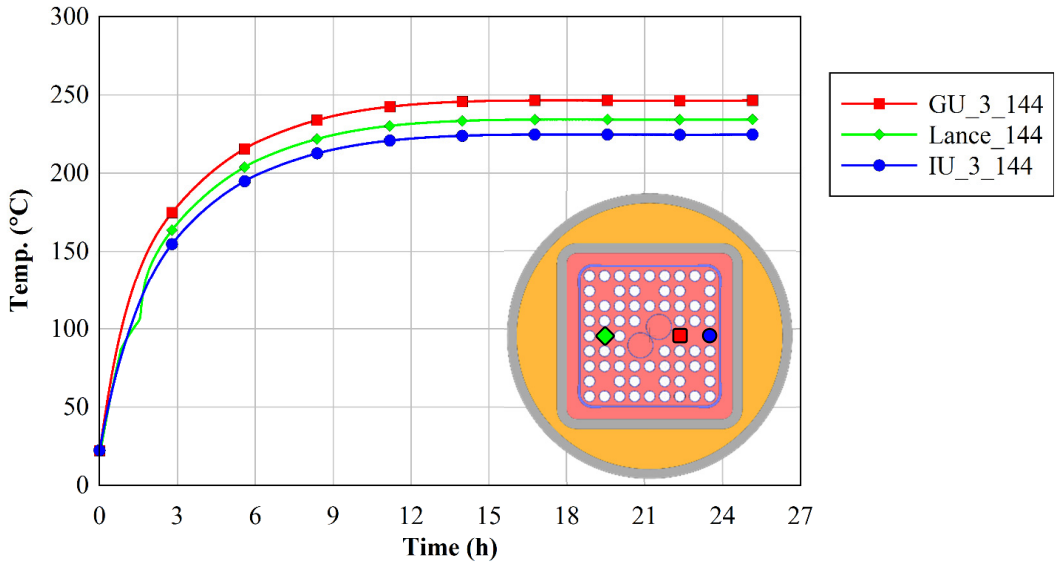

Figure B.25 Comparison of 144" TC lance data with 144" heater rod data for the 2.5 kW test at 800 kPa on 6/27/2016.

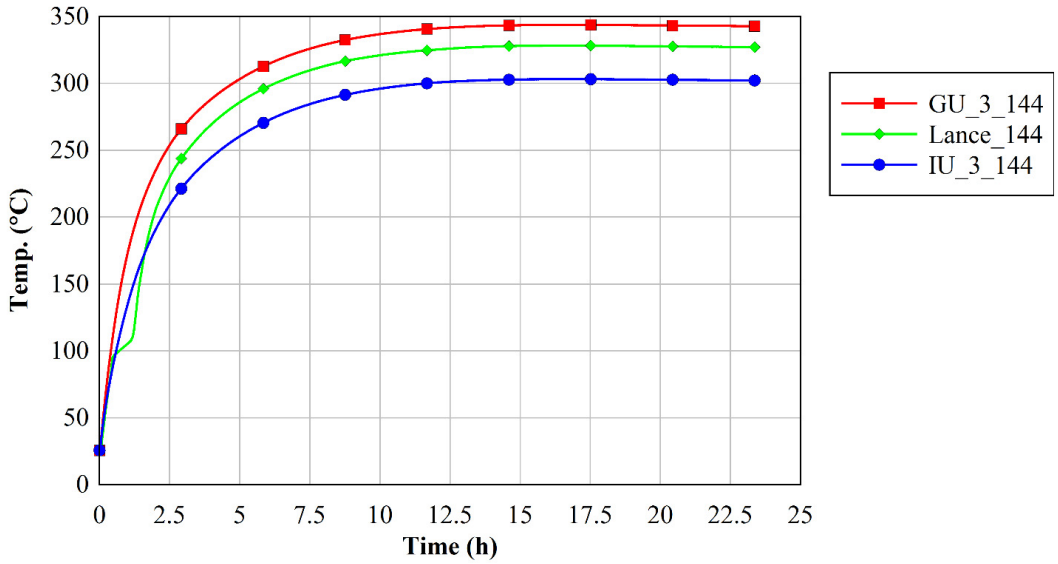

Figure B.26 Comparison of 144" TC lance data with 144" heater rod data for the 5.0 kW test at 100 kPa on 8/1/2016.

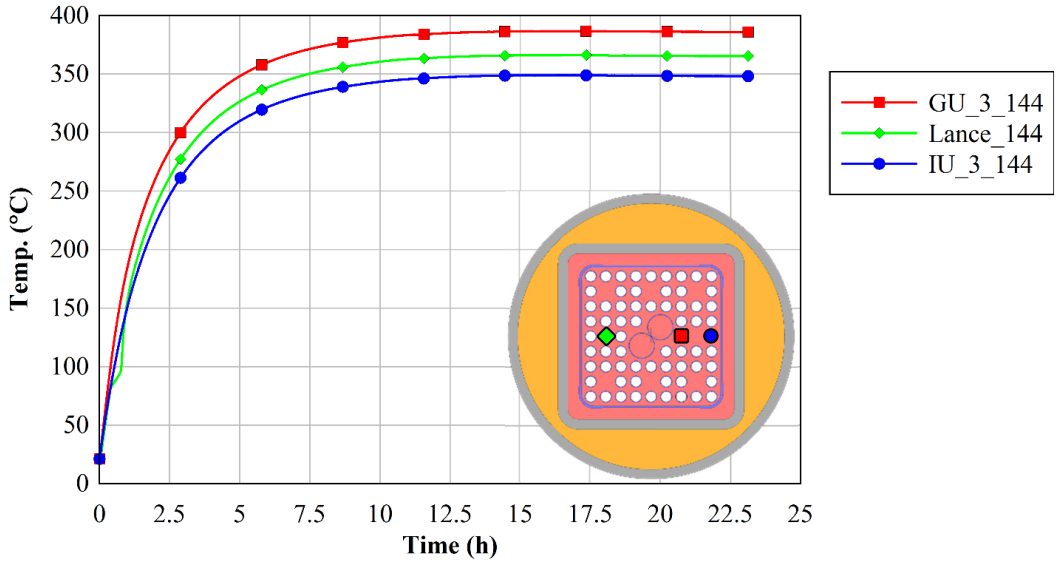

Figure B.27 Comparison of 144" TC lance data with 144" heater rod data for the 5.0 kW test at 450 kPa on 7/13/2016.

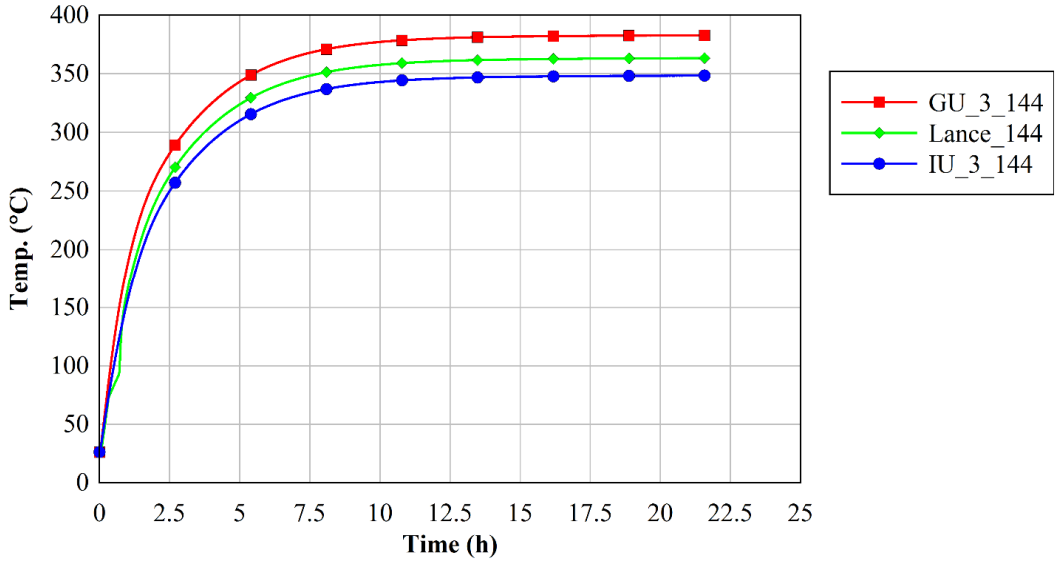

Figure B.28 Comparison of 144" TC lance data with 144" heater rod data for the 5.0 kW test at 800 kPa on 6/23/2016.

B.3 Responsible Phenomena Identification and Mitigation Plan

Discussions with the responsible technical staff at the lance vendor revealed that there was a unique braze closure at the top of the lance where the nine metallic TC sheathes exit. The braze closure forms a second (and redundant) pressure boundary that is not present on the TC lances to be used in the Cask Demonstration Project. A water based flux was used to form the braze closure. A hypothesis developed that some water based flux was trapped inside the TC lance and the anomalous behavior was due to complex phase change phenomena.

A mitigation plan was developed to breach the TC lance above the pressure seal for the pressure vessel but below the braze seal in a region where potential damage to the internal TC leads was minimal.

Venting the TC lance would allow the trapped moisture to escape when heated and prevent the TC lance internals from pressurizing. Figure B.29a shows a guidance drawing provided by the lance vendor and Figure B.29b shows an image of the as-implemented lance breach.

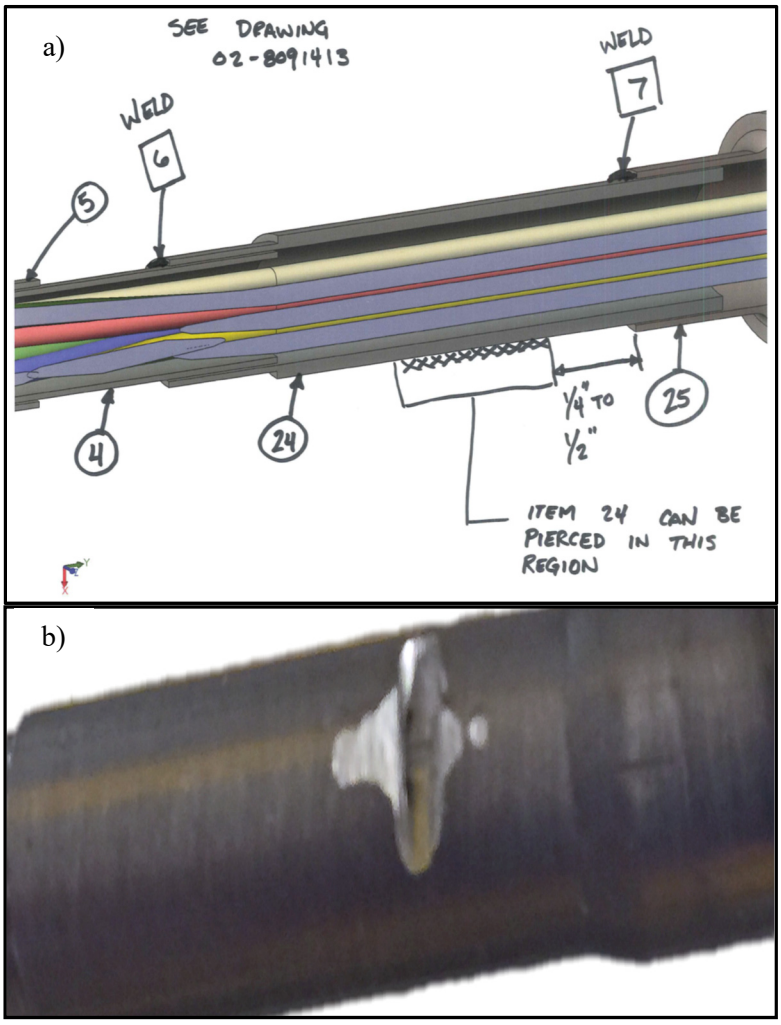

Figure B.29 a) Guidance diagram showing optimal location of the proposed breach. b) Photo of the as-implemented breach.

B.4 Mitigation Results

Implementation of the mitigation plan seemed to correct the problem. Figure B.30a shows TC lance data before the lance was breached. Notice after an hour when the lance TC at 108" reached 100 °C the upper lance TCs began to exhibit anomalous behavior. Figure B.30b shows TC lance data for a repeat run after the lance was breached. Notice there is no anomalous behavior even as all TC reach temperatures above 100 °C.

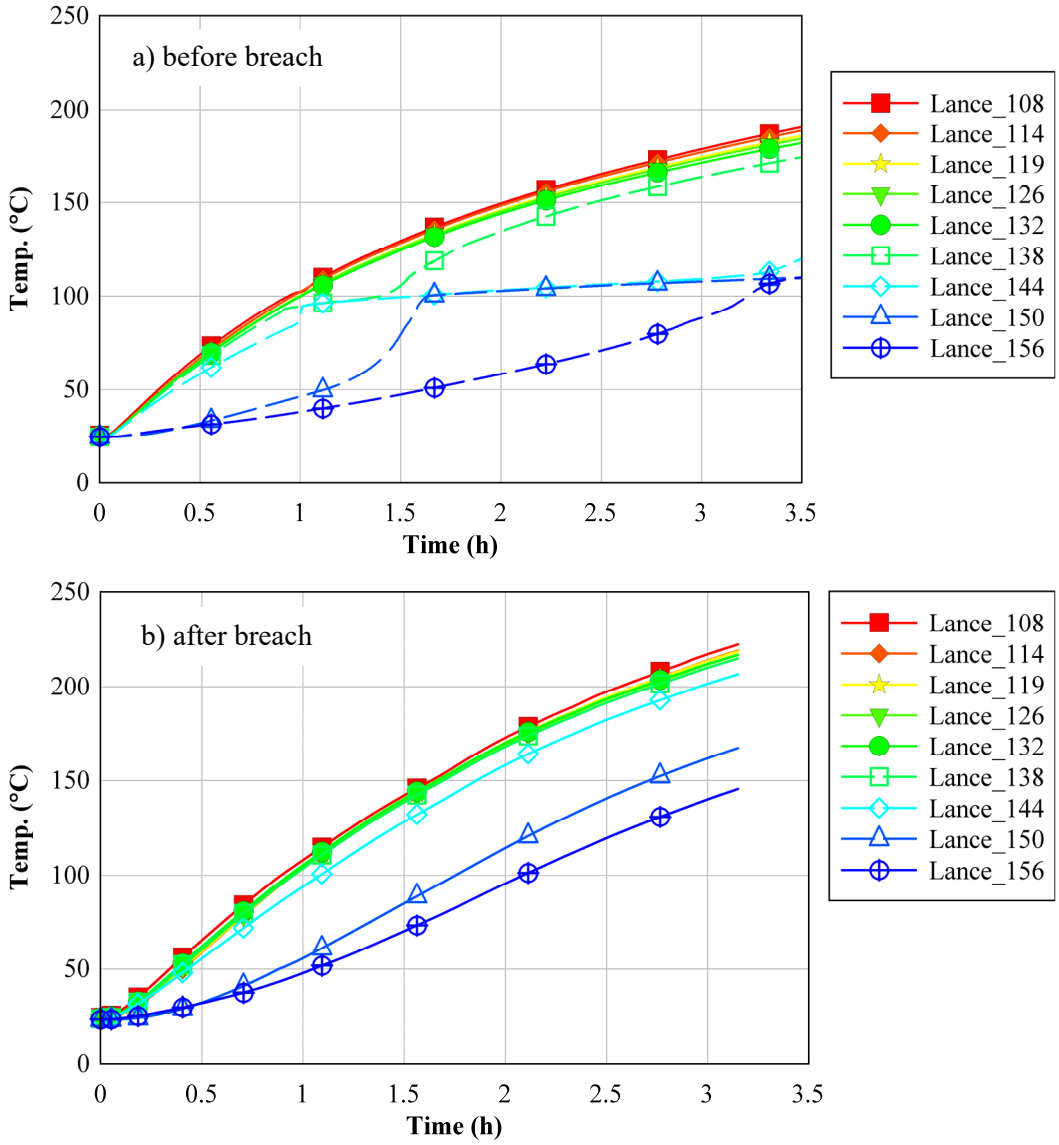

Figure B.30 a) Anomalous TC lance behavior for the 2.5 kW test at 100 kPa conducted on 7/27/2016 before the lance was breached. b) TC lance data for the same test conditions conducted on 5/1/2017 after the lance was breached.

APPENDIX C CHANNEL LIST FROM ABOVEGROUND TESTING

The results presented in the body of the test report describe the most important quantities as determined by the authors. This presentation represents a fraction of the information collected from the test assembly. Table C.1 gives the complete channel list for the aboveground configuration as an example to the reader of the extent of the available data.

Table C.1 Channel list for aboveground configuration testing.

Slot	Channel	TC #	Instrument Nomenclature	Instrument Type
1	0	1	WDV - IN	Type "K" TC
1	1	2	WDV - OUT	Type "K" TC
1	2	3	WFT - IN	Type "K" TC
1	3	4	WFT - OUT	Type "K" TC
1	4	5	WEU24	Type "K" TC
1	5	6	WEU48	Type "K" TC
1	6	7	WEU72	Type "K" TC
1	7	8	WEU96	Type "K" TC
1	8	9	No_Data	Type "K" TC
1	9	10	WEU144	Type "K" TC
1	10	11	WDV24_1	Type "K" TC
1	11	12	WDV96_1	Type "K" TC
1	12	13	WFT48_2A	Type "K" TC
1	13	14	WFT72_3A	Type "K" TC
1	14	15	WFT119_2A	Type "K" TC
1	15	16	WFT144_3A	Type "K" TC
1	16	17	DT24_1	Type "K" TC
1	17	18	DT48_2	Type "K" TC
1	18	19	DT96_1	Type "K" TC
1	19	20	DT119_2	Type "K" TC
1	20	21	CU24_1	Type "K" TC
1	21	22	CU96_1	Type "K" TC
1	22	23	ES48_2	Type "K" TC
1	23	24	ES119_2	Type "K" TC
1	24	25	CX24_1	Type "K" TC
1	25	26	CX96_1	Type "K" TC
1	26	27	GS48_2	Type "K" TC
1	27	28	GS72_3	Type "K" TC
1	28	29	GS119_2	Type "K" TC
1	29	30	GS144_3	Type "K" TC
1	30	31	GU72_3	Type "K" TC
1	31	32	GU144_3	Type "K" TC
2	0	33	FV72_3	Type "K" TC
2	1	34	FV144_3	Type "K" TC
2	2	35	CS6_1A	Type "K" TC
2	3	36	CS12_1A	Type "K" TC
2	4	37	CS18_1A	Type "K" TC
2	5	38	CS24_1	Type "K" TC
2	6	39	CS30_1A	Type "K" TC
2	7	40	CS36_1A	Type "K" TC
2	8	41	CS42_2A	Type "K" TC
2	9	42	CS48_2	Type "K" TC
2	10	43	CS54_2A	Type "K" TC
2	11	44	CS61_2A	Type "K" TC
2	12	45	CS90_1A	Type "K" TC
2	13	46	CS96_1	Type "K" TC
2	14	47	CS103_1A	Type "K" TC
2	15	48	CS108_1A	Type "K" TC
2	16	49	CS114_2A	Type "K" TC
2	17	50	CS119_2	Type "K" TC
2	18	51	CS126_2A	Type "K" TC
2	19	52	CS132_2A	Type "K" TC
2	20	53	No_Data	Type "K" TC
2	21	54	GX72_3	Type "K" TC
2	22	55	GX78_3A	Type "K" TC
2	23	56	GX84_3A	Type "K" TC
2	24	57	GX138_3A	Type "K" TC
2	25	58	GX144_3	Type "K" TC
2	26	59	GX150_3A	Type "K" TC
2	27	60	GX156_3A	Type "K" TC
2	28	61	AQ24_1	Type "K" TC
2	29	62	AQ48_2	Type "K" TC
2	30	63	AQ96_1	Type "K" TC
2	31	64	AQ119_2	Type "K" TC

Slot	Channel	TC #	Instrument Nomenclature	Instrument Type
3	0	65	AS24_1	Type "K" TC
3	1	66	AS96_1	Type "K" TC
3	2	67	No_Data	Type "K" TC
3	3	68	No_Data	Type "K" TC
3	4	69	No_Data	Type "K" TC
3	5	70	AU96_1	Type "K" TC
3	6	71	AU108_1	Type "K" TC
3	7	72	No_Data	Type "K" TC
3	8	73	AX96_1	Type "K" TC
3	9	74	AZ24_1	Type "K" TC
3	10	75	AZ96_1	Type "K" TC
3	11	76	CQ48_2	Type "K" TC
3	12	77	CQ119_2	Type "K" TC
3	13	78	EQ48_2	Type "K" TC
3	14	79	EQ60_2	Type "K" TC
3	15	80	EQ119_2	Type "K" TC
3	16	81	EQ132_2	Type "K" TC
3	17	82	GQ48_2	Type "K" TC
3	18	83	GQ119_2	Type "K" TC
3	19	84	IQ48_2	Type "K" TC
3	20	85	IQ72_3	Type "K" TC
3	21	86	IQ119_2	Type "K" TC
3	22	87	IQ144_3	Type "K" TC
3	23	88	IS72_3	Type "K" TC
3	24	89	IS144_3	Type "K" TC
3	25	90	IU72_3	Type "K" TC
3	26	91	IU84_3	Type "K" TC
3	27	92	IU144_3	Type "K" TC
3	28	93	IU156_3	Type "K" TC
3	29	94	IX72_3	Type "K" TC
3	30	95	IX144_3	Type "K" TC
3	31	96	IZ72_3	Type "K" TC
4	0	97	IZ144_3	Type "K" TC
4	1	98	Instr_Well_Leads	Type "K" TC
4	2	99	Instr_Well_Int	Type "K" TC
4	3	100	Pedestal_Base	Type "K" TC
4	4	101	Pedestal_(-5.5)_4	Type "K" TC
4	5	102	Channel_0_4	Type "K" TC
4	6	103	Channel_12_1	Type "K" TC
4	7	104	Channel_24_1	Type "K" TC
4	8	105	Channel_24_4	Type "K" TC
4	9	106	Channel_24_4-1	Type "K" TC
4	10	107	Channel_36_2	Type "K" TC
4	11	108	Channel_48_2	Type "K" TC
4	12	109	Channel_48_4	Type "K" TC
4	13	110	Channel_60_3	Type "K" TC
4	14	111	Channel_72_3	Type "K" TC
4	15	112	Channel_72_4	Type "K" TC
4	16	113	Channel_72_3-4	Type "K" TC
4	17	114	Channel_84_1	Type "K" TC
4	18	115	Channel_96_1	Type "K" TC
4	19	116	Channel_96_4	Type "K" TC
4	20	117	Channel_108_2	Type "K" TC
4	21	118	Channel_119_2	Type "K" TC
4	22	119	Channel_119_4	Type "K" TC
4	23	120	Channel_119_2-3	Type "K" TC
4	24	121	Channel_132_3	Type "K" TC
4	25	122	Channel_144_3	Type "K" TC
4	26	123	Channel_144_4	Type "K" TC
4	27	124	Channel_156_1	Type "K" TC
4	28	125	Channel_159_4	Type "K" TC
4	29	126	g48_C-B_2.9_4	Type "K" TC
4	30	127	g72_C-B_2.9_2	Type "K" TC
4	31	128	g96_C-B_4.0_4-1	Type "K" TC
5	0	129	g96_C-B_2.9_1	Type "K" TC
5	1	130	g96_C-B_2.9_1S	Type "K" TC
5	2	131	g144_C-B_2.9_1	Type "K" TC
5	3	132	g144_C-B_2.9_1S	Type "K" TC
5	4	133	g144_C-B_4.0_3-4	Type "K" TC
5	5	134	g144_C-B_2.9_3	Type "K" TC
5	6	135	g144_C-B_2.9_3S	Type "K" TC
5	7	136	Basket_Int_12_1	Type "K" TC
5	8	137	Basket_(-5.5)_4	Type "K" TC
5	9	138	Basket_0_4	Type "K" TC
5	10	139	Basket_12_1	Type "K" TC
5	11	140	Basket_24_1	Type "K" TC
5	12	141	Basket_24_4	Type "K" TC
5	13	142	Basket_24_4-1	Type "K" TC
5	14	143	Basket_36_2	Type "K" TC
5	15	144	Basket_48_2	Type "K" TC
5	16	145	Basket_48_4	Type "K" TC
5	17	146	Basket_60_3	Type "K" TC
5	18	147	Basket_72_3	Type "K" TC
5	19	148	Basket_72_4	Type "K" TC
5	20	149	Basket_72_3-4	Type "K" TC
5	21	150	Basket_84_1	Type "K" TC
5	22	151	Basket_96_1	Type "K" TC
5	23	152	Basket_96_4	Type "K" TC
5	24	153	Basket_108_2	Type "K" TC
5	25	154	Basket_119_2	Type "K" TC
5	26	155	Basket_119_4	Type "K" TC
5	27	156	Basket_119_2-3	Type "K" TC
5	28	157	Basket_132_3	Type "K" TC
5	29	158	Basket_144_3	Type "K" TC
5	30	159	Basket_144_4	Type "K" TC
5	31	160	Basket_156_1	Type "K" TC
6	0	161	Basket_159_4	Type "K" TC
6	1	162	Basket_165_4-1	Type "K" TC
6	2	163	Basket_Int_156_1	Type "K" TC
6	3	164	g(-7.6)_B-V_3.5_2	Type "K" TC
6	4	165	g48_B-V_4.3_4	Type "K" TC
6	5	166	g48_B-V_4.8_3-4	Type "K" TC
6	6	167	g72_B-V_4.3_2	Type "K" TC
6	7	168	g96_B-V_4.8_4-1	Type "K" TC
6	8	169	g96_B-V_3.8_1	Type "K" TC
6	9	170	g96_B-V_4.3_1	Type "K" TC
6	10	171	g96_B-V_4.8_1	Type "K" TC
6	11	172	g144_B-V_4.3_1	Type "K" TC
6	12	173	g144_B-V_4.3_1S	Type "K" TC
6	13	174	g144_B-V_4.8_3-4	Type "K" TC
6	14	175	g144_B-V_3.8_3	Type "K" TC
6	15	176	g144_B-V_4.3_3	Type "K" TC
6	16	177	g144_B-V_4.8_3	Type "K" TC
6	17	178	g167_B-V_3.5_3	Type "K" TC
6	18	179	g167_B-V_3.5_1S	Type "K" TC
6	19	180	PV_Int_12_1	Type "K" TC
6	20	181	PV_0_4	Type "K" TC
6	21	182	PV_12_1	Type "K" TC
6	22	183	PV_24_1	Type "K" TC
6	23	184	PV_24_4	Type "K" TC
6	24	185	PV_24_4-1	Type "K" TC
6	25	186	PV_36_2	Type "K" TC
6	26	187	PV_48_2	Type "K" TC
6	27	188	PV_48_4	Type "K" TC
6	28	189	PV_60_3	Type "K" TC
6	29	190	PV_72_3	Type "K" TC
6	30	191	PV_72_4	Type "K" TC
6	31	192	PV_72_3-4	Type "K" TC

Slot	Channel	TC #	Instrument Nomenclature	Instrument Type
7	0	193	PV_84_1	Type "K" TC
7	1	194	PV_96_1	Type "K" TC
7	2	195	PV_96_4	Type "K" TC
7	3	196	PV_108_2	Type "K" TC
7	4	197	PV_119_2	Type "K" TC
7	5	198	PV_119_3	Type "K" TC
7	6	199	PV_119_4	Type "K" TC
7	7	200	PV_119_2-3	Type "K" TC
7	8	201	PV_132_3	Type "K" TC
7	9	202	PV_144_1	Type "K" TC
7	10	203	PV_144_3	Type "K" TC
7	11	204	PV_144_4	Type "K" TC
7	12	205	PV_156_1	Type "K" TC
7	13	206	PV_159_4	Type "K" TC
7	14	207	PV_165_4	Type "K" TC
7	15	208	PV_Int_156_1	Type "K" TC
7	16	209	g48_V-S1_5.6_4	Type "K" TC
7	17	210	g48_V-S1_6.4_4	Type "K" TC
7	18	211	g48_V-S1_7.2_4	Type "K" TC
7	19	212	g48_V-S1_8.1_4	Type "K" TC
7	20	213	g48_V-S1_7.2_3-4	Type "K" TC
7	21	214	g96_V-S1_5.6_1	Type "K" TC
7	22	215	g96_V-S1_6.4_1S	Type "K" TC
7	23	216	g96_V-S1_7.2_1	Type "K" TC
7	24	217	g96_V-S1_8.1_1S	Type "K" TC
7	25	218	g96_V-S1_7.2_4-1	Type "K" TC
7	26	219	g96_V-S1_7.2_4	Type "K" TC
7	27	220	g144_V-S1_7.2_3-4	Type "K" TC
7	28	221	g144_V-S1_7.2_3	Type "K" TC
7	29	222	S1_0_4	Type "K" TC
7	30	223	S1_12_1	Type "K" TC
7	31	224	S1_24_1-4	Type "K" TC

Slot	Channel	TC #	Instrument Nomenclature	Instrument Type
8	0	225	S1_24_1	Type "K" TC
8	1	226	S1_24_4	Type "K" TC
8	2	227	S1_36_2	Type "K" TC
8	3	228	S1_48_2	Type "K" TC
8	4	229	S1_48_4	Type "K" TC
8	5	230	S1_60_3	Type "K" TC
8	6	231	S1_72_3-4	Type "K" TC
8	7	232	S1_72_3	Type "K" TC
8	8	233	S1_72_4	Type "K" TC
8	9	234	S1_84_1	Type "K" TC
8	10	235	S1_96_1	Type "K" TC
8	11	236	S1_96_4	Type "K" TC
8	12	237	S1_108_2	Type "K" TC
8	13	238	S1_119_2-3	Type "K" TC
8	14	239	S1_119_2	Type "K" TC
8	15	240	S1_119_3	Type "K" TC
8	16	241	S1_119_4	Type "K" TC
8	17	242	S1_132_3	Type "K" TC
8	18	243	S1_144_1	Type "K" TC
8	19	244	S1_144_3	Type "K" TC
8	20	245	S1_144_4	Type "K" TC
8	21	246	S1_156_1	Type "K" TC
8	22	247	S1_159_4	Type "K" TC
8	23	248	S1_170_4	Type "K" TC
8	24	249	g48_S1-S2_9.7_4	Type "K" TC
8	25	250	g48_S1-S2_10.8_4	Type "K" TC
8	26	251	g48_S1-S2_12_4	Type "K" TC
8	27	252	g48_S1-S2_10.8_3-4S	Type "K" TC
8	28	253	g96_S1-S2_9.7_1	Type "K" TC
8	29	254	g96_S1-S2_10.8_1	Type "K" TC
8	30	255	g96_S1-S2_12_1	Type "K" TC
8	31	256	g96_S1-S2_10.8_4-1S	Type "K" TC

Slot	Channel	TC #	Instrument Nomenclature	Instrument Type
9	0	257	g96_S1-S2_10.8_4	Type "K" TC
9	1	258	g144_S1-S2_10.8_3-4S	Type "K" TC
9	2	259	g144_S1-S2_10.8_3	Type "K" TC
9	3	260	S2_0_4	Type "K" TC
9	4	261	S2_12_1	Type "K" TC
9	5	262	S2_24_1-4	Type "K" TC
9	6	263	S2_24_1	Type "K" TC
9	7	264	S2_24_4	Type "K" TC
9	8	265	S2_36_2	Type "K" TC
9	9	266	S2_48_2	Type "K" TC
9	10	267	S2_48_4	Type "K" TC
9	11	268	S2_60_3	Type "K" TC
9	12	269	S2_72_3-4	Type "K" TC
9	13	270	S2_72_3	Type "K" TC
9	14	271	S2_72_4	Type "K" TC
9	15	272	S2_84_1	Type "K" TC
9	16	273	S2_96_1	Type "K" TC
9	17	274	S2_96_4	Type "K" TC
9	18	275	S2_108_2	Type "K" TC
9	19	276	S2_119_2-3	Type "K" TC
9	20	277	S2_119_2	Type "K" TC
9	21	278	S2_119_3	Type "K" TC
9	22	279	S2_119_4	Type "K" TC
9	23	280	S2_132_3	Type "K" TC
9	24	281	S2_144_1	Type "K" TC
9	25	282	S2_144_3	Type "K" TC
9	26	283	S2_144_4	Type "K" TC
9	27	284	Lance_108	Type "K" TC
9	28	285	Lance_114	Type "K" TC
9	29	286	Lance_119	Type "K" TC
9	30	287	Lance_126	Type "K" TC
9	31	288	Lance_132	Type "K" TC

Slot	Channel	TC #	Instrument Nomenclature	Instrument Type
10	0	289	Lance_138	Type "K" TC
10	1	290	Lance_144	Type "K" TC
10	2	291	Lance_150	Type "K" TC
10	3	292	Lance_156	Type "K" TC
10	4	293	S1_96_1_Ins	Type "K" TC
10	5	294	S1_96_4_Ins	Type "K" TC
10	6	295	S1_48_4_Ins	Type "K" TC
10	7	296	S1_144_3_Ins	Type "K" TC
10	8	297	S1_144_3-4_Ins	Type "K" TC
10	9	298	S1_96_1-4_Ins	Type "K" TC
10	10	299	S1_48_3-4_Ins	Type "K" TC
10	11	300	S1_144_3_X-tra	Type "K" TC
10	12	301	S1_96_1_X-tra	Type "K" TC
10	13	302	S1_48_4_X-tra	Type "K" TC
10	14	303	PRV_Temp	Type "K" TC
10	15	304	Ext_Well_Mid_Flange	Type "K" TC
10	16	305	Ext_Mid_Well	Type "K" TC
10	17	306	Elc_Feed_Tube	Type "K" TC
10	18	307	Good_No_Data	Type "K" TC
10	19	308	Building_Heat	Type "K" TC
10	20	309	ForcedAir_Temp	Type "K" TC
10	21	310	Ambient_-24	Type "K" TC
10	22	311	Ambient_-12	Type "K" TC
10	23	312	Ambient_0	Type "K" TC
10	24	313	Ambient_24	Type "K" TC
10	25	314	Ambient_48	Type "K" TC
10	26	315	Ambient_72	Type "K" TC
10	27	316	Ambient_96	Type "K" TC
10	28	317	Ambient_120	Type "K" TC
10	29	318	Ambient_144	Type "K" TC
10	30	319	Ambient_168	Type "K" TC
10	31	320	Ambient_192	Type "K" TC

Slot	Channel		TC #	Instrument Nomenclature	Instrument Type
11	0		321	S1_2-3_171	Type "K" TC
11	1		322	S1_2_171	Type "K" TC
11	2		323	PV_Top_-1.375	Type "K" TC
11	3		324	Flow_straight_temp	Type "K" TC
11	4		325	North_Air_Inlet	Type "K" TC
11	5		326	West_Air_Inlet	Type "K" TC
11	6		327	East_Air_Inlet	Type "K" TC
11	7		328	South_Air_Inlet	Type "K" TC
11	8		329	CYBL_Wall_Amb_0	Type "K" TC
11	9		330	CYBL_Wall_Amb_72	Type "K" TC
11	10		331	CYBL_Wall_Amb_144	Type "K" TC
11	11		332	Inlet_Top_1	Type "K" TC
11	12		333	Inlet_Air_1_1	Type "K" TC
11	13		334	Inlet_Bottom_1	Type "K" TC
11	14		335	Inlet_Top_2	Type "K" TC
11	15		336	Inlet_Air_1_2	Type "K" TC
11	16		337	Inlet_Bottom_2	Type "K" TC
11	17		338	Inlet_Top_3	Type "K" TC
11	18		339	Inlet_Air_1_3	Type "K" TC
11	19		340	Inlet_Bottom_3	Type "K" TC
11	20		341	Inlet_Top_4	Type "K" TC
11	21		342	Inlet_Air_1_4	Type "K" TC
11	22		343	Inlet_Bottom_4	Type "K" TC
11	23		344	Outlet_Top_1	Type "K" TC
11	24		345	Outlet_Air_7_1	Type "K" TC
11	25		346	Outlet_Air_4_1	Type "K" TC
11	26		347	Outlet_Air_1_1	Type "K" TC
11	27		348	Outlet_Bottom_1	Type "K" TC
11	28		349	Outlet_Top_2	Type "K" TC
11	29		350	Outlet_Air_7_2	Type "K" TC
11	30		351	Outlet_Air_4_2	Type "K" TC
11	31		352	Outlet_Air_1_2	Type "K" TC

Slot	Channel		TC #	Instrument Nomenclature	Instrument Type
12	0		353	Outlet_Bottom_2	Type "K" TC
12	1		354	Outlet_Top_3	Type "K" TC
12	2		355	Outlet_Air_7_3	Type "K" TC
12	3		356	Outlet_Air_4_3	Type "K" TC
12	4		357	Outlet_Air_1_3	Type "K" TC
12	5		358	Outlet_Bottom_3	Type "K" TC
12	6		359	Outlet_Top_4	Type "K" TC
12	7		360	Outlet_Air_7_4	Type "K" TC
12	8		361	Outlet_Air_4_4	Type "K" TC
12	9		362	Outlet_Air_1_4	Type "K" TC
12	10		363	Outlet_Bottom_4	Type "K" TC
12	11		364	Rake_78.75_0%_20	Type "K" TC
12	12		365	Rake_78.75_.25"_20	Type "K" TC
12	13		366	Rake_78.75_5%_20	Type "K" TC
12	14		367	Rake_78.75_15%_20	Type "K" TC
12	15		368	Rake_78.75_50%_20	Type "K" TC
12	16		369	Rake_78.75_85%_20	Type "K" TC
12	17		370	Rake_78.75_95%_20	Type "K" TC
12	18		371	Rake_78.75_100%_20	Type "K" TC
12	19		372	Rake_168.75_0%_20	Type "K" TC
12	20		373	Rake_168.75_.25"_20	Type "K" TC
12	21		374	Rake_168.75_5%_20	Type "K" TC
12	22		375	Rake_168.75_15%_20	Type "K" TC
12	23		376	Rake_168.75_50%_20	Type "K" TC
12	24		377	Rake_168.75_85%_20	Type "K" TC
12	25		378	Rake_168.75_95%_20	Type "K" TC
12	26		379	Rake_168.75_100%_20	Type "K" TC
12	27		380	Rake_258.75_0%_20	Type "K" TC
12	28		381	Rake_258.75_.25"_20	Type "K" TC
12	29		382	Rake_258.75_5%_20	Type "K" TC
12	30		383	Rake_258.75_15%_20	Type "K" TC
12	31		384	Rake_258.75_50%_20	Type "K" TC

Slot	Channel		TC #	Instrument Nomenclature	Instrument Type
13	0		385	Rake_258.75_85%_20	Type "K" TC
13	1		386	Rake_25875_95%_20	Type "K" TC
13	2		387	Rake_258.75_100%_20	Type "K" TC
13	3		388	Rake_348.75_0%_20	Type "K" TC
13	4		389	Rake_348.75_.25"_20	Type "K" TC
13	5		390	Rake_348.75_5%_20	Type "K" TC
13	6		391	Rake_348.75_15%_20	Type "K" TC
13	7		392	Rake_348.75_50%_20	Type "K" TC
13	8		393	Rake_348.75_85%_20	Type "K" TC
13	9		394	Rake_348.75_95%_20	Type "K" TC
13	10		395	Rake_348.75_100%_20	Type "K" TC
13	11		396		
13	12		397		
13	13		398		
13	14		399		
13	15		400		
13	16		401		
13	17		402		
13	18		403		
13	19		404		
13	20		405		
13	21		406		
13	22		407		
13	23		408		
13	24		409		
13	25		410		
13	26		411		
13	27		412		
13	28		413		
13	29		414		
13	30		415		
13	31		416		

Slot	Channel		TC #	Instrument Nomenclature	Instrument Type
27	0			Vessel_Pressure_1	Pressure Transducer
27	1			Vessel_Pressure_2	Pressure Transducer
27	2			Atm_Pressure	Pressure Transducer
27	3			Current_Xducer_1	Current Transducer
27	4			Volt_Xducer_1	Volt Transducer
27	5			Power_Xducer_1	Power Transducer
27	6			Hot_Wire_South	Air Velocity Transducer
27	7			Hot_Wire_West	Air Velocity Transducer
27	8			Hot_Wire_North	Air Velocity Transducer
27	9			Hot_Wire_East	Air Velocity Transducer
27	10			Flow_1	Flow controller
27	11				
27	12				
27	13				
27	14				
27	15				
27	16				
27	17				
27	18				
27	19				
27	20				
27	21				
27	22				
27	23				
27	24				
27	25				
27	26				
27	27				
27	28				
27	29				
27	30				
27	31				